

INVESTIGATION OF STRUCTURAL CHANGES IN  
VANADIUM CONTAINING TRANSITION METAL OXIDES

by

MATTHEW AUSTIN DAVENPORT

JARED M. ALLRED, COMMITTEE CHAIR

GREGORY J. SZULCZEWSKI

ARUNAVA GUPTA

CLAUDIA MEWES

PAUL A. RUPAR

A DISSERTATION

Submitted in partial fulfillment of the requirements  
for the degree of Doctor of Philosophy in the  
Department of Chemistry and Biochemistry  
in the Graduate School of  
The University of Alabama

TUSCALOOSA, ALABAMA

2020

Copyright Matthew Austin Davenport 2020  
ALL RIGHTS RESERVED

## ABSTRACT

We have completed an experiment to obtain diffuse scattering data for use in a comprehensive study of the local-structure changes as a function of molybdenum composition and have made large strides in interpreting some of the major changes found in this study. For these experiments, single crystals of molybdenum substituted  $\text{VO}_2$  with the formula  $\text{V}_{1-x}\text{Mo}_x\text{O}_2$  were synthesized, with molybdenum compositions up to  $x = 0.60$ , using a novel, two-step chemical vapor transport synthesis. Using these large single crystals for total scattering experiments, we report the discovery of the sudden collapse of three-dimensional order in the low-temperature phase of  $\text{V}_{1-x}\text{Mo}_x\text{O}_2$  at  $x = 0.17$  and the emergence of a novel frustrated two-dimensional order at  $x = 0.19$ , with only a slight change in electronic properties. Single crystal diffuse x-ray scattering reveals that this transition from the 3D M1 phase to a 2D variant of the M2 phase results in long-range structural correlations along symmetry-equivalent (11L) planes of the tetragonal rutile structure, yet extremely short-range correlations transverse to these planes. Additionally, we report a combined study using single crystal X-ray diffraction, powder X-ray diffraction, and representational analysis to examine both the local and crystallographically averaged atomic structures simultaneously near  $x = 0.50$ . Between about  $x = 0.50$  and  $0.60$ , the average structure of  $\text{V}_{1-x}\text{Mo}_x\text{O}_2$  is the parent rutile phase, but the local symmetry is broken by atomic displacements that are best described by an orthorhombic cell in the spacegroup  $Fmmm$ . This model is locally identical to the two-dimensionally ordered 2D-M2 phase except the correlation length is much shorter in the 2D plane, and longer in the frustrated one, making it more isotropic.

## **DEDICATION**

To my parents, Tony and Melissa Davenport, as well as the rest of my family and friends for their love and support. Making it to this point would not have been possible without them.

## LIST OF ABBREVIATIONS AND SYMBOLS

2D	Two-dimensional
3D	Three-dimensional
ANL	Argonne National Laboratory
APS	Advanced Photon Source
C	Celsius
CCD	Charge Coupled Device
CCTW	Crystal coordinate transformation work-flow
CDW	Charge density wave
cm	Centimeter
CVT	Chemical vapor transport
CZ	Cold zone
d	Distance
DMFT	Dynamical Mean Field Theory
EDS	Energy dispersive X-ray Spectroscopy
FWHM	Full width at half maximum
g	Gram
ht	High temperature
HZ	Hot zone
ICP-OES	Inductively coupled plasma atomic emission spectroscopy
irrep	Irreducible representation

K	Kelvin
lt	Low temperature
M	Metal
M1	Monoclinic phase of VO <sub>2</sub> in <i>P2<sub>1</sub>/c</i> space group
M2	Monoclinic phase of VO <sub>2</sub> in <i>C2/m</i> space group
mg	Milligram
MIT	Metal-to-insulator transition
mm	Millimeter
nm	Nanometer
PDF	Pair distribution function
PXRD	Powder X-ray diffraction
R	Tetragonal phase of VO <sub>2</sub> in <i>P4<sub>2</sub>/mnm</i> space group
SEM	Scanning electron microscope
SPT	Structural phase transition
SXRD	Single crystal X-ray diffraction
T	Temperature
TEM	Transmission electron microscopy
TMO	Transition metal oxide
<i>x</i>	Composition
>	Greater than
<	Less than
≤	Less than or equal to
=	Equal to

°	Degrees
Å	Angstrom
$\lambda$	Lambda, wavelength
$\theta$	Theta, a rotation in X-ray scattering
$\xi$	Xi, correlation length

## ACKNOWLEDGEMENTS

I want to thank all of my friends, family, and mentors who have helped me and guided me through my time at The University of Alabama. I would like to give special thanks to my advisor Dr. Jared Allred for his encouragement and patience while working with me these past few years. For their help and support throughout my synthetic and experimental efforts, I would like to thank my group members David Matetich, Tyra Douglas, Logan Whitt, Avash Rawot, Chettri, Jacob Phillips, Eslam Elbakry, and all of our undergraduate students throughout the past few years. Our lab antics have filled the essential role of keeping each other sane during our studies.

A special thanks goes out to Dr. Raymond Osborn, Dr. Stephan Rosenkranz, and Dr. Matt Krogstad for all their help with diffuse scattering data collection and interpretation. We would have been lost during our scheduled beamtime without them. Thanks also goes to Dr. Douglas Robinson, the beamline scientist on 6-ID-D at Argonne National Laboratory, for his help with getting the beamline prepared and for his help and advice during our experiments, Matthew Confer and Dr. Sidhartha Bhattacharyya for their help with ICP-OES experiments, as well as Dr. Ni Ni and Chaowei Hu for their help with running resistivity measurements. I would also like to thank my committee members, Dr. Greg Szulczewski, Dr. Arunava Gupta, Dr. Paul Rugar, and Dr. Claudia Mewes for their support and guidance throughout my time as a graduate student. Their advice and guidance has been invaluable during my studies.

This work was primarily supported by the U.S. Department of Energy, Office of Science, Basic Energy Sciences, Materials Sciences and Engineering Division. The work at the University

of Alabama was supported under award DE-SC0018174. This research used resources of the Advanced Photon Source, a U.S. Department of Energy (DOE) Office of Science User Facility operated for the DOE Office of Science by Argonne National Laboratory under Contract No. DE-AC02-06CH11357. Work at UCLA done by Ni Ni and Chaowei Hu was supported by NSF DMREF program under the award NSF DMREF project DMREF-1629457. Thanks to NSF CHE MRI 1828078 and UA for the purchase of the single crystal X-Ray diffraction instrument used in this study. I also gratefully acknowledge the University of Alabama College of Engineering and College of Arts and Sciences shared analytical facility for providing use of the ICP-OES.

## CONTENTS

ABSTRACT.....	ii
DEDICATION.....	iii
LIST OF ABBREVIATIONS AND SYMBOLS .....	iv
ACKNOWLEDGEMENTS.....	vii
LIST OF TABLES.....	xii
LIST OF FIGURES .....	xiii
CHAPTER 1: INTRODUCTION.....	1
1.1 Transition Metal Oxides.....	1
1.2 VO <sub>2</sub> and the Metal-to-Insulator Transition.....	2
1.3 Chemical Substitution of VO <sub>2</sub> .....	5
1.4 X-Ray Diffraction and Diffuse Scattering .....	9
1.5 Chapter Outlines.....	12
References .....	15
CHAPTER 2: LARGE SINGLE CRYSTALS OF V <sub>1-x</sub> Mo <sub>x</sub> O <sub>2</sub> FROM A TWO-STEP CHEMICAL VAPOR TRANSPORT SYNTHESIS .....	20
2.1 Introduction.....	20
2.2 Experimental .....	21
2.2.1 Optimized Synthesis Method.....	21

2.2.2 Composition Determination .....	24
2.3 Results and Discussion.....	26
2.3.1 Optimization by Reagent Choice.....	26
2.3.2 Optimization by Transport Agent Choice .....	28
2.3.3 Final Optimization.....	29
2.4 Conclusion.....	30
Supporting Information.....	31
References .....	39
CHAPTER 3: FRAGILE 3D ORDER IN $V_{1-x}Mo_xO_2$ .....	41
3.1 Introduction.....	41
3.2 Experimental .....	43
3.3 Total Scattering Data.....	45
3.4 Interpretation and modelling of the 3D- $\Delta$ PDF.....	50
3.5 Discussion .....	54
3.6 Conclusions .....	55
References .....	56
CHAPTER 4: A CRYSTALLOGRAPHIC APPROACH TO THE SHORT-RANGE ORDERING PROBLEM IN $V_{1-x}Mo_xO_2$ ( $0.50 \leq x \leq 0.60$ ).....	59
4.1 Introduction.....	59
4.2 Experimental .....	60
4.3 Results and Discussion.....	61

4.3.1 Total Scattering Measurements .....	62
4.3.2 Structural Solutions .....	64
4.3.3 Powder Diffraction .....	71
4.4 Conclusions .....	74
References .....	75
CHAPTER 5: FURTHER WORK ON $V_{1-x}M_xO_2$ , $M = Mo, Cr, W$ AND $V_7Nb_6O_{29}$ .....	78
5.1 Introduction .....	78
5.2 Further work on $V_{1-x}Mo_xO_2$ .....	79
5.3 Synthesis and Total Scattering of Cr, W Substituted $VO_2$ .....	81
5.4 New Metal Site Ordering Phase, $V_7Nb_6O_{29}$ .....	82
5.5 Conclusions .....	86
References .....	87
CHAPTER 6: CONCLUSIONS .....	89

## LIST OF TABLES

<b>Table 1.1</b> Ionic Sizes for Relevant Transition Metals.....	13
<b>Table 2.1</b> Results of CVT synthesis using various starting materials and transport agents.....	23
<b>Table 2.2</b> $V_{1-x}Mo_xO_2$ , Determination of $x$ using three separate methods on the same batch. ....	24
<b>Table 4.1</b> Refinement results for the R phase and all nine possible subgroups.....	66
<b>Table 4.2</b> The difference between the long and short distances between the 4 metal atom sites as well as the angle of metal atom chains. ....	70
<b>Table 4.3</b> Values for the displacement modes for the P4, P1, C2, P3, C1, and 4D1 models. In the setting used here, B1u is the dimerizing metal displacement, B2u is the in-plane distortion coupled to the dimerization, and B3u is the in-plane distortion orthogonal to B2u. ....	71
<b>Table 4.4</b> Structural refinement parameters for the structural solution of $V_{0.45}Mo_{0.55}O_2$ in the space group <i>Fmmm</i> . ....	72
<b>Table 5.1</b> Structure solution data for $V_7Nb_6O_{29}$ .....	85

## LIST OF FIGURES

**Figure 1.1** Structure of VO<sub>2</sub> with only vanadium atoms shown. (a) The rutile c, b, and a axes, from left to right of the monoclinic, high temperature phase (M1). (b) The rutile c, b, and a axes, from left to right of the tetragonal, low temperature phase (R)..... 3

**Figure 1.2** (a) An exaggerated, one-dimensional example of the Peierls model indicating the formation of metal-cation dimers with alternating distances between the metal atoms. (b) Example of the band structure of a material with a Peierls transition both before and after the MIT with new bonding and antibonding orbitals creating the band gap. (c) Depiction of the Mott-Hubbard transition showing uncorrelated electrons of a paramagnetic material transitioning into a correlated antiferromagnetic structure. (d) Example of the band structure of a Mott-Hubbard insulator before and after the MIT with a band gap created by the electron correlations..... 4

**Figure 1.3** (a) The rutile c, b, and a axes, from left to right of the M1 monoclinic phase. (b) The rutile c, b, and a axes, from left to right of the M2 monoclinic phase. Atoms with dimerizing distortions are shown in blue, atoms with non-dimerizing distortions are shown in red, and atoms with both distortions are shown in purple. .... 7

**Figure 2.1** (a) The composition for the CVT growths were obtained by comparing known *a* lattice parameters to the *a* lattice parameters obtained by GSAS refinements. Once the composition was determined using the *a* lattice parameter, plots of the composition versus volume and (b) composition versus *c* lattice parameter were obtained in order to confirm that the obtained values matched well with the known trend. Error bars for both (a) and (b) are smaller than the points. (c) Plots for compositional range show how the diffraction peaks change as a function of composition..... 25

**Figure 2.2** SEM images of V<sub>1-x</sub>Mo<sub>x</sub>O<sub>2</sub> for *x* = (a) 0.10, (b) 0.33, and (c) 0.40. EDS maps for the incorporated elements are below the SEM images in panels (d), (e), and (f). In the EDS maps; vanadium is red, molybdenum is green, oxygen is yellow, tellurium is purple, chlorine is cyan, and carbon is blue. .... 26

**Figure 2.3** The oxygen content for V<sub>0.8</sub>Mo<sub>0.2</sub>O<sub>2</sub> was varied by changing the ratio of V<sup>3+</sup> to V<sup>4+</sup>. The most phase pure product was obtained for a 1:1 ratio indicating that the oxidation state of the metal needed to be balanced as an overall 4+ oxidation state. Byproducts for each

synthesis are labeled below the corresponding diffraction pattern with the diffraction peaks for that byproduct being denoted by an asterisk. .... 27

**Figure 2.4** Compositions were obtained by fitting the  $a$  lattice parameter of each sample to this linear fit of the  $a$  lattice parameters obtained by Holman et al.<sup>2</sup> ..... 31

**Figure 2.5** Product of CVT growth with VO<sub>2</sub>, V<sub>2</sub>O<sub>3</sub>, MoO<sub>3</sub>, and TeCl<sub>4</sub>. Byproducts pictured are V<sub>2</sub>O<sub>3</sub> and TeMo<sub>5</sub>O<sub>16</sub>. .... 32

**Figure 2.6** Product of CVT growth with VO<sub>2</sub>, V<sub>2</sub>O<sub>3</sub>, MoO<sub>3</sub>, and MoCl<sub>3</sub> ..... 32

**Figure 2.7** Product of CVT growth using V<sub>1-x</sub>Mo<sub>x</sub>O<sub>2</sub> and TeCl<sub>4</sub> ..... 33

**Figure 2.8** PXRD Pattern of V<sub>0.95</sub>Mo<sub>0.05</sub>O<sub>2</sub> ..... 34

**Figure 2.9** PXRD Pattern of V<sub>0.90</sub>Mo<sub>0.10</sub>O<sub>2</sub> ..... 34

**Figure 2.10** PXRD Pattern of V<sub>0.833</sub>Mo<sub>0.167</sub>O<sub>2</sub> ..... 35

**Figure 2.11** PXRD Pattern of V<sub>0.80</sub>Mo<sub>0.20</sub>O<sub>2</sub> ..... 35

**Figure 2.12** PXRD Pattern of V<sub>0.75</sub>Mo<sub>0.25</sub>O<sub>2</sub> ..... 36

**Figure 2.13** PXRD Pattern of V<sub>0.67</sub>Mo<sub>0.33</sub>O<sub>2</sub> ..... 36

**Figure 2.14** PXRD Pattern of V<sub>0.60</sub>Mo<sub>0.40</sub>O<sub>2</sub> ..... 37

**Figure 2.15** PXRD Pattern of V<sub>0.50</sub>Mo<sub>0.50</sub>O<sub>2</sub> ..... 37

**Figure 2.16** PXRD Pattern of V<sub>0.45</sub>Mo<sub>0.55</sub>O<sub>2</sub> ..... 38

**Figure 2.17** PXRD Pattern of V<sub>0.40</sub>Mo<sub>0.60</sub>O<sub>2</sub> ..... 38

**Figure 3.1** (a) The [010]<sub>R</sub> projection of the tetragonal rutile (R) phase, the low temperature monoclinic (M1) structure of VO<sub>2</sub>, and the monoclinic (M2) structure. The same three structures are shown in (b) from the [001]<sub>R</sub> projection. Boxes are drawn around {110}<sub>R</sub> distortion planes. Oxygen atoms are both omitted from (a) and (b) for clarity. (c) Stepwise schematic showing the conventional understanding of dimer formation driving the long-range distortion in two dimensions within {110}<sub>R</sub>. The arrows pointing from the far-right panel to

(b) are added to show how it projects onto the actual structures. M1 is a superposition of two orthogonal families of distortion planes. .... 42

**Figure 3.2** Reciprocal lattice slices from  $V_{1-x}Mo_xO_2$ . (a-e) Temperature dependence of the  $l = 0.5$  slices of  $x = 0.19$ , at  $T = 120, 140, 150, 160,$  and  $240$  K, respectively. (f)  $x = 0.17$  at  $200$  K, with same slice as above. (g-i) Composition dependence of the  $l = 1.5$  low temperature structures at  $x = 0.17, 0.19,$  and  $0.27$ . Coordinates are given in the reciprocal lattice vectors of the parent rutile unit cell..... 46

**Figure 3.3** (a) Temperature dependence of the correlation length,  $\xi$ , of 19% Mo as determined from fitting the peak width from the scattering data (circles) and from the 3D- $\Delta$ PDF (triangles). Red and blue symbols are for the  $[x,x,0]$  and  $[0,0,z]$  directions, respectively. (b) Resistivity,  $\rho$ , vs temperature of selected orientations of the 17% and 19% Mo crystals..... 48

**Figure 3.4** Symmetric log plots of the 3D- $\Delta$ PDF correlation maps from (a) 17% Mo and (b) 19% Mo at 115 and 120 K, respectively, parallel to the (001) plane at  $z = 0$ . (c) Section of the slice from the (110) plane. (d-e) Detailed views of the same slice with drawing showing the various types of lattice vectors that are observed. (d) Placement of the three types of interatomic vectors in the average rutile structure; large filled circles are on integer points and correspond to equivalent atom positions both M-M and O-O vectors. Large empty circles in black are at  $[u2,v2,w2]$  points, and only correspond to interchain M-M vectors. Small green circles correspond to both M-O and O-O vectors, which approximately overlap with each other near  $[0.35, 0.35, z]$  points. (e) and (f) use the same scheme, except the shapes are drawn over maxima in the 3D- $\Delta$ PDF correlation map. (e) shows how the interchain peaks are consistent with local dimer formation, and (f) shows a scheme consistent with the intrachain O atom displacements. The colormap inside the boxes in (e) is muted for clarity. The signal intensity is normalized to unity. .... 49

**Figure 3.5** The correlation between the real atom displacements and the 3D- $\Delta$ PDF map showing the probability of finding an atom. Increased positivity is in red and decreased probability is in blue. There are four possible deviations for each metal atom in the M2 phase, two possibilities for each chain of metal atoms. These are  $(x+\delta, y+\delta, z)$ ;  $(x-\delta, y-\delta, z)$ ;  $(x, y, z+\delta)$ ; and  $(x, y, z-\delta)$ . Atoms that are separated by the (1, 1, 1) lattice vector (A) are always displaced in the opposite direction giving a positive probability of finding the atom centered around the (1, 1, 1) point in panel D. Unlike the (1, 1, 1) lattice vector, atoms separated by the (2,2,1) lattice vector (B) have displacements in the same directions leading to four lobes of positive probability in panel D with the dimer formation leading to the positive probability at  $(2, 2, 1+2\delta)$  and  $(2, 2, 1-2\delta)$  and the non-dimerizing distortion leading to positive probability at  $(2+2\delta, 2+2\delta, 1)$  and  $(2-2\delta, 2-2\delta, 1)$ . Displacements in the xy direction and the z direction (C) are coupled in atoms separated by the (1.5, 1.5, 1.5) lattice vector with displacements resulting in the vector always being smaller in one direction

and larger in the other. These displacements are seen in the two-lobe positive probability in panel D at  $(1.5+\delta, 1.5+\delta, 1.5-\delta)$  and  $(1.5-\delta, 1.5-\delta, 1.5+\delta)$ . ..... 51

**Figure 3.6** (a) Comparison of observed diffuse scattering from various slices, on left, to the simulated scattering model, on right. (b) Comparison of observed 3D- $\Delta$ PDF, on left, to the calculated disorder model, on right. .... 53

**Figure 4.1** Cuts of the (a)  $hk\frac{1}{2}$  and the (b)  $hk1$  planes in  $V_{1-x}MoxO_2$  using the rutile lattice vectors. The presence of diffraction peaks in the (a)  $hk\frac{1}{2}$  plane should not exist without a break in the  $P4_2/mnm$  symmetry, but the peaks are considerably broader than usual Bragg peaks. (c-f) Total scattering data from beamline 6-ID-D at the APS. The scattering slices are all taken at  $L = 3/2$ . The 19% Mo data is shown to illustrate the 2D-M2 phase's scattering. All plots are in log scale. .... 64

**Figure 4.2** (a) Group-subgroup relations of selected models. (b-d) Schematics highlighting the results of the selected structure solutions. (b) P4 is the M1 phase, (c) P1, which is the M2 phase, and C2 have nearly identical models, suggesting M1 is incorrect. (d) P3 and C1 are nearly identical, and 4D1 agrees qualitatively with them as well. In 4D1, one of the “no distortion” sites has a small B2u distortion. .... 68

**Figure 4.3** PXRD data on  $V_{1-x}MoxO_2$  from 11-BM. (a) Comparison of peak shape between compositions. Peaks are both normalized and offset in  $2\theta$  for comparison. (b) Anisotropic peak broadening and strain analysis as a function of composition from Rietveld refinement using a rutile model (c) Comparison between expected supercell reflection  $(3/2\ 0\ 3/2)$  and observation in  $V_{0.44}Mo_{0.56}O_2$  for two different linewidths. The intensity is equivalent in both and is taken from the single crystal diffraction integrated intensities. The blue line has the same FWHM as the observed parent phase reflections in this composition (e.g. panel a). The orange line is uses the actual FWHM determined from total scattering (6-ID-D), shown in panel (d). .... 73

**Figure 5.1** The compositional dependence of the diffuse scattering features in  $V_{1-x}Mo_xO_2$ . .... 80

**Figure 5.2** Diffuse scattering feature similar to that caused by the 2D-M2 phase in  $V_{0.81}Mo_{0.19}O_2$ , found in  $V_{0.95}Cr_{0.05}O_2$ . .... 82

**Figure 5.3** Blue polyhedrons have vanadium at the center and the green polyhedrons have predominantly niobium at the center. A.) View down the c axis. B.) View down the a or b axis, this view shows the ferroelectric distortion in the center of the unit cell. C.) An extended view of the c axis view showing the connectivity between unit cells. The set of four atoms in the red box are isolated in panel D. Based on the partial occupancies of the four atoms forming this set, one will be a vanadium atom and three will be niobium atoms. .... 83

**Figure 5.4** Blue polyhedrons have vanadium at the center and the green polyhedrons have predominantly or entirely niobium at the center. A slice of the 1½1 plane for VNb<sub>9</sub>O<sub>25</sub> in panel A and V<sub>7</sub>Nb<sub>6</sub>O<sub>29</sub> in panel B. Due to the smaller overall oxidation state, the corner sharing interactions between the metal clusters, shown in the red boxes, is replaced with edge sharing interactions. .... 84

**Figure 6.1** Updated phase diagram including the newly characterized phase regions. The location and details about the phase boundary between the end of the *Fmmm* and the recurrence of the M1 phase at high molybdenum composition is still unknown. .... 90

## CHAPTER 1: INTRODUCTION

### 1.1 Transition Metal Oxides

Transition metal oxides (TMOs) are a class of materials with diverse electronic and magnetic properties.<sup>1</sup> The diversity of these properties is primarily due to the unique nature of their outer  $d$  electrons, which can exhibit both itinerant and localized electron properties.<sup>2</sup> This unusual behavior causes property predictions from elemental band theory to fail; however, some properties can be predicted based on structural factors such as the cation-cation separation and the cation-oxygen-cation overlap.<sup>3</sup> Because of their wide array of properties, TMOs have had a high volume of research interest with numerous uses in everyday objects and devices.<sup>1, 4</sup>

One topic of much importance is the role between physical structure and electronic structure as well as how structural phase transitions (SPTs) can contribute to electronic phase transitions. Both types of transitions occur in TMOs with varying levels of interplay between the two transitions. A SPT typically occurs in a material as a function of a change in temperature or pressure. Changes in bonding distances or angles in a metal-oxygen-metal chain can result in changes to the electronic band structure and electronic properties of the material.<sup>5</sup> In some cases, small changes in bonding distance or angle can have a large impact on the ability of a material to undergo an electronic phase transition for example, with most superconducting materials, any small change to the bonding can result in complete loss of superconductivity.<sup>6</sup> In other cases, periodic defects in materials can lead to phenomenon such as charge density waves (CDWs) in which electrons form a standing wave pattern and can collectively carry a charge.<sup>7</sup> Materials such as ferroelectrics rely on a SPT in order to have a physical change in their structure from a

non-polar to a polar phase allowing spontaneous electric polarization.<sup>8</sup> Gaining a better understanding of the role a material's structure plays in the emergence of that material's properties allows for tailoring of those properties for future technological applications.

The work presented in this dissertation explores the intricate interplay between the structure and properties of vanadium containing transition metal oxides with the majority of the work being done on changes in the phase transition in vanadium dioxide brought on by molybdenum substitution and solution of the difficult structural determinations of the resulting phases.

## **1.2 VO<sub>2</sub> and the Metal-to-Insulator Transition**

Vanadium dioxide is a material that can be either a metal or an insulator depending on external factors such as temperature through a type of electronic phase transition known as a metal-to-insulator transition (MIT).<sup>9</sup> This phenomenon was first discovered in magnetite in the 1940s and has since been observed in many different materials with the MIT in VO<sub>2</sub> being discovered by F.J. Morin in 1959.<sup>10</sup> This transition was evidenced by a change in resistance between 2 and 5 orders of magnitude depending on the quality of the crystalline sample.<sup>11</sup> In VO<sub>2</sub>, this change in resistivity is accompanied by a change in the physical structure of the material through the formation of canted V-V dimers.<sup>12</sup> This SPT leads to the lowering of symmetry from its tetragonal rutile phase (R) at high temperatures to its monoclinic (M1) phase at low temperatures, Figure 1.1. In bulk VO<sub>2</sub>, this transition takes place at 340K but, this transition temperature can be adjusted by making VO<sub>2</sub> thin films, nanoparticles, or through chemical substitution of another metal onto the vanadium atom site.<sup>13-18</sup> The mechanism behind the MIT in VO<sub>2</sub> has been primarily described by two potential models, with the degree of contribution each model has on the MIT continuing to be a point of debate amongst scientists in

the field even after six decades of research.<sup>15, 19-23</sup> These two models are the Peierls model in which is driven by electron-phonon correlations and the Mott-Hubbard model is driven by electron-electron correlations.<sup>24-26</sup> The Peierls model can be visualized in a one-dimensional system as a continuous chain of atoms that go from being equally spaced unpaired atoms to atoms pairs with alternating short and long distances, Figure 1.2. This change takes place because as the strength of the interaction between the phonon and the electrons increases, the vibrational frequency for the phonon mode decreases. Then, as the vibrational frequency decreases, neighboring atoms in this one-dimensional chain come into close proximity to each other for longer periods of time. This results in stronger interactions between atoms and even dimer formation once the atomic interactions become strong enough. In the case of a MIT driven

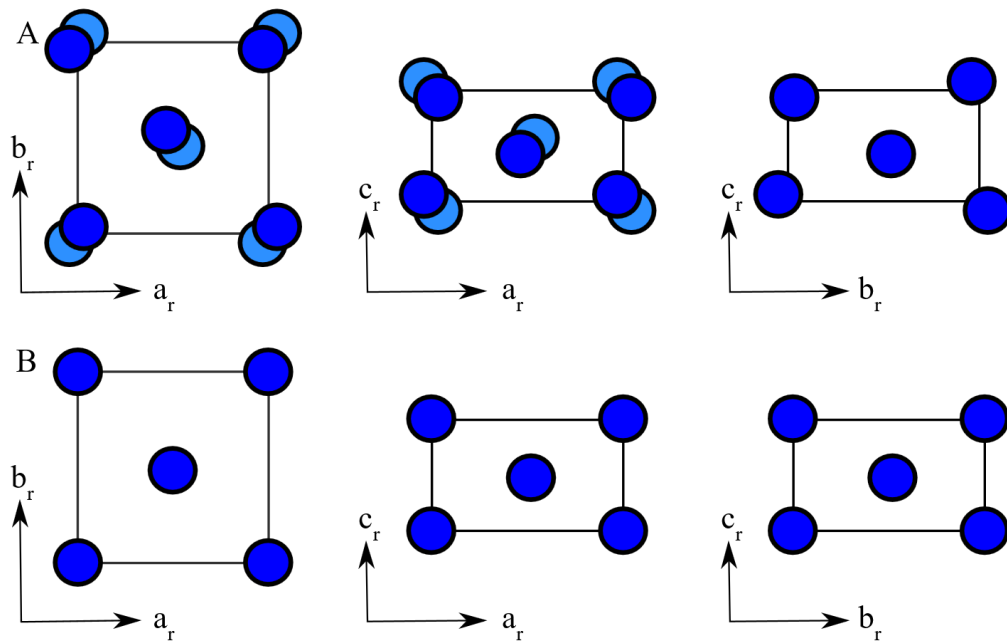


**Figure 1.1** Structure of VO<sub>2</sub> with only vanadium atoms shown. (a) The rutile c, b, and a axes, from left to right of the monoclinic, high temperature phase (M1). (b) The rutile c, b, and a axes, from left to right of the tetragonal, low temperature phase (R).

by this dimerization, new contributions to the band structure from these newly formed bonds leads to a split in the conducting band of electrons and a band gap at the fermi energy level.<sup>24</sup> Comparatively, the Mott-Hubbard model can be visualized as a paramagnetic material undergoing magnetic ordering and to become antiferromagnetic, Figure 1.2.<sup>26</sup> Because these correlations are so strong, the band structure contribution of these correlations, which had previously been inconsequential, becomes significant. This contribution can be realized in band structure calculations by the addition of a Hubbard term to the local-density approximation band-structure Hamiltonian.<sup>27</sup>

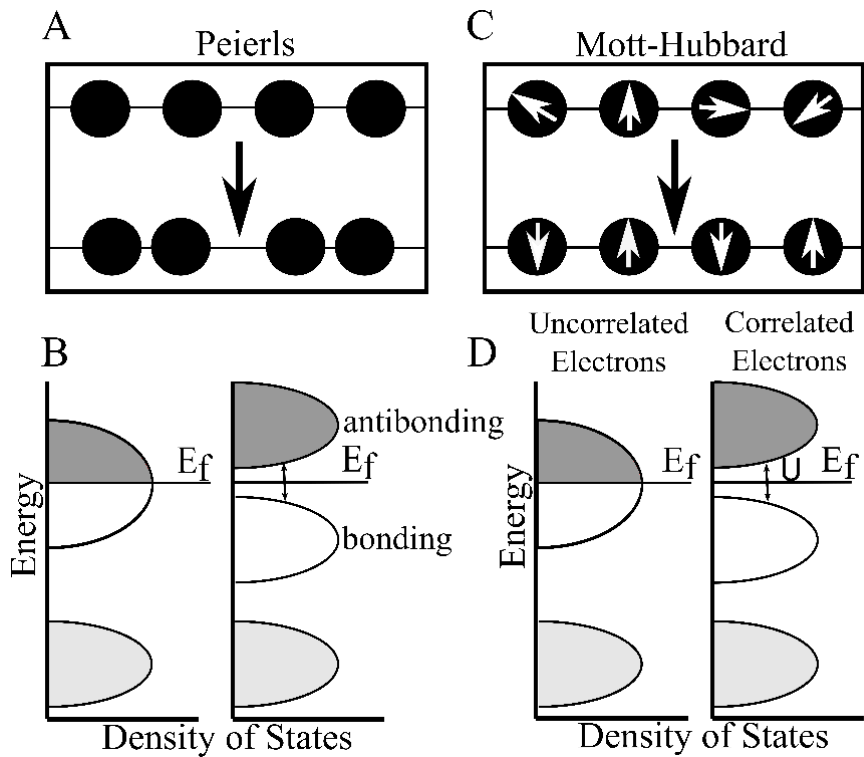


**Figure 1.2** (a) An exaggerated, one-dimensional example of the Peierls model indicating the formation of metal-cation dimers with alternating distances between the metal atoms. (b) Example of the band structure of a material with a Peierls transition both before and after the MIT with new bonding and antibonding orbitals creating the band gap. (c) Depiction of the Mott-Hubbard transition showing uncorrelated electrons of a paramagnetic material transitioning into a correlated antiferromagnetic structure. (d) Example of the band structure of a Mott-Hubbard insulator before and after the MIT with a band gap created by the electron correlations.

In VO<sub>2</sub>, the Peierls model is appealing because of the SPT which occurs simultaneously alongside the MIT. This is because dimer formation results in a lowering of symmetry from the conducting R phase to the insulating M1 phase with the addition of non-dimerizing distortions occurring in planes perpendicular to these bonding distortions.<sup>28-29</sup> Because of this structural change occurring alongside the MIT, some of the earliest work on VO<sub>2</sub> attributed the band gap to the Peierls mechanism.<sup>30-31</sup> When the one-dimensional Peierls model failed to account for the magnitude of the band gap, it became apparent that the model is too simplistic to adequately describe the three-dimensional structural transition that occurs in VO<sub>2</sub> as it only accounts for the dimer formation where VO<sub>2</sub> also sees in-plane, non-dimerizing distortions.<sup>19, 32-33</sup> However, purely structure based *ab initio* band structure calculations continue to fail to account for the magnitude of the band gap and have required the addition of a Hubbard term in order to effectively model the band gap.<sup>23</sup> Because of this, the general consensus on the mechanism behind the transition is some combination of the two mechanisms with other factors such as orbital overlap and spin-coupling also playing a role.<sup>34</sup>

While the structural change in VO<sub>2</sub> accompanied by the MIT has drawn much attention and controversy, studies on the structural instability behind the SPT have been less than abundant. Determining the role that structure plays on the MIT is important for further development of materials utilizing the MIT. However, we can only do so if the reason behind the structural phase transition itself is better understood.

### **1.3 Chemical Substitution of VO<sub>2</sub>**

Chemical substitution of different transition metals onto the vanadium atom site in VO<sub>2</sub> contributes to the material's structural instability and results in changes to the SPT or leads to the development of structural phases that are different, but related to the M1 and R structural

phases.<sup>17, 20-21, 35-36</sup> This makes the study of these structural changes in transition metal substituted VO<sub>2</sub> the ideal choice for furthering the study of the structural instability. Depending on the substituent being used, transition metal substitution can change the bonding orbitals, the number of valence electrons, or both at the same time. With the changes in the structural instability and the electronic structure, the addition of substituents also typically results in changes to the MIT such as an increase or decrease in the transition temperature or changes in the magnitude of the change in resistance during the transition. Studying these changes in the MIT brought on by substitution has proven useful in providing insight into the underlying mechanism of that transition and shows promise for learning more about the structural instability.<sup>15, 21</sup>

The results from chemical substitution onto the vanadium atom site in VO<sub>2</sub> largely contradict what would be expected from a Peierls model. Specifically, chromium substitution results in a change from the usual M1 monoclinic phase to a new semiconducting monoclinic phase M2 in which only half of the vanadium atoms form dimer pairs, with the other half undergoing in-plane, non-dimerizing distortions and no metal atoms undergoing both distortions as was the case with the M1 phase, Figure 1.3.<sup>15, 20, 37</sup> Because the band gap is largely insensitive to the structural differences between these two structures, as should be the case for a Peierls driven transition, many researchers prefer the Mott-Hubbard model as either a main contributor or, in some cases, as a sole contributor to the MIT.<sup>23, 38-39</sup> This M2 phase has also been observed in other substituents such as aluminum and titanium and has also been shown to exist in strained, unsubstituted VO<sub>2</sub> thin films and nanostructures providing further support for a Mott-Hubbard driven transition.<sup>18, 40-42</sup>

While the M2 phase has been heavily studied, there is still more left to understand about how the structural instability in VO<sub>2</sub> leads to its emergence.<sup>43-44</sup> The structural instability itself, while relevant to the MIT, is a separate avenue of investigation that has been overlooked as a result of the focus on the Mott Hubbard versus Peierls debate. Despite chromium being one of the most heavily studied substituent into the VO<sub>2</sub> structure, the phase diagram for the V<sub>1-x</sub>Cr<sub>x</sub>O<sub>2</sub> system is still not completely defined and has been drawn in many different ways occasionally with the inclusion of other monoclinic phases, orthorhombic phases, and triclinic phases.<sup>11, 15, 20, 37</sup> However, none of these additional phases are well defined with no clear consensus on what phases actually exist much less where their phase boundaries lie in the phase diagram. The questions about the structure of substituted VO<sub>2</sub> only grows as the structures of other substituents are considered with systems such as the (Ti,V)O<sub>2</sub> system only recently having been shown to undergo spinodal decomposition.<sup>45</sup>

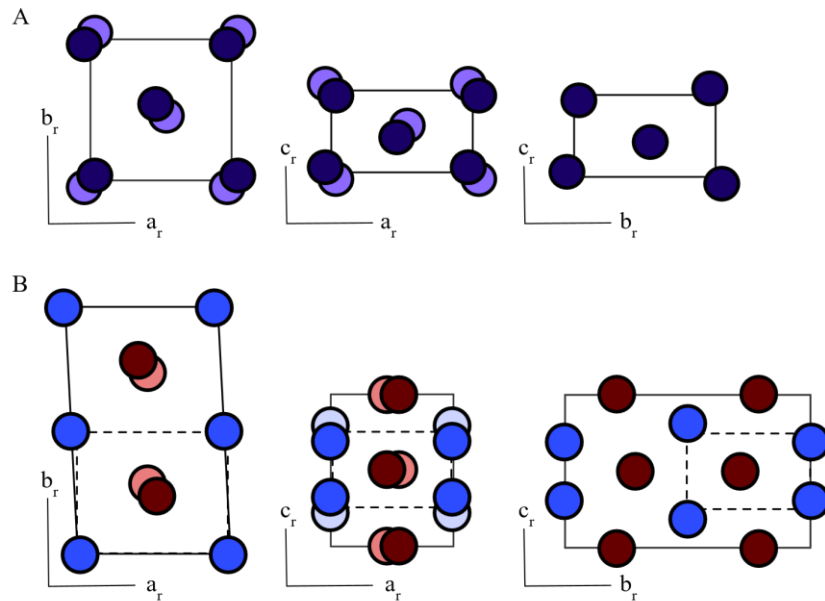


**Figure 1.3** (a) The rutile c, b, and a axes, from left to right of the M1 monoclinic phase. (b) The rutile c, b, and a axes, from left to right of the M2 monoclinic phase. Atoms with dimerizing distortions are shown in blue, atoms with non-dimerizing distortions are shown in red, and atoms with both distortions are shown in purple.

When considering substituents such as chromium and titanium, some of the difficulty in determining the structure could be, in part, due to the substituent being a  $3^+$  metal ion that then forces the normally  $4^+$  vanadium metal to compensate with a  $5^+$  charge. Yet, when considering substituents that go into the  $\text{VO}_2$  structure as  $4^+$  such as molybdenum, there is still evidence of structural anomalies. In work done by Marinder on heavily substituted  $\text{V}_{1-x}\text{Mo}_x\text{O}_2$  powders in 1975, the M2 phase was proposed to exist between  $0.50 \leq x \leq 0.70$  with the existence of two metastable versions of the M1 structure labeled M1' and M1'' between  $0.70 \leq x \leq 0.85$ ; however, the ordering in these phases was difficult to reproduce and required specific quenching steps to obtain.<sup>46</sup> Despite this early work on the structural studies of molybdenum substituted  $\text{VO}_2$ , more comprehensive work was not completed until 2009 when Holman et al performed a systematic study on the resistivity and magnetic susceptibility of  $\text{V}_{1-x}\text{Mo}_x\text{O}_2$  powders with  $0.05 \leq x \leq 0.50$ . In this work, the magnitude of the change in resistance was shown to decrease with increased molybdenum content until  $x = 0.20$  at which point both the MIT and the SPT disappeared. Additionally, transmission electron microscopy (TEM) measurements found evidence of supercell reflections in electron diffraction patterns around  $x = 0.50$ . These reflections are consistent with either the M1 or M2 superstructures, but they correspond to a short-range ordering with no evidence of long-range ordering peaks in synchrotron powder X-ray diffraction (PXRD) patterns. Molybdenum substituted  $\text{VO}_2$  is an ideal choice for furthering our understanding of the structural instability. This is because molybdenum goes into the structure with an oxidation state of  $4^+$ , and does not result in a change in the oxidation state of the vanadium atoms. A comprehensive study of single crystals of  $\text{V}_{1-x}\text{Mo}_x\text{O}_2$  will varying compositions and the mechanism by which the SPT is suppressed with increased composition should provide insight into this instability.

## 1.4 X-Ray Diffraction and Diffuse Scattering

X-ray diffraction is a necessary tool for the structural determination of highly ordered materials. The first known X-ray diffraction experiment was carried out by Max Von Laue in April of 1912, a discovery that led to the 1914 Nobel Prize in physics and an entirely new field of study.<sup>47</sup> X-rays diffract off the crystallographic lattice planes in the crystal structure when the Bragg condition,  $2d \sin \theta = n\lambda$ , is fulfilled. The intensities measured by the detector are known as Bragg reflections, named after William Bragg, and are based on the long-range ordering of the average crystal structure.<sup>48</sup> Measurement of these reflections provides information about the distance between lattice planes with the relative intensities of the reflections being dependent upon the symmetry of the crystal lattice as well as the atoms in the lattice planes that are diffracting the X-rays. In X-ray crystallography, the most structural information is obtained by using a single crystal sample in single crystal X-ray diffraction (SXRD) providing 3-dimensional information about the reciprocal lattice that can be used for structural determination. However, this experiment does not necessarily give full information about the products of a reaction and can be limited if single crystals are unobtainable. In these cases, PXRD can be used. PXRD uses a powder sample with lines of diffraction being measured rather than spherical peaks. PXRD benefits from having a larger sample size that can be used to better determine if multiple products were formed during synthesis as well as providing highly accurate lattice parameters; however, while high quality data can provide information about the position of atoms, a lot of the 3-dimensional data is lost in PXRD.

While these experiments are primarily used to determine the average crystal structure of materials, these materials can have many local defects that disrupt the average crystal structure and can also be measured by the detector in the area between Bragg reflections. These measured

intensities are called diffuse scattering or non-Bragg scattering since the cause of these reflections are short-range ordering, or local structure, of the crystal rather than the average crystal structure.<sup>49</sup> Because many properties in materials, such as resistance, are results of local structure changes rather than the average crystal structure, studying diffuse scattering can provide many insights into how the local structure changes facilitate the mechanisms behind the material's properties. The observation of diffuse features in the X-ray scattering were observed as early as in 1913.<sup>50</sup> Based on the idea of using these features to explain disorder, plenty of early work showed interest into the diffuse scattering effects of thermal motion and occupational disorder on the intensity of Bragg peaks as well as development of a theory of diffuse scattering that took into account longitudinal and transverse thermal vibrations.<sup>51-53</sup> With the utilization of monochromatic X-rays and better imaging, the observation of diffuse scattering as a result of imperfect lattices was a common occurrence leading to theoretical work on the diffraction of these imperfect lattices.<sup>49</sup> Despite much of this early work, the availability of high quality detectors and computational power has only become available recently with the use of area detectors able to obtain full three-dimensional data sets.<sup>49, 54</sup>

However, there are still many difficulties in the measurement and interpretation of diffuse scattering. Measuring diffuse scattering requires high intensity X-rays and expensive detectors with a high dynamic range in order to measure both the diffuse and Bragg scattering in the same frame because even the most intense diffuse scattering is still only a fraction of the intensity of the Bragg peaks.<sup>49</sup> In order to obtain this high-quality data, X-rays from a synchrotron source are ideal due to the increased intensity of the X-rays produced by sources as well as access to specialty detectors afforded at these facilities. Additionally, the ability to interpret even high-quality diffuse scattering data is still limited by the programs developed for that purpose.

Because the field of diffuse scattering is relatively young in its development compared to typical X-ray diffraction, the programs used to interpret the data are still in the process of evolving to become more usable and efficient. One tool developed for the analysis of the total diffuse scattering data is the pair distribution function (PDF) method. PDF is a method of analyzing diffuse scattering data from powder samples. This technique is a Fourier transform of the total X-ray powder diffraction pattern and provides the real interatomic distances in the studied material. However, because PDF is a one-dimensional technique, the information about the three-dimensional interatomic vectors is lost in this method. This means that interatomic vectors of similar length cannot be distinguished between even if the spatial orientation of the vectors are vastly different. This shortcoming was overcome by the development of the three-dimensional pair distribution function (3D-PDF). 3D-PDF is the Fourier transformation of the total scattering from a single crystal rather than a powder sample which allows for the interatomic vectors to be fully determined using high quality three-dimensional diffraction data. However, analysis of this data requires large amounts of computational power and time. To cut down on the taxing computational needs of 3D-PDF, the 3D- $\Delta$ PDF method was developed. 3D- $\Delta$ PDF uses a “punch and fill” method to remove the Bragg peaks so that it only focuses on the deviations of the local structure from the average structure rather than looking at the total scattering. This is beneficial because the average structure tends to be well documented prior to an investigation into the local structure of the material. Studying just the deviations in the local structure, cuts down on the amount of data needed for the computations which reduces the computational power and time required, making the data analysis more feasible.<sup>49</sup>

The first diffuse scattering work done on VO<sub>2</sub> was done in 1978 by Terauchi and Cohen. In this work, diffuse scattering was observed in the R-R direction, the direction between the (0.5,

0, 0.50) and the (0, 0.5, 0.5) R points, which indicated softening of a transverse phonon near the R point.<sup>44</sup> These results worked to confirm the lattice instability in pure VO<sub>2</sub>, however, the analysis was limited heavily by the instrumentation and software available at the time. Some of the most recent diffuse scattering work on VO<sub>2</sub> was done by Budai et al. in 2014. This work came in the form of thermal diffuse scattering experiments used to study excitations in the phonon modes during the phase transition and resulted in the observation of anisotropically anharmonic soft phonons, again near the R point in reciprocal space.<sup>55</sup> These diffuse scattering works have given some insight into the lattice instability and the mechanism behind the SPT in VO<sub>2</sub>; however, there is still little known about how chemical substitution affects this instability.

## 1.5 Chapter Outlines

The goal of the research presented in this dissertation is to explore the lattice instability in transition metal substituted VO<sub>2</sub>. The bulk of the work focuses around the V<sub>1-x</sub>Mo<sub>x</sub>O<sub>2</sub> family of compounds with additional work done using chromium, tungsten, and niobium in vanadium oxide systems Table 1.1 gives a list of relevant ion sizes for the six coordinate metal ions in the crystal lattice because, while not analyzed in this dissertation due to more interesting and unique diffuse scattering features, the size difference of the original metal and the substituent metal can cause diffuse scattering features called size effect scattering.<sup>49, 56</sup> The progress towards this goal will be laid out in the following chapters.

The second chapter of this dissertation explores the development and optimization process for the synthetic procedure of large, single crystals of V<sub>1-x</sub>Mo<sub>x</sub>O<sub>2</sub>, with reliable compositions between  $x = 0$  and  $x = 0.60$ . Previous synthetic methods for molybdenum substituted VO<sub>2</sub> resulted in either powder or polycrystalline products; however, to maintain information about the three-dimensional structural environment, large single crystals are

necessary. In this chapter, the optimization process for the synthetic method will be presented with the reliability of the resulting composition also being explored.

**Table 1.1** Ionic Sizes for Relevant Transition Metals

<b>Metal Ion</b>	<b>Crystal Radius (Å)</b>
V <sup>4+</sup>	0.72
Mo <sup>4+</sup>	0.79
Nb <sup>4+</sup>	0.82
W <sup>4+</sup>	0.80
V <sup>3+</sup>	0.78
W <sup>6+</sup>	0.74
V <sup>5+</sup>	0.68
Cr <sup>3+</sup>	0.755

In the  $V_{1-x}Mo_xO_2$  system, the MIT disappears around  $x = 0.20$ , with the SPT assumed to disappear as well. To determine what occurs at this composition, total scattering experiments for compositions below, at, and above  $x = 0.20$  are performed at various temperatures to determine how the local structure changes as a function of both substituent percentage and temperature. The third chapter will present the discovery of a new two-dimensional ordered phase which occurs due to a breakdown of the monoclinic ordering along the rutile c-axis. This new phase, brought on by geometric frustration, emphasizes the importance and complexity of the lattice instability.

Evidence of a superstructure in  $V_{0.50}Mo_{0.50}O_2$  was first observed by Holman et al. in 2009; however, due to the superlattice peaks only being visible in electron diffraction experiments and not in their PXRD experiments, the structure could not be determined. With single crystals of samples with compositions in this range, the determination of this

superstructure is possible and will be presented in chapter four. However, while the superlattice peaks are visible in SXRD, the peaks are broad due to a short correlation length. Because of this short correlation length, typical structure solution techniques would usually fail due to averaging of the short-range structure into a long-range structure solution. Despite this, by using an approach driven by group theory analysis to narrow down the possible structural solutions and then compare the magnitude of atomic displacements, determination of the appropriate structural solution was made possible. Further use of this structural determination for the solution of short to mid-range structural deviations should make difficult structural problems easier to manage, especially in the rutile system.

Using the same synthetic procedure from the molybdenum substitution experiments, the synthesis of chromium, tungsten, and niobium substituted vanadium oxides have also been explored. Chapter five presents preliminary results of diffuse scattering experiments for chromium substituted  $\text{VO}_2$  that have been completed with features similar to that in  $\text{V}_{0.81}\text{Mo}_{0.19}\text{O}_2$ ; however, with the long-range ordering maintaining a monoclinic symmetry. Samples of  $\text{V}_{1-x}\text{W}_x\text{O}_2$  have been synthesized with plans for diffuse scattering experiments to be carried out. Synthesis of single crystals of  $\text{V}_{1-x}\text{Nb}_x\text{O}_2$  does not seem to work using the same synthetic procedure; however, during attempts of this synthesis, a new metal site ordered compound was discovered,  $\text{V}_7\text{Nb}_6\text{O}_{29}$ , based on the structure solution, this material is a promising candidate as an antiferroelectric material.

## References

1. Rao, C. N. R., Transition Metal Oxides. *Annu. Rev. Phys. Chem.* **1989**, *40*, 291-326.
2. Localized and itinerant electrons in solids. In *Transition Metal Compounds*, Khomskii, D. I., Ed. Cambridge University Press: Cambridge, 2014; pp 1-24.
3. Goodenough, J. B., Metallic oxides. *Progr. Solid State Chem.* **1971**, *5*, 145-399.
4. *Transition Metal Compounds*. Cambridge University Press: Cambridge, 2014.
5. Steurer, W., Crystal Structures of the Elements. In *Encyclopedia of Materials: Science and Technology*, Buschow, H. H. J.; Cahn, R. W.; Flemings, M. C.; Ilschner, B.; Kramer, E. J.; Mahajan, S.; Vey, P., Eds. Elsevier: 2001; pp 1880-1897.
6. Wang, Z.; Yei, W.; Sidorov, V. A.; Bao, J.; Tang, Z.; Guo, J.; Zhou, Y.; Zhang, S.; Li, H.; Shi, Y., et al., Correlation between superconductivity and bond angle of CrAs chain in non-centrosymmetric compounds  $A_2Cr_3As_3$  ( $A = K, Rb$ ). *Scientific Reports* **2016**, *6*, 37878.
7. Gruner, G., The dynamics of charge-density waves. *Rev. Mod. Phys.* **1988**, *60* (4), 1129-1181.
8. Tagantsev, A. K., Size effects in Ferroelectric-Containing Structures. In *Encyclopedia of Materials: Science and Technology*, Buschow, K. H. J.; Cahn, R. W.; Flemings, M. C.; Ilschner, B.; Kramer, E. J.; Mahajan, S.; Vey, P., Eds. Elsevier: 2011; pp 1-6.
9. Imada, M.; Fujimori, A.; Tokyura, Y., Metal-insulator transitions. *Rev. Mod. Phys.* **1998**, *70* (4), 1039-1263.
10. Morin, F. J., Oxides Which Show a Metal-to-Insulator Transition at the Neel Temperature. *Phys. Rev. Lett.* **1959**, *3* (1), 34-36.
11. Ladd, L. A.; Paul, W., Optical and transport properties of high quality crystals of  $V_2O_4$  near the metallic transition temperature. *Solid State Commun.* **1969**, *7* (4), 425-428.

12. Anderson, G., Studies on Vanadium Oxides. *Acta. Chem. Scand.* **1956**, *10*, 623-628.
13. Zhu, M.; Qi, H.; Li, C.; Wang, B.; Wang, H.; Guan, T.; Zhang, D., VO<sub>2</sub> thin films with low phase transition temperature grown on ZnO/glass by applying substrate DC bias at low temperature of 250°C. *Appl. Surf. Sci.* **2018**, *453*, 23-30.
14. Chen, Z.; Gao, Y.; Kang, L.; Cao, C.; Chen, S.; Luo, H., Fine crystalline VO<sub>2</sub> nanoparticles: synthesis, abnormal phase transition temperatures and excellent optical properties of a derived VO<sub>2</sub> nanocomposite foil. *J. Mat. Chem. A* **2014**, *2* (8), 2718-2727.
15. Villeneuve, G.; Bordet, A.; Casalot, A.; Hagenmuller, P., Proprietes physiques et structurales de la phase Cr<sub>x</sub>V<sub>1-x</sub>O<sub>2</sub>. *Mat Res Bull* **1971**, *6* (2), 119-130.
16. Jin, P.; Tanemura, S., Relationship between Transition Temperature and x in V<sub>1-x</sub>W<sub>x</sub>O<sub>2</sub> Films Deposited by Dual-Target Magnetron Sputtering. *Jpn J Appl Phys* **1995**, *34*, 2459-2460.
17. Holman, K. L.; McQueen, T. M.; Williams, A. J.; Klimczuk, T.; Stephens, P. W.; Zandbergen, H. W.; Xu, Q.; Ronning, F.; Cava, R. J., Insulator to Correlated Metal Transition in V<sub>1-x</sub>Mo<sub>x</sub>O<sub>2</sub>. *Phys. Rev. B.* **2009**, *79*, 245114.
18. Kong, T.; Masters, M. W.; Bud'ko, S. L.; Canfield, P. C., Physical properties of V<sub>1-x</sub>Ti<sub>x</sub>O<sub>2</sub> (0 < x < 0.187) single crystals. *APL Mat.* **2015**, *3* (041502), 041502.
19. Goodenough, J. B., The Two Components of the Crystallographic Transition in VO<sub>2</sub>. *J. Solid State Chem.* **1971**, *3*, 490-500.
20. Marezio, M.; McWhan, B.; Remeika, J. P.; Dernier, P. D., Structural aspects of metal-insulator transitions in Cr-doped VO<sub>2</sub>. *Phys Rev B* **1972**, *5*, 2541-2551.
21. Villeneuve, G.; Bordet, A.; Casalot, A.; Pouget, J. P.; Launois, H.; Lederer, P., Contribution to the Study of the Metal-Insulator Transition in the V<sub>1-x</sub>Nb<sub>x</sub>O<sub>2</sub> System: I- Crystallographic and Transport Properties. *J. Phys. Chem. Solids* **1972**, *33*, 1953-1959.
22. Goodenough, J. B.; Hong, H. Y. P., Structures and a two-band model for the system V<sub>1-x</sub>Cr<sub>x</sub>O<sub>2</sub>. *Phys Rev B* **1973**, *8* (4), 1323-1331.
23. Wentzcovitch, R. M.; Schulz, W. W.; Allen, P. B., VO<sub>2</sub>: Peierls or Mott-Hubbard? A view from band theory. *Phys. Rev. Lett.* **1994**, *72* (21), 3389.

24. Peierls, R., *More Surprises in Theoretical Physics*. Princeton University Press: 1991.
25. Mott, N. F., The Basis of the Electron Theory of Metals, with Special Reference to the Transition Metals. *Proc. Phys. Soc. A*. **1949**, 62 (7), 416-422.
26. Mott, N. F., Metal-Insulator Transition. *Rev. Mod. Phys.* **1968**, 40 (4), 677-683.
27. Albers, R. C.; Christensen, N. E.; Svane, A., Hubbard-U Band-Structure Methods. *J. Phys.: Condens. Matter* **2009**, 21 (34), 343201.
28. Magneli, A.; Andersson, G., On the MoO<sub>2</sub> Structure Type. *Acta. Chem. Scand.* **1955**, 1955 (9), 1378-1381.
29. Heckingbottom, R.; Linnett, J. W., Structure of Vanadium Dioxide. *Nature* **1962**, 194, 678.
30. Goodenough, J. B., Narrow-band electrons in transition-metal oxides. *Czech. J. Phys. B* **1967**, 17, 304-336.
31. Adler, D.; Brooks, H., Theory of Semiconductor-To-Metal Transitions. *Phys. Rev.* **1967**, 155 (3), 826-840.
32. Verleur, H. W.; Jr., A. S. B.; Berglund, C. N., Optical Properties of VO<sub>2</sub> between 0.25 and 5 eV. *Phys. Rev.* **1968**, 172 (3), 788-798.
33. Berglund, C. N.; Jayaraman, A., Hydrostatic-Pressure Dependence of the Electronic Properties of VO<sub>2</sub> Near the Semiconductor-Metal Transition Temperature. *Phys. Rev.* **1969**, 185 (3), 1034-1039.
34. Tao, Z.; Han, T. T.; Mahanti, S. D.; Duxbury, P. M.; Yuan, F.; Ruan, C., Decoupling of Structural and Electronic Phase Transitions in VO<sub>2</sub>. *Phys Rev Lett* **2012**, 109, 166406.
35. Tan, X.; Yao, T.; Long, R.; Sun, Z.; Feng, Y.; Cheng, H.; Yuan, X.; Zhang, W.; Liu, Q.; Wu, C.; Xie, Y.; Wei, S., Unraveling Metal-insulator Transition Mechanism of VO<sub>2</sub> Triggered by Tungsten Doping. *Sci. Rep.* **2012**, 2 (466), 1-6.

36. Wu, Y.; Fan, L.; Chen, S.; Chen, S.; Chen, F.; Zou, C.; Wu, Z., A novel route to realize controllable phases in an aluminum ( $\text{Al}^{3+}$ )-doped  $\text{VO}_2$  system and the metal-insulator transition modulation. *Mater Lett* **2014**, *127*, 44-47.
37. Villeneuve, G.; Drillon, M.; Hagenmulier, P., Contribution a l'etude structurale des phases  $\text{V}_{1-x}\text{Cr}_x\text{O}_2$ . *Mat Res Bull* **1973**, *8*, 1111-1122.
38. Zylbersztejn, A.; Mott, N. F., Metal insulator transition in vanadium dioxide. *Phys. Rev. B* **1975**, *11* (11), 4383-4395.
39. Sakuma, R.; Miyake, T.; Aryasetiawn, F., Quasiparticle Band Structure of Vanadium Dioxide. *J. Phys.: Condens. Matter* **2009**, *21*, 6.
40. Ghedira, M.; Vincent, H.; Marezio, M.; Launay, J. C., Structural aspects of metal-insulator transitions in  $\text{V}_{0.985}\text{Al}_{0.015}\text{O}_2$ . *Solid State Chem* **1977**, *22*, 423-438.
41. Okimura, K.; Watanabe, T.; Sakai, J., Stress-induced  $\text{VO}_2$  films with M2 monoclinic phase stable at room temperature grown by inductively coupled plasma-assisted reactive sputtering. *J. Appl. Phys.* **2012**, *111*, 073514.
42. Jones, A. C.; Berweger, S.; Wei, J.; Cobden, D.; Raschke, M. B., Nano-optical Investigation of the Metal-Insulator Phase Behavior of Individual  $\text{VO}_2$  Microcrystals. *Nano Lett.* **2010**, *10*, 1574-1581.
43. Gupta, M.; Freeman, A. J.; Ellis, D. E., Electronic structure and lattice instability of metallic  $\text{VO}_2$ . *Phys Rev B* **1977**, *16* (8), 3338.
44. Terauchi, H.; Cohen, J. B., Diffuse x-ray scattering due to the lattice instability near the metal-semiconductor transition in  $\text{VO}_2$ . *Phys Rev B* **1978**, *17* (6), 2494-2496.
45. Hiroi, Z.; Hayamizu, H.; Yoshida, T.; Muraoka, Y.; Okamoto, Y.; Yamaura, J.; Ueda, Y., Spinodal Decomposition in the  $\text{TiO}_2$ - $\text{VO}_2$  System. *Chem. Mater.* **2013**, *25* (11), 2202-2210.
46. Marinder, B. O., On the Phase Relations in the  $\text{V}_x\text{Mo}_{1-x}\text{O}_2$  System ( $0 \leq x \leq 0.55$ ). *Mat. Res. Bull.* **1975**, *10*, 909-914.
47. *Early Days of X-Ray Crystallography*. Oxford University Press: Oxford, UK, 2013.

48. Bragg, W. L., The diffraction of Short Electromagnetic Waves by a Crystal. *Proc Camb Phil Soc* **1913**, *17*, 43-57.
49. Welberry, T. R.; Weber, T., One Hundred Years of Diffuse Scattering. *Crystallography Review* **2015**, *22* (1), 2-78.
50. Friedrich, W.; Knipping, P.; Laue, M., Interferenzerscheinungen bei Rontgenstrahlen. *Phys. Z.* **1913**, *14*, 1079-1087.
51. Debye, P. P., Interferenz von Rontgenstrahlen und Warmebewegung. *Ann. Phys. Lpz.* **1914**, *43*, 49-95.
52. Laue, M. v., Rontgenstrahlinterferenz und Mischkristalle. *Ann. Phys.* **1918**, *361* (15), 497-506.
53. Brillouin, L. N., Diffusion de la lumiere et des rayons X par un corps transparent homogene. *Ann. Phys. Paris* **1922**, *17*, 88-122.
54. Estermann, M. A.; Steurer, W., Diffuse Scattering data acquisition techniques. *Phase Transitions* **1998**, *67* (1), 165-195.
55. Budai, J. D.; Hong, J.; Manley, M. E.; Specht, E. D.; Li, C. W.; Tischler, J. Z.; Abernathy, D. L.; Said, A. H.; Leu, B. M.; Boatner, L. A.; McQueeney, R. J.; Delaire, O., Metallization of Vanadium Dioxide Driven by large Phonon Entropy. *Nature* **2014**, *515*, 535-539.
56. Pauling, L., *The Nature of The Chemical Bond*. Cornell University Press: Ithaca, NY, 1961.

## CHAPTER 2: LARGE SINGLE CRYSTALS OF $V_{1-x}Mo_xO_2$ FROM A TWO-STEP CHEMICAL VAPOR TRANSPORT SYNTHESIS

Chapter is adapted from previous publication.<sup>1</sup>

### 2.1 Introduction

The study of the local structure in  $V_{1-x}Mo_xO_2$  requires that large single crystals with reliable composition be synthesized. Previous work done using molybdenum substituted  $VO_2$  used powder or thin film synthetic methods.<sup>2-4</sup> However, previous research on various transition metal oxides, with vanadium oxides among them, have shown chemical vapor transport (CVT) synthesis capable of being used to obtain crystals of the desired size and chemical control.<sup>5-7</sup> CVT is a synthetic process where the starting materials and a volatile transport agent are placed into a sealed ampoule which is placed in a furnace. A temperature gradient is applied by heating opposite ends of the sealed ampoule to two different temperatures. The volatile transport agent reacts with the starting materials bringing them into the vapor phase. Convection from the temperature gradient then causes this gas phase product to travel to the opposite end of the sealed ampoule where the product of the transport synthesis is then deposited. This type of synthetic method was first discovered in nature from the transport of  $Fe_2O_3$  from volcanic gases and was first used in laboratory synthesis in 1925.<sup>8-9</sup> The most extensive work carried out on the CVT reaction was done in the 1950s and 1960s with the discovery of many new transport agents and the understanding of the thermodynamics of the CVT reaction.<sup>7, 10-11</sup> The CVT synthesis is a promising method for obtaining single crystals of  $V_{1-x}Mo_xO_2$ ; however, due to potential reactivity with the transport agent the synthesis requires optimization.

## 2.2 Experimental

Synthesis of  $V_{1-x}Mo_xO_2$  was achieved using a CVT method. The varied parameters for the optimization of this synthesis were primarily: reagent choice, input stoichiometry, and transport agent; though a few temperature gradient variations are also reported below. Unless stated otherwise, the dwell time was 6 days, the hot zone was 950 °C (9 hour ramp on heating, 8 hour ramp on cooling), and the cold zone was 850 °C (10 hour ramp on heating, 9 hour ramp on cooling).

The following reagents were used:  $VO_2$  (Materion, 99.5%),  $V_2O_3$  (Alfa Aesar, 99.7%),  $MoO_3$  (Alfa Aesar, 99.95%), and  $MoO_2$ .  $MoO_2$  was obtained through the reduction of  $MoO_3$  by passing 5%  $H_2$  gas in Ar over the  $MoO_3$  for 24 hours at 565 °C, and verified using PXRD. A total of 0.3 to 0.6 g of reagents were used. Transport agents used were  $VCl_3$  (Alfa Aesar, 99%),  $MoCl_3$  (Alfa Aesar, 99.5%), and  $TeCl_4$  (Alfa Aesar, 99.9%). For each reaction, samples were sealed in evacuated fused quartz ampoules, with a 1 cm diameter, ~23 cm length and an equivalent mass of transport agent (0.15 mg) was used. All experiments were performed in the same furnace (Lindberg Blue Three Zone furnace).

### 2.2.1 Optimized Synthesis Method

The various growth methods attempted are reported in the Results section below and tabulated in Table 2.1. Based on the results reported below, the optimized synthesis of large single crystal samples of  $V_{1-x}Mo_xO_2$  for  $0 \leq x \leq 0.60$  requires a two-part CVT synthesis with the first step used to synthesize phase-pure  $V_{1-x}Mo_xO_2$  and the second step used for crystal growth. For the first step, the CVT-style setup was the only way found to prevent the formation of higher Mo- containing oxides in this step. The second step requires phase-pure  $V_{1-x}Mo_xO_2$  as a precursor, otherwise molybdenum tellurate phases poison the reaction.

The first step uses  $\text{MoCl}_3$  as a transport agent and starting materials chosen from  $\text{VO}_2$ ,  $\text{V}_2\text{O}_3$ ,  $\text{MoO}_3$ , and  $\text{MoO}_2$  in order to give a V:Mo:O ratio to match the target composition. Given the oxidation state range available, multiple starting material compositions could be used (e.g. either 3:1  $\text{VO}_2$ : $\text{MO}_2$  or 1:1:1  $\text{V}_2\text{O}_3$ : $\text{VO}_2$ : $\text{MoO}_3$  for  $x = 0.25$ ), but the final composition of the main product was insensitive to this choice for this step.

The resulting products are a few, small single crystals of  $\text{V}_{1-x}\text{Mo}_x\text{O}_2$  in the cold zone of the tube and a large amount of a black polycrystalline powder of phase-pure  $\text{V}_{1-x}\text{Mo}_x\text{O}_2$  in the hot zone of the tube. Both the resulting single crystal and polycrystalline products have molybdenum compositions in close agreement to the initial input value.

In order to obtain larger single crystals, the phase pure polycrystalline samples from the hot zone were ground into a fine powder and placed into new evacuated ampoules, this time using  $\text{TeCl}_4$  as the transport agent, and heated using the same standardized heating schedule reported above. This second CVT synthesis resulted in the formation of single crystals of  $\text{V}_{1-x}\text{Mo}_x\text{O}_2$ , with  $x$  near that of the input value, in the cold zone. These crystals were large (5mm x 0.5mm x 0.5mm), rod-shaped single crystals that, like the polycrystalline samples, were black in color with a slight bluish or purplish metallic cast.

**Table 2.1** Results of CVT synthesis using various starting materials and transport agents.

Starting Materials	Ratio V : Mo : O	Transport Agent	$V_{1-x}Mo_xO_2$ $x =$	Byproducts
VO <sub>2</sub> , V <sub>2</sub> O <sub>3</sub> , MoO <sub>3</sub>	0.80 : 0.20 : 1.8	TeCl <sub>4</sub>	0.418(11) <sup>HZ</sup>	Mo <sub>4</sub> V <sub>9</sub> O <sub>25</sub> <sup>HZ</sup>
VO <sub>2</sub> , V <sub>2</sub> O <sub>3</sub> , MoO <sub>3</sub>	0.80 : 0.20 : 1.9	TeCl <sub>4</sub>	0.159(7) <sup>HZ</sup>	Mo <sub>0.9</sub> V <sub>1.1</sub> O <sub>5</sub> <sup>HZ</sup>
VO <sub>2</sub> , V <sub>2</sub> O <sub>3</sub> , MoO <sub>3</sub>	0.80 : 0.20 : 2.0	TeCl <sub>4</sub>	0.163(7) <sup>HZ</sup>	TeMo <sub>5</sub> O <sub>16</sub> <sup>HZ+CZ</sup>
VO <sub>2</sub> , V <sub>2</sub> O <sub>3</sub> , MoO <sub>3</sub>	0.80 : 0.20 : 2.1	TeCl <sub>4</sub>	0.157(7) <sup>HZ</sup>	V <sub>4</sub> O <sub>7</sub> <sup>HZ</sup>
VO <sub>2</sub> , V <sub>2</sub> O <sub>3</sub> , MoO <sub>3</sub>	0.80 : 0.20 : 2.2	TeCl <sub>4</sub>	0.045(6) <sup>HZ</sup>	V <sub>3</sub> O <sub>5</sub> <sup>HZ</sup>
VO <sub>2</sub> , V <sub>2</sub> O <sub>3</sub> , MoO <sub>3</sub>	0.67 : 0.33 : 2	TeCl <sub>4</sub>	0.294(9) <sup>HZ</sup>	TeMo <sub>5</sub> O <sub>16</sub> <sup>HZ+CZ</sup> , TeMo <sub>4</sub> O <sub>13</sub> <sup>HZ</sup>
V <sub>2</sub> O <sub>3</sub> , MoO <sub>3</sub> , MoO <sub>2</sub>	0.60 : 0.40 : 2	TeCl <sub>4</sub>	0.187(7) <sup>CZ</sup>	MoO <sub>2</sub> <sup>HZ</sup>
V <sub>2</sub> O <sub>3</sub> , MoO <sub>3</sub> , MoO <sub>2</sub>	0.50 : 0.50 : 2	TeCl <sub>4</sub>	0.242(8) <sup>CZ</sup>	TeMo <sub>5</sub> O <sub>16</sub> <sup>HZ+CZ</sup> ,
VO <sub>2</sub> , V <sub>2</sub> O <sub>3</sub> , MoO <sub>3</sub>	0.90 : 0.10 : 2	VCl <sub>3</sub>	N/A	V <sub>3</sub> O <sub>5</sub> <sup>HZ</sup> , V <sub>2</sub> O <sub>3</sub> <sup>HZ</sup>
VO <sub>2</sub> , V <sub>2</sub> O <sub>3</sub> , MoO <sub>3</sub>	0.80 : 0.20 : 2	VCl <sub>3</sub>	N/A	MoO <sub>2</sub> <sup>HZ</sup>
VO <sub>2</sub> , V <sub>2</sub> O <sub>3</sub> , MoO <sub>3</sub>	0.70 : 0.30 : 2	VCl <sub>3</sub>	0.361(9)	N/A
VO <sub>2</sub> , V <sub>2</sub> O <sub>3</sub> , MoO <sub>3</sub>	0.95 : 0.05 : 2	MoCl <sub>3</sub>	0.051(6) <sup>HZ</sup>	N/A
VO <sub>2</sub> , V <sub>2</sub> O <sub>3</sub> , MoO <sub>3</sub>	0.90 : 0.10 : 2	MoCl <sub>3</sub>	0.103(6) <sup>HZ</sup>	N/A
VO <sub>2</sub> , V <sub>2</sub> O <sub>3</sub> , MoO <sub>3</sub>	0.80 : 0.20 : 2	MoCl <sub>3</sub>	0.209(7) <sup>HZ</sup>	V <sub>4</sub> O <sub>7</sub> <sup>HZ</sup>
VO <sub>2</sub> , V <sub>2</sub> O <sub>3</sub> , MoO <sub>3</sub>	0.70 : 0.30 : 2	MoCl <sub>3</sub>	0.319(9) <sup>HZ</sup>	N/A
V <sub>2</sub> O <sub>3</sub> , MoO <sub>3</sub> , MoO <sub>2</sub>	0.60 : 0.40 : 2	MoCl <sub>3</sub>	0.438(11) <sup>HZ</sup>	VOCl <sup>HZ</sup> , V <sub>2</sub> O <sub>3</sub> <sup>HZ</sup>
V <sub>2</sub> O <sub>3</sub> , MoO <sub>3</sub> , MoO <sub>2</sub>	0.45 : 0.55 : 2	MoCl <sub>3</sub>	0.545(13) <sup>HZ</sup>	V <sub>2</sub> O <sub>3</sub> <sup>HZ</sup>
V <sub>2</sub> O <sub>3</sub> , MoO <sub>3</sub> , MoO <sub>2</sub>	0.40 : 0.60 : 2	MoCl <sub>3</sub>	0.598(14) <sup>HZ</sup>	Mo <sub>4</sub> O <sub>11</sub> <sup>HZ+CZ</sup>
V <sub>0.95</sub> Mo <sub>0.05</sub> O <sub>2</sub>	0.95 : 0.05 : 2	TeCl <sub>4</sub>	0.052(6) <sup>CZ</sup>	N/A
V <sub>0.90</sub> Mo <sub>0.10</sub> O <sub>2</sub>	0.90 : 0.10 : 2	TeCl <sub>4</sub>	0.102(6) <sup>CZ</sup>	N/A
V <sub>0.80</sub> Mo <sub>0.20</sub> O <sub>2</sub>	0.80 : 0.20 : 2	TeCl <sub>4</sub>	0.218(8) <sup>CZ</sup>	N/A
V <sub>0.70</sub> Mo <sub>0.30</sub> O <sub>2</sub>	0.70 : 0.30 : 2	TeCl <sub>4</sub>	0.297(9) <sup>CZ</sup>	N/A
V <sub>0.60</sub> Mo <sub>0.40</sub> O <sub>2</sub>	0.60 : 0.40 : 2	TeCl <sub>4</sub>	0.394(10) <sup>CZ</sup>	N/A
V <sub>0.45</sub> Mo <sub>0.55</sub> O <sub>2</sub>	0.45 : 0.55 : 2	TeCl <sub>4</sub>	0.55(1) <sup>CZ</sup>	N/A
V <sub>0.40</sub> Mo <sub>0.60</sub> O <sub>2</sub>	0.40 : 0.60 : 2	TeCl <sub>4</sub>	0.60(1) <sup>CZ</sup>	Mo <sub>4</sub> O <sub>11</sub> <sup>CZ</sup>

Superscripts denote the end of the tube in which the product formed: HZ=Hot Zone, CZ=Cold Zone.

## 2.2.2 Composition Determination

The concentration of molybdenum in the resulting  $V_{1-x}Mo_xO_2$  samples was determined using PXRD with data from Holman et al. as a reference, as the  $a$  lattice parameter was shown to increase linearly with molybdenum composition.<sup>2</sup> Using this linear trend and lattice parameters obtained from PXRD refinements, the compositions of these  $V_{1-x}Mo_xO_2$  samples were calculated and plotted in Figure 2.1 which shows the close agreement with the previous data. The compositions of these samples were further verified by 1) refining the V:Mo occupancy ratio through single crystal structural refinements and 2) through inductively coupled plasma atomic emission spectroscopy (ICP-OES) experiments (Table 2.2). Additionally, sample homogeneity was confirmed using scanning electron microscopy (SEM) energy dispersive X-ray spectroscopy (EDS) analysis, shown in Figure 2.2, to obtain maps of the surface of several single crystals in the composition range.

**Table 2.2**  $V_{1-x}Mo_xO_2$ , Determination of  $x$  using three separate methods on the same batch.

Input	SXRD	PXRD	ICP-OES
0.05	0.076(15)	0.074(6)	0.078(3)
0.10	0.082(8)	0.095(6)	0.1062(12)
0.40	0.20(2)	0.187(7)	0.1881(17)
0.30	n/a	0.319(9)	0.333(2)
0.40	0.412(12)	0.438(11)	0.4526(1)
0.55	0.52(3)	0.55(1)	0.53608(3)

Note that similar input composition can lead to different final compositions depending on the reaction conditions (Table 2.1).

The room temperature crystallographic unit-cell parameters were obtained using a Bruker D2 Phaser, Cu-K $\alpha$  radiation with structural models from GSAS and EXPGUI being used to fit the data.<sup>12-13</sup> Single crystal diffraction data was collected using a Siemens diffractometer

equipped with a Bruker APEX-II CCD and a monochromated Mo-K $\alpha$  producing sealed source. Structural models of the single crystal diffraction data were created and refined using SHELX and WINGX.<sup>14-15</sup> SEM-EDS data was collected using a Jeol 7000 FE SEM at an energy of 20.0 kV.

A PerkinElmer Optima 8300 ICP-OES with axial viewing was used for composition analysis. A calibration curve was developed using a multielement standard (Quality Control Standard 19, VWR, Lot# P2-MEB677343), the wavelengths used were Mo(II) 202.031 and V(II) 290.880 nm. No emission from other elements in the multielement standard overlap with the analyte peaks was observed. All samples were delivered at 1.5 mL min<sup>-1</sup> with a plasma flow of 15 L min<sup>-1</sup>, auxiliary flow of 0.5 L min<sup>-1</sup>, nebulizer flow of 0.8 L min<sup>-1</sup>, and power of 1300 W.

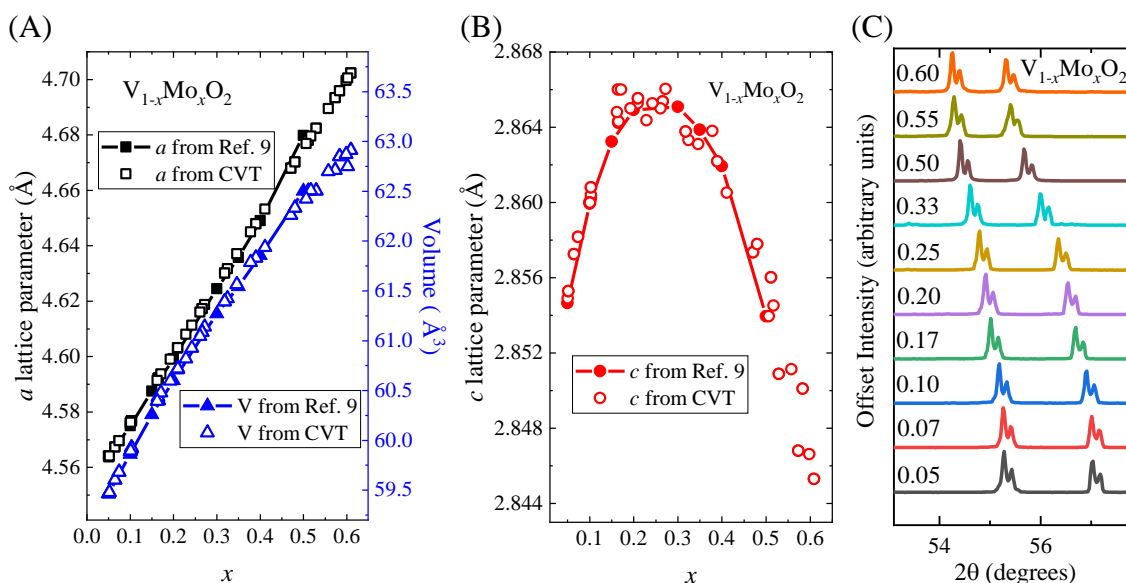


**Figure 2.1** (a) The composition for the CVT growths were obtained by comparing known *a* lattice parameters to the *a* lattice parameters obtained by GSAS refinements. Once the composition was determined using the *a* lattice parameter, plots of the composition versus volume and (b) composition versus *c* lattice parameter were obtained in order to confirm that the obtained values matched well with the known trend. Error bars for both (a) and (b) are smaller than the points. (c) Plots for compositional range show how the diffraction peaks change as a function of composition.

## 2.3 Results and Discussion

The first step to obtaining an optimized synthesis of  $V_{1-x}Mo_xO_2$  single crystals was to determine an appropriate transport agent and temperature gradient for CVT. Because various vanadium oxides have previously been grown using a CVT synthesis with  $TeCl_4$  as a transport agent and with a temperature gradient between 850 °C and 950 °C, this was chosen as the starting point for the synthesis.<sup>6</sup> Before proceeding with cation substitution experiments, large (7mm x 0.8 mm x 0.8mm) single crystals of unsubstituted  $VO_2$ , grey with a metallic sheen, were grown confirming this temperature schedule as a valid starting point for the synthesis.

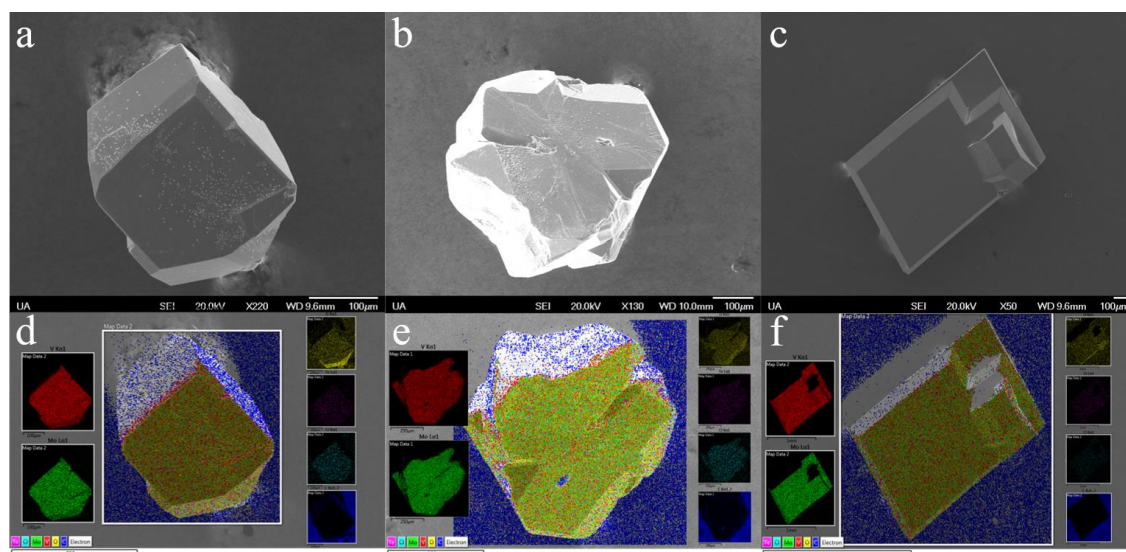


**Figure 2.2** SEM images of  $V_{1-x}Mo_xO_2$  for  $x =$  (a) 0.10, (b) 0.33, and (c) 0.40. EDS maps for the incorporated elements are below the SEM images in panels (d), (e), and (f). In the EDS maps; vanadium is red, molybdenum is green, oxygen is yellow, tellurium is purple, chlorine is cyan, and carbon is blue.

### 2.3.1 Optimization by Reagent Choice

To obtain single crystals of molybdenum substituted  $VO_2$ , it is necessary to determine an appropriate V:Mo:O ratio, as disproportionation may occur. This was done by selecting the molybdenum composition at which a 1:1 ratio of  $V^{3+}$  to  $V^{4+}$ , would balance with the 6+ oxidation state of the molybdenum in  $MoO_3$  to give an overall 4+ oxidation state on the metal

atom. This composition,  $V_{0.8}Mo_{0.2}O_2$ , was then synthesized using  $MoO_3$  as the molybdenum source and then varying the amount of the  $V_2O_3$  and  $VO_2$  starting materials to obtain  $V^{3+}:V^{4+}$  ratios between 1:0 and 0:1, PXRD of the resulting phases are shown in Figure 2.3. Of these reactions, the fewest extraneous phases were found in the 1:1,  $V^{3+}:V^{4+}$ , sample. Therefore, a 1:1 ratio of  $V_2O_3:MoO_3$  (*i.e.*, 2:1  $V^{3+}:Mo^{6+}$ ) was used to maintain an overall 4+ oxidation state for the synthesis of  $V_{1-x}Mo_xO_2$  with  $0.05 \leq x \leq 0.33$ .

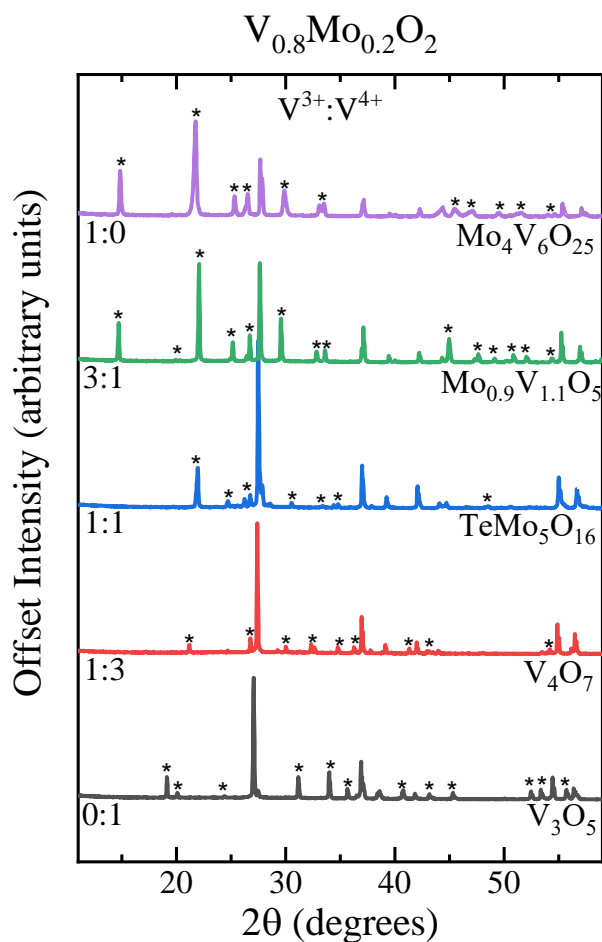


**Figure 2.3** The oxygen content for  $V_{0.8}Mo_{0.2}O_2$  was varied by changing the ratio of  $V^{3+}$  to  $V^{4+}$ . The most phase pure product was obtained for a 1:1 ratio indicating that the oxidation state of the metal needed to be balanced as an overall 4+ oxidation state. Byproducts for each synthesis are labeled below the corresponding diffraction pattern with the diffraction peaks for that byproduct being denoted by an asterisk.

For the above reactions, the hot zone of the tube contained nearly phase pure polycrystalline  $V_{1-x}Mo_xO_2$ , but there were very few single crystals obtained in the cold zone. Analysis of these crystals by SXRD determined them to be  $TeMo_5O_{16}$ . Since tellurium from the transport agent was removed from the gas phase to form this side product, the reaction resulted in no transport of  $VO_2$ , leaving polycrystalline  $V_{1-x}Mo_xO_2$ , with an irreproducible molybdenum content remaining in the hot zone. This lack of transport also indicates that this unwanted reaction likely took place between the  $TeCl_4$  transport agent and the  $MoO_3$  starting material early in the reaction, possibly even before the furnace reached full temperature due to the high vapor pressure of  $MoO_3$ .

With the high vapor pressure of  $MoO_3$  appearing to cause a reaction with the  $TeCl_4$  transport agent,  $MoO_2$  was chosen as an alternate molybdenum source to bypass the molybdenum tellurate byproduct. This CVT synthesis with only  $VO_2$  and  $MoO_2$  starting materials was successful in avoiding the molybdenum tellurate side product and lead to large single crystals of  $V_{1-x}Mo_xO_2$ . However, the output molybdenum composition was roughly half that of the input composition for all samples with excess  $MoO_2$  crystals in the hot zone of the tube (Table 2.1).

### **2.3.2 Optimization by Transport Agent Choice**

When using  $TeCl_4$  as the transport, the use of both  $MoO_3$  and  $MoO_2$  as Mo sources had drawbacks that precluded the formation of large crystals with the desired molybdenum content. In order to avoid the formation of  $TeMo_5O_{16}$  while maintaining control over the molybdenum content, two alternative transport agents,  $VCl_3$  and  $MoCl_3$ , were tested using  $MoO_3$  as the molybdenum source. These transport agents were selected as candidates because they each decompose into one or more gaseous product upon heating and only introduce chlorine as an

additional element to the synthesis. Transport using  $\text{VCl}_3$  failed to produce phase pure products; however, transport using  $\text{MoCl}_3$  resulted in phase pure black phase-pure polycrystalline  $\text{V}_{1-x}\text{Mo}_x\text{O}_2$  in the hot zone and very few, small (0.10mm x 0.04mm x 0.04mm) single crystals of  $\text{V}_{1-x}\text{Mo}_x\text{O}_2$  with  $0 \leq x \leq 0.33$  obtained in the cold zone. These products were characterized using PXRD and SXRD (Table 2.1). When attempting to obtain compositions of  $\text{V}_{1-x}\text{Mo}_x\text{O}_2$  where  $x > 0.33$  using only  $\text{MoO}_3$  as the molybdenum source, the synthesis resulted in impure samples of lower compositions of  $\text{V}_{1-x}\text{Mo}_x\text{O}_2$  with lower molybdenum concentration than the input composition as well as various vanadium and molybdenum Magnéli phases, phases with the formula  $\text{V}_n\text{O}_{2n-1}$  and  $\text{Mo}_n\text{O}_{3n-1}$ , due to the oxygen content no longer being balanced to provide a 1:2 metal:oxygen ratio. Therefore, in order to exceed the  $x = 0.33$  threshold,  $\text{MoO}_2$  must be used to balance the oxygen content. By introducing  $\text{MoO}_2$  as an additional reactant, polycrystalline samples of  $\text{V}_{1-x}\text{Mo}_x\text{O}_2$  with  $0 \leq x \leq 0.60$  were obtained (Table 2.1). Attempts to obtain  $\text{V}_{1-x}\text{Mo}_x\text{O}_2$  with  $x > 0.60$  have all failed due to the formation of pure  $\text{MoO}_2$  and various molybdenum Magnéli phases. Since  $\text{Mo}^{4+}$  and  $\text{V}^{4+}$  are both found in products and in combination with the  $\text{Mo}^{5,6+}$  species, this points to the possibility of a miscibility gap in this composition regime. However, it is also possible that by exerting even more reducing conditions that the composition range may be extended.

### 2.3.3 Final Optimization

While  $\text{MoCl}_3$  provides good chemical control, the crystal size is not suitable for diffuse scattering measurements. Conversely, reactions using  $\text{TeCl}_4$  as the transport agent can provide large single crystals suitable for those measurements if  $\text{MoO}_2$  is used as the molybdenum source but, compositional control is lost because the transport of  $\text{MoO}_2$  occurs at a slower rate than that of  $\text{VO}_2$ . So, in order to average out the activity of the two metals while obtaining larger single

crystals, we elected to use ground polycrystalline  $V_{1-x}Mo_xO_2$  samples from the  $MoCl_3$  growth attempts as a starting reagent in a second CVT reaction, but with  $TeCl_4$  as the transport agent. This resulted in large (5mm x 0.5mm x 0.5mm), rod-shaped single crystals of  $V_{1-x}Mo_xO_2$  with output molybdenum compositions comparable to the input (Table 2.1), and no Mo-Te-O phases.

Finally, an unsuccessful synthesis of  $V_{1-x}Mo_xO_2$  without  $MoCl_3$  was attempted as a way to more easily obtain  $V_{1-x}Mo_xO_2$  powders, *i.e.* using a standard solid-state reaction. Apparently, the atmosphere of  $MoCl_2$  and  $MoCl_4$  gas from the decomposition of  $MoCl_3$  is necessary to avoid the formation of molybdenum Magnéli phases, especially for higher molybdenum compositions. It is possible that in this case, the formation of higher molybdenum oxide phases is driven by molybdenum oxide vapors that form in the sealed ampoule, and that the volatile molybdenum chlorides suppress their formation.

## 2.4 Conclusion

The synthesis of  $V_{1-x}Mo_xO_2$  has been optimized to obtain large single crystals through the use of a two-step CVT synthesis. This two-step synthesis was necessary to avoid unwanted side reactions with the transport agent while still being able to obtain large single crystals suitable for physical property measurements and diffuse scattering experiments. Additionally, by using an atmosphere of  $MoCl_2$  and  $MoCl_4$  to suppress the formation of volatile molybdenum oxide phases, both single crystal and polycrystalline samples of  $V_{1-x}Mo_xO_2$  can be obtained with higher molybdenum concentrations than what was possible through previous synthetic methods. Through further optimization of this synthesis, single crystals for the entire  $VO_2 - MoO_2$  compositional range might be possible. This type of two-step synthesis could prove beneficial in other crystal systems where CVT synthesis has previously failed due to reaction between starting materials and otherwise optimal transport agents.

## Supporting Information

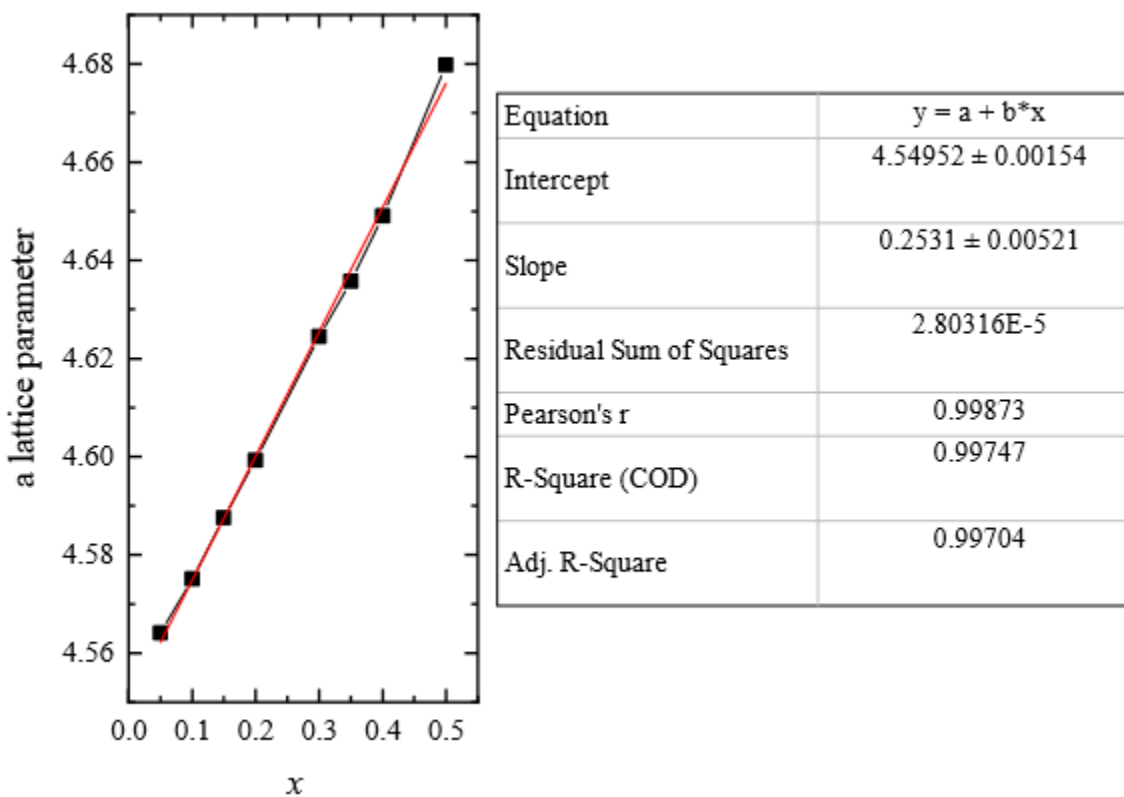


**Figure 2.4** Compositions were obtained by fitting the  $a$  lattice parameter of each sample to this linear fit of the  $a$  lattice parameters obtained by Holman et al.<sup>2</sup>



**Figure 2.5** Product of CVT growth with  $\text{VO}_2$ ,  $\text{V}_2\text{O}_3$ ,  $\text{MoO}_3$ , and  $\text{TeCl}_4$ . Byproducts pictured are  $\text{V}_2\text{O}_3$  and  $\text{TeMo}_5\text{O}_{16}$ .

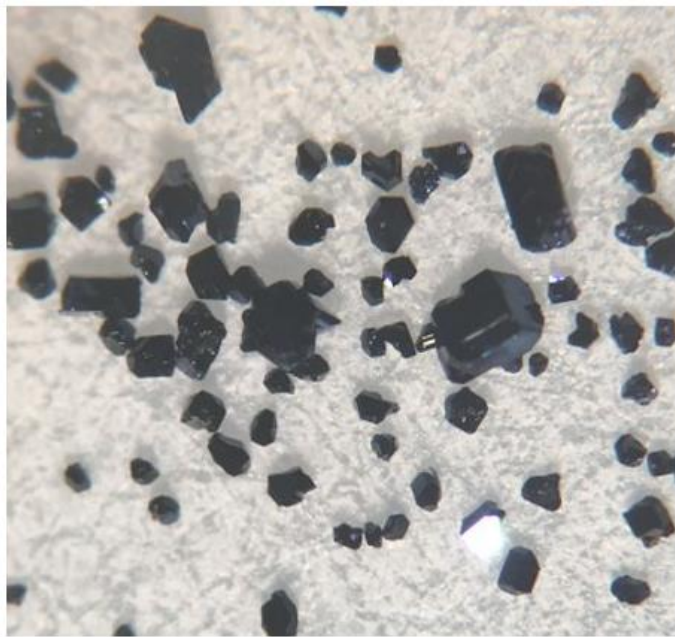


**Figure 2.6** Product of CVT growth with  $\text{VO}_2$ ,  $\text{V}_2\text{O}_3$ ,  $\text{MoO}_3$ , and  $\text{MoCl}_3$

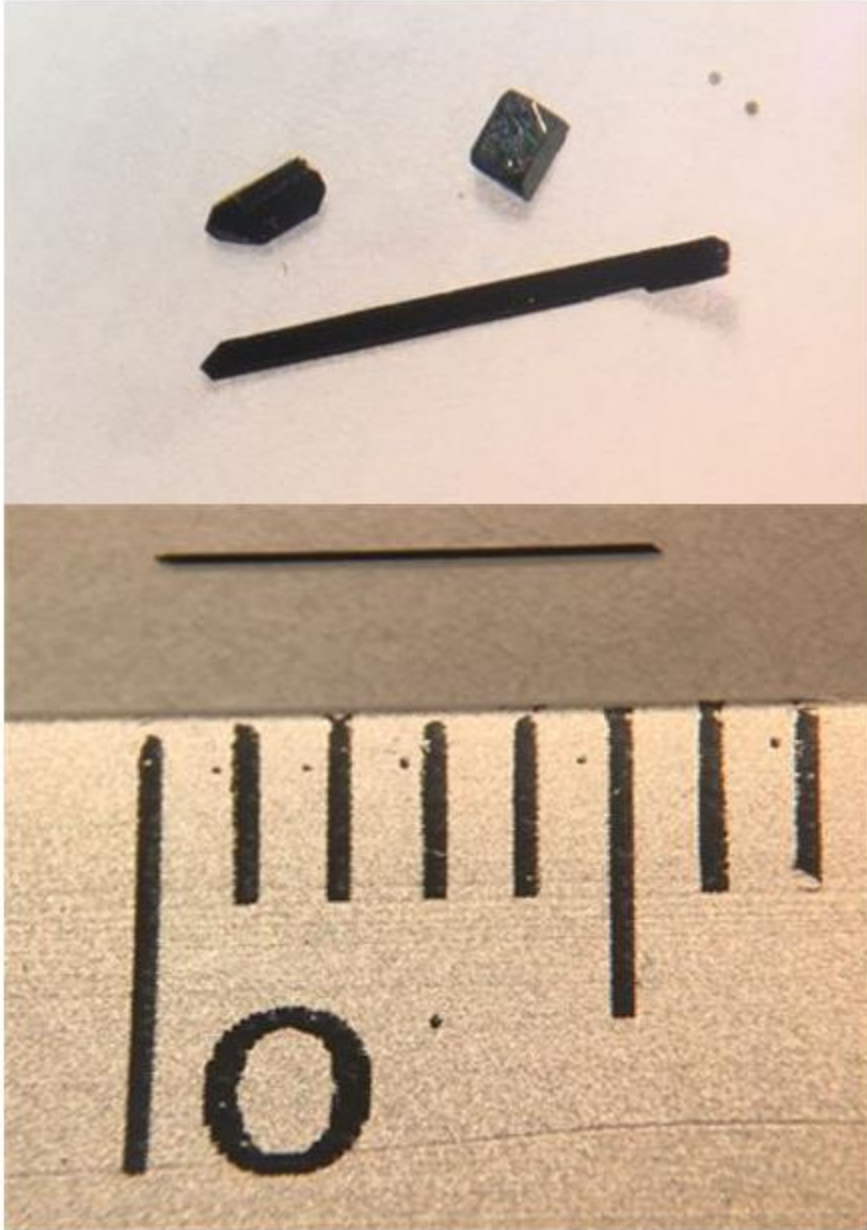


**Figure 2.7** Product of CVT growth using  $V_{1-x}Mo_xO_2$  and  $TeCl_4$

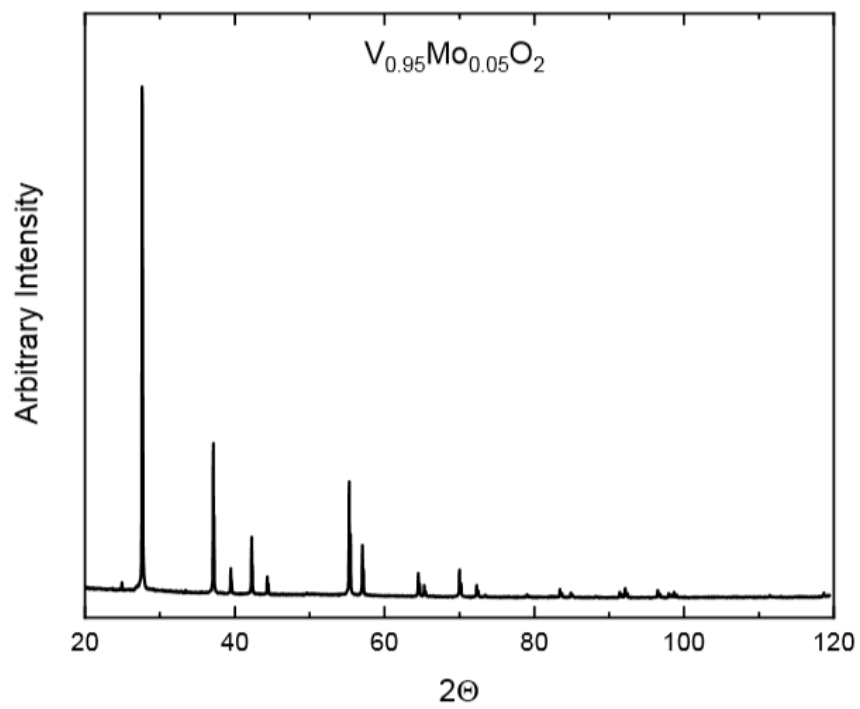


**Figure 2.8** PXRD Pattern of  $V_{0.95}Mo_{0.05}O_2$

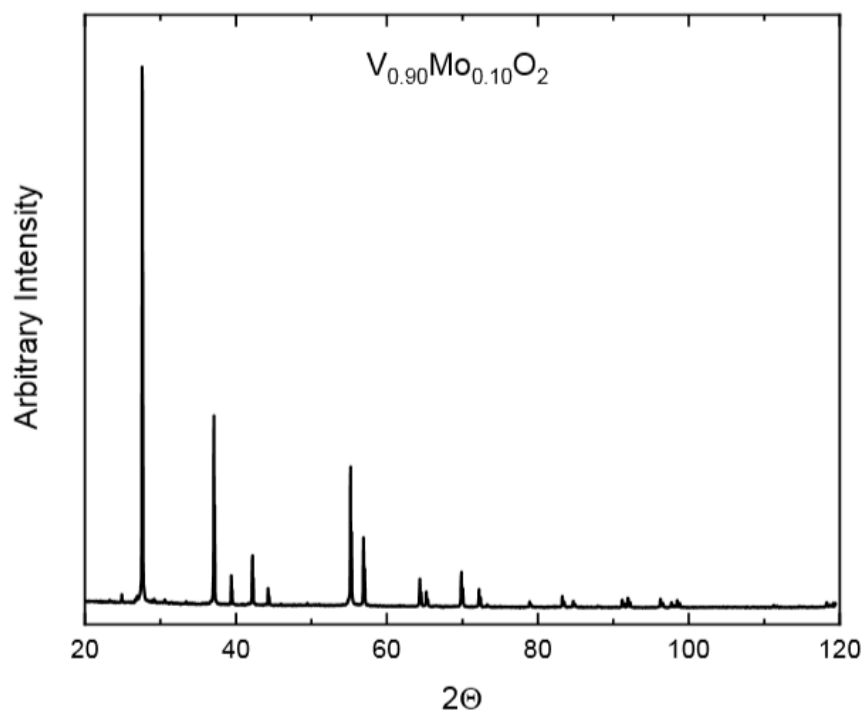


**Figure 2.9** PXRD Pattern of  $V_{0.90}Mo_{0.10}O_2$

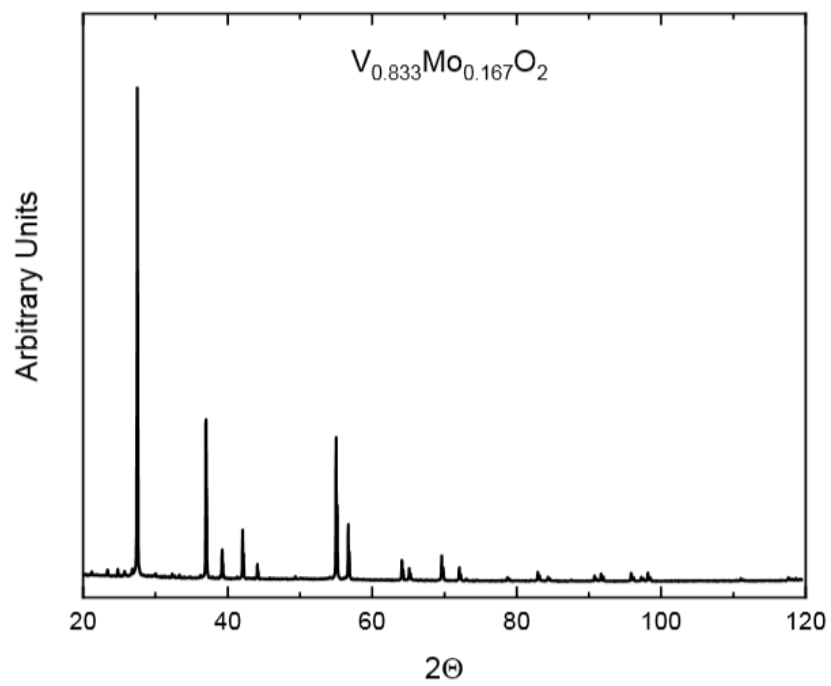


**Figure 2.10** PXRD Pattern of  $V_{0.833}Mo_{0.167}O_2$

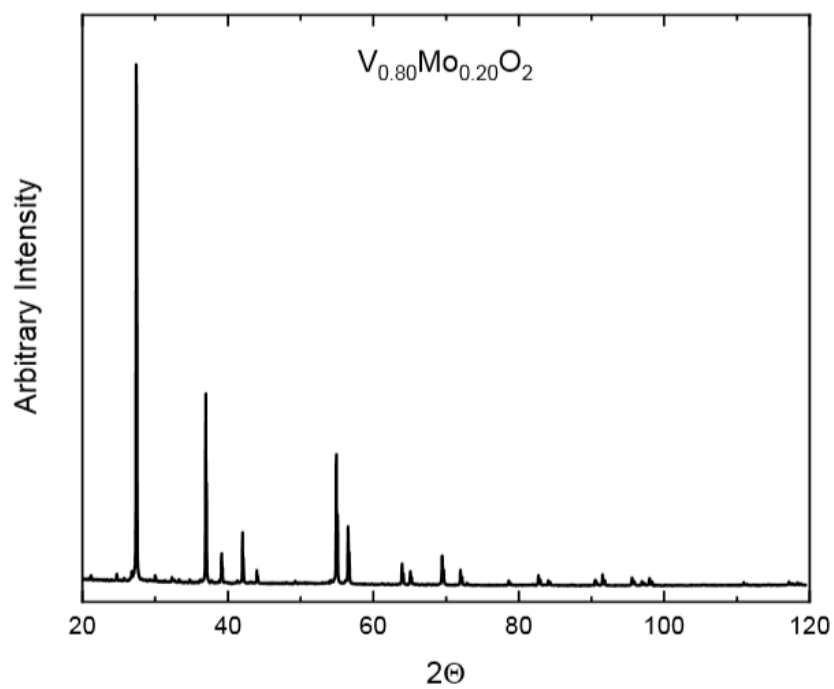


**Figure 2.11** PXRD Pattern of  $V_{0.80}Mo_{0.20}O_2$

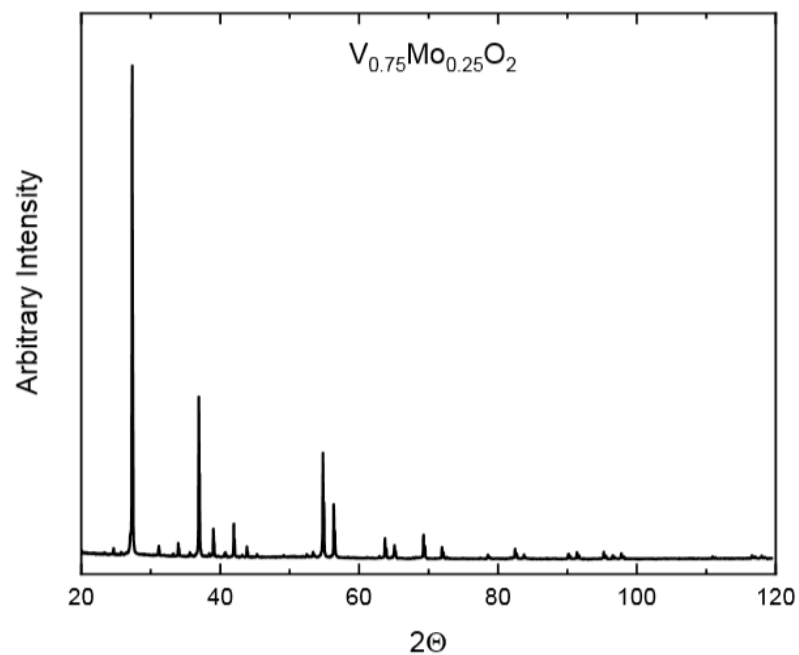


**Figure 2.12** PXRD Pattern of  $V_{0.75}Mo_{0.25}O_2$

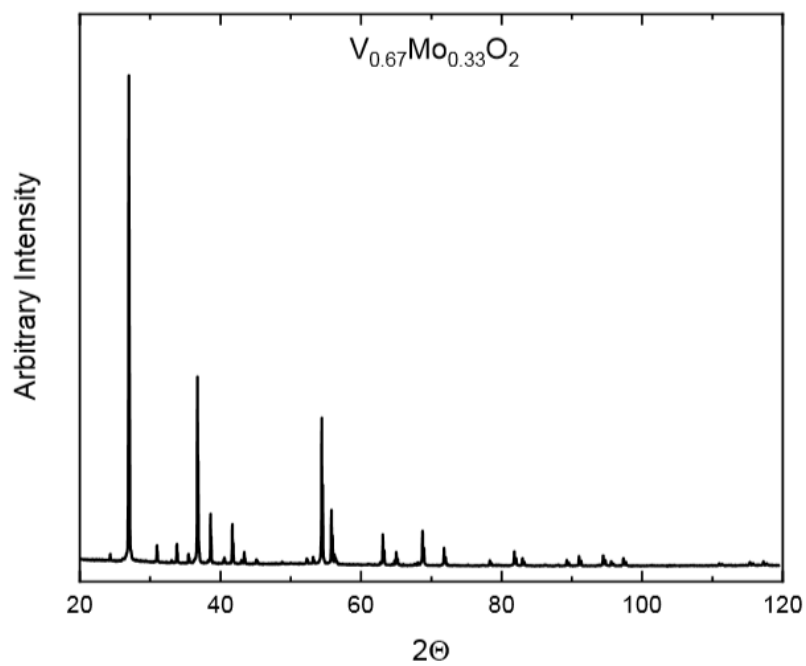


**Figure 2.13** PXRD Pattern of  $V_{0.67}Mo_{0.33}O_2$

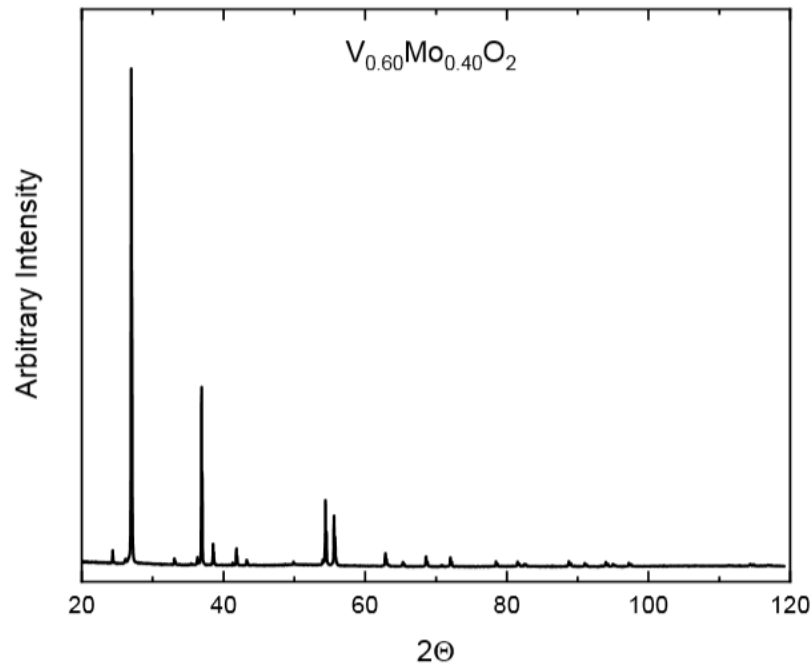


**Figure 2.14** PXRD Pattern of  $V_{0.60}Mo_{0.40}O_2$

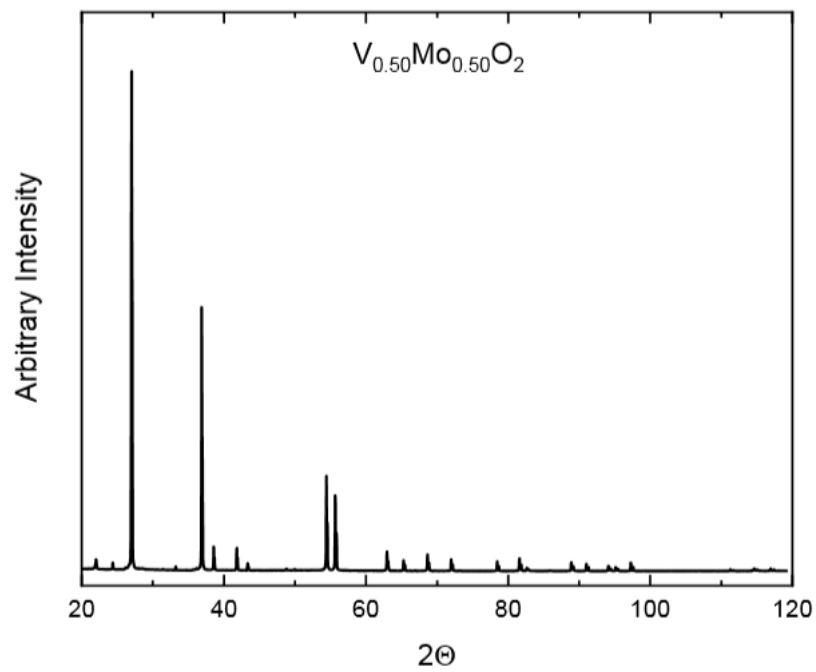


**Figure 2.15** PXRD Pattern of  $V_{0.50}Mo_{0.50}O_2$

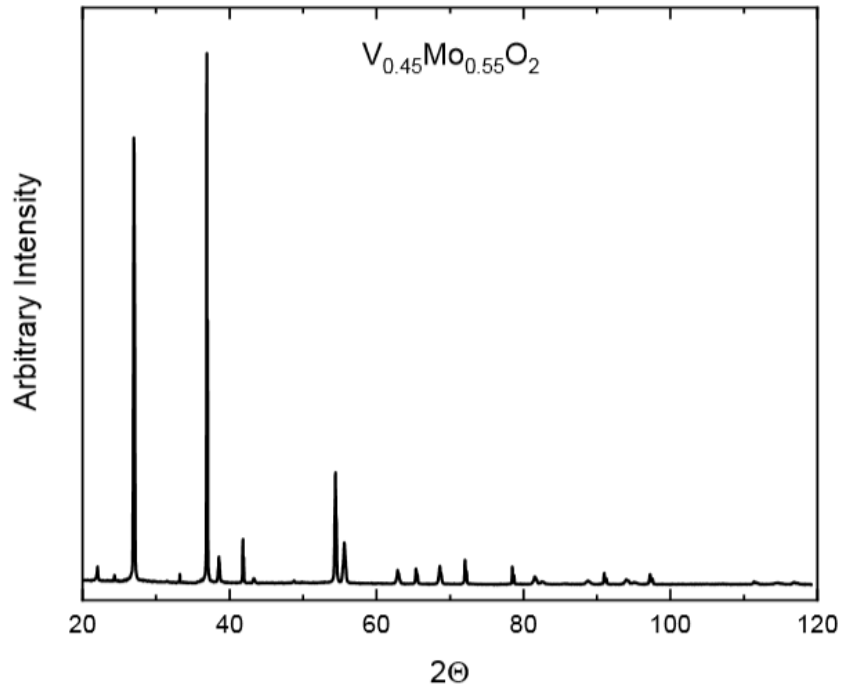


**Figure 2.16** PXRD Pattern of  $V_{0.45}Mo_{0.55}O_2$

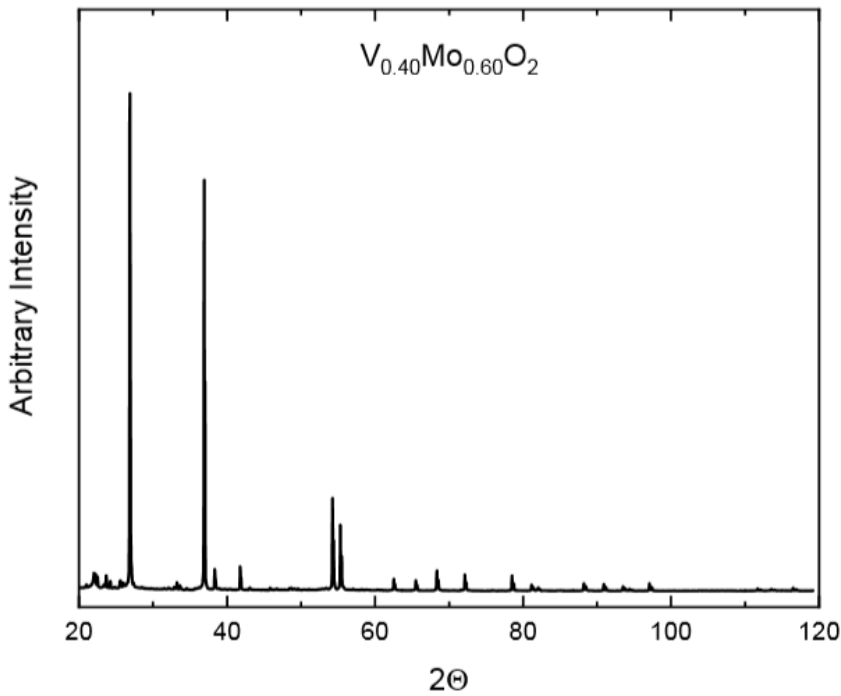


**Figure 2.17** PXRD Pattern of  $V_{0.40}Mo_{0.60}O_2$

## References

1. Davenport, M. A.; Douglas, T. C.; Chettri, T. B. R.; Confer, M. P.; Allred, J. M., Large Single Crystals of  $V_{1-x}Mo_xO_2$  from a Two-Step Chemical Vapor Transport Synthesis. *Cryst. Growth Des.* **2020**, *20* (6), 3635-3640.
2. Holman, K. L.; McQueen, T. M.; Williams, A. J.; Klimczuk, T.; Stephens, P. W.; Zandbergen, H. W.; Xu, Q.; Ronning, F.; Cava, R. J., Insulator to Correlated Metal Transition in  $V_{1-x}Mo_xO_2$ . *Phys. Rev. B.* **2009**, *79*, 245114.
3. Marinder, B. O., On the Phase Relations in the  $V_xMo_{1-x}O_2$  System ( $0 \leq x \leq 0.55$ ). *Mat. Res. Bull.* **1975**, *10*, 909-914.
4. Jin, P.; Tanemura, S.,  $V_{1-x}Mo_xO_2$  thermochromic films deposited by reactive magnetron sputtering. *Thin Solid Films* **1996**, *281/282*, 239-242.
5. Bando, Y.; Nagasawa, K.; Kato, Y.; Takada, T., Growth of  $VO_2$  Single Crystals by Chemical Transport Reaction. *Japan J. Appl. Phys.* **1969**, *8*, 633-634.
6. Allred, J. M.; Cava, R. J., Crystal structures of the high temperature forms of  $V_8O_{15}$  and  $V_9O_{17}$  and structural trends in the  $V_nO_{2n-1}$  Magnéli series. *J. Solid State Chem.* **2013**, *198*, 10-17.
7. Schmidt, P.; Binnewies, M.; Glaum, R.; Schmidt, M., Chemical Vapor Transport Reactions - Methods, Materials, Modeling. In *Advanced Topics on Crystal Growth*, Ferreira, S. O., Ed. InTechOpen: 2013.
8. Bunsen, R., Vulkanische exhalation. *J. Prakt. Chem.* **1852**, *56*, 53.
9. Arkel, A. E. V.; Boer, J. H. d., Darstellung von reinem Titanium-, Zirkonium-, Hafnium- und Thoriummetall. *Z. Anorg. Allg. Chem.* **1925**, *148*, 345.
10. Schafer, H., *Chemische Transportreaktionen: der Transport anorganischer Stoffe über die Gasphase und seine Anwendungen*. Verlag Chemie: Weinheim, 1962; p 142.

11. Schafer, H., Chemical Transport and Solubility of Solid in Gas-Phase. *Z. Anorg. Allg. Chem.* **1973**, 400, 242.
12. Toby, B. H., Expgui, a graphical user interface of gsas. *J. Appl. Crystallogr.* **2001**, 34, 210-213.
13. Larson, A. C.; Dreele, R. B. V., General structure analysis system (gsas). *Los Alamos National Laboratory Report* **2000**, 86-748.
14. Sheldrick, G. M., A short history of SHELX. *Acta. Cryst.* **2008**, 64 (1), 112-122.
15. Farrugia, L. J., WinGX Suite for Small-Molecule Single-Crystal Crystallography. *J. Appl. Crystallogr.* **1999**, 32 (4), 837-838.

## CHAPTER 3: FRAGILE 3D ORDER IN $V_{1-x}Mo_xO_2$

Chapter is being prepared for publication.

### 3.1 Introduction

As mentioned before, the high temperature (ht)  $VO_2$  is metallic due to the  $d^1 V^{4+}$  species, which somehow localizes into a paramagnetic state in low-temperature (lt) semiconducting  $VO_2$ . At this time, electron-electron correlations are considered by many to be fundamental to this localization process, possibly in combination with a Peierls instability.<sup>1-6</sup> Others still favor the primacy of a pure structural instability, suggesting previous calculations underestimated the effect of bond covalency, entropy, and/or orbital ordering.<sup>7-10</sup> As such, 60 years after its discovery, the current literature represents many different approaches and conclusions.<sup>11</sup>

What has become clear is that the structural instability is more complex than initially perceived, and it is not fully understood. The rutile structure of metallic  $VO_2$  (R) consists of two chains (A and B) of edge-sharing octahedra running along the  $c$  axis that are related by a  $4_2$  screw axis. The screw axis means that the A and B chains are not mutually equivalent by translation. The structure is shown looking across the chains in Figure 3.1.a and down the chains in Figure 3.1.b. Also shown are the M1 and M2 phases, which are both lt phases. Below the MIT, all of the metal atoms dimerize and an in-plane, non-dimerizing distortion (A chain in the  $[1,1,0]$  direction, B chain in the  $[-1,1,0]$  direction), yielding the M1 phase. The M2 phase forms upon addition of  $Cr^{3+}$ ,  $Al^{3+}$ , and  $Ga^{3+}$ , and is quite similar to the M1 phase, except only half

of the metal atoms dimerize (e.g. the A chain).<sup>9, 12-13</sup> The remaining B chain metal sites show the in-plane, non-dimerizing distortion.

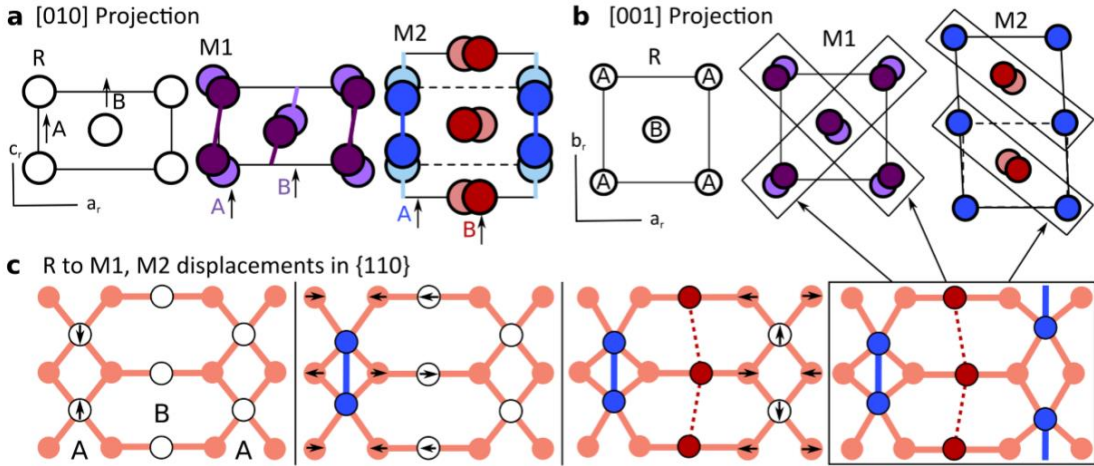


**Figure 3.1** (a) The [010]<sub>R</sub> projection of the tetragonal rutile (R) phase, the low temperature monoclinic (M1) structure of VO<sub>2</sub>, and the monoclinic (M2) structure. The same three structures are shown in (b) from the [001]<sub>R</sub> projection. Boxes are drawn around {110}<sub>R</sub> distortion planes. Oxygen atoms are both omitted from (a) and (b) for clarity. (c) Stepwise schematic showing the conventional understanding of dimer formation driving the long-range distortion in two dimensions within {110}<sub>R</sub>. The arrows pointing from the far-right panel to (b) are added to show how it projects onto the actual structures. M1 is a superposition of two orthogonal families of distortion planes.

Simple Coulombic arguments can be used to explain the connection between the dimer formation and non-dimerizing distortion and is illustrated in Figure 3.1.c. When a *M-M* bond forms along a given chain, the *c*-axis displacement of one *M* atom ( $d_z$ ) couples to the *ab* displacement of another atom ( $d_{xy}$ ) at  $[\frac{1}{2}, \frac{1}{2}, \frac{1}{2}]$  through the shared oxygen atom (Figure 3.1.c). This propagates in a network in the (110) planes, with two types of V atoms—those with only  $d_z$  and those with only  $d_{xy}$ . This network is entirely 2D, as described. In the M2 structure, 3D ordering occurs when the distortions propagate symmetrically along the *a* axis and antisymmetrically along the *b* axis (or *vice versa*). The M1 phase can be seen as simply a superposition of two, orthogonal M2 order parameters.

Several attempts have been made to more fully describe the connection between the M1 and M2 phases in tandem, including an all electron embedded Dynamical Mean Field Theory (DMFT) model by Brito *et al.*<sup>5</sup> Another approach was taken by Lovorn and Sarker, who instead used an Ashkin-Teller model, with displacements taking the place of spins, which resulted in several novel predictions.<sup>14</sup> They found that in order to make the 2D displacement network shown in Figure 3.1.c fully three-dimensional, inclusion of second-order terms to the Hamiltonian are required. These favored weak cooperative (*i.e.* ferroelectric) displacements in the [100] and [010] directions. This interaction is thus geometrically frustrated, and the 3D-M2 ordering is only stabilized by next-nearest neighbour interactions. However, there is still no model that can predict whether the M1 or M2 phase is more stable under a given set of conditions, nor why the M1 phase so often devolves into the M2 phase.

With this in mind and the single crystals from the previous chapter, the goal is to explore how the short range ordering in VO<sub>2</sub> changes as a function of molybdenum substitution. The logical starting point for this observation is around the phase boundaries where the M1 phase disappears near V<sub>0.8</sub>Mo<sub>0.2</sub>O<sub>2</sub> and where evidence of another monoclinic phase was seen in electron diffraction at V<sub>0.5</sub>Mo<sub>0.5</sub>O<sub>2</sub>. In this chapter, we explore a unique diffuse scattering feature in V<sub>0.81</sub>Mo<sub>0.19</sub>O<sub>2</sub> at the phase boundary where the first M1 phase disappears.

### **3.2 Experimental**

Total scattering data was collected at the Advanced Photon Source (APS) at Argonne National Lab (ANL) on sector 6-ID-D. The experiment used an incident beam energy of 87 keV. The detector was a Dectris Pilatus CdTe 2M detector, held at a distance of 650 mm, with a threshold detection limit set to 43 keV. Samples were mounted on Kapton capillaries using either GE varnish or Duco cement. Goniometer geometry allowed free rotation of  $\varphi$ , limited  $\omega$ ,

and fixed  $\chi$  at  $90^\circ$ . Every temperature scan had three  $360^\circ$   $\varphi$  scans, at  $\omega = 0, -15, +15$ . The second and third sub-scans also included a shift of the detector of  $5 \text{ mm} \times 5 \text{ mm}$  and  $10 \times 10 \text{ mm}$ . The detector and  $\omega$  shifts were to correct for gaps in the detector and blooming artefacts. The data were processed using NeXpy, and transformed using the crystal coordinate transformation work-flow (CCTW).<sup>15-16</sup> Sample temperature was controlled using an Oxford Cryosystems nHelix. A 3D- $\Delta$ PDF map was created using a modification of the punch and fill method developed by Weber et al.,<sup>17-18</sup>: by taking a Fourier transform of a symmetrized reciprocal space map of the diffuse scattering only. The symmetrization used the following symmetry operators:  $C_{2x}$ ,  $C_{2y}$ ,  $C_{4z}$ ,  $\sigma_x$ ,  $\sigma_y$ ,  $\sigma_z$ , and  $i$ . The Bragg scattering was removed by punching out a sphere of  $0.01 \text{ r.l.u}$  around each integer point, and then filling the hole by convolving the existing data with a Gaussian kernel using the astropy library.<sup>19-20</sup> In the case of 19% Mo we focused on the diffuse scattering rods in the  $hk0$  plane, so instead of punching out Bragg peaks, the entirety of each  $hkn$  ( $n = \text{integer}$ ) plane was removed. Since most of the diffuse scattering is found in the  $L/2$  planes, the difference between this and a standard punch and fill method is small, extending only a few unit cells in the PDF. However, in this material the modified method's 3D- $\Delta$ PDF map is much less noisy, and with fewer Fourier transform artefacts. The standard punch and fill was used for 17% Mo, and only the rutile subcell peaks were punched out.

A single-domain crystal of  $\text{VO}_2$  with size  $100 \times 100 \times 50$  unit cells was simulated in the program DISCUS,<sup>21</sup> with the computation time being decreased through the use of an additional program, SCATTY.<sup>22</sup> In the model, oxygen atoms are omitted and each corner vanadium site is displaced by  $\pm \delta_{ab}$  along the  $(110)$  direction in the  $ab$  plane. The displacements of these atoms were initially randomized, then swapped with each other via a Monte Carlo procedure using an Ising-type Hamiltonian shown in Equation 1.

$$H = \sum J_1 \sigma_+ \sigma_- + J_2 \sigma_+ \sigma_- + J_3 \sigma_+ \sigma_- \quad \text{Eq. 1}$$

An atom displaced along the positive (110) direction is represented by  $\sigma_+$  and one displaced along the negative (110) direction by  $\sigma_-$ .  $J_1$  and  $J_2$  represented strong antiferromagnetic interactions between nearest neighbors along the (110) direction and the (001) direction, respectively.  $J_3$  represents interactions between nearest neighbors along  $\langle 100 \rangle$  directions. Once the displacements of the corner atoms were determined, the center site atoms were displaced along the  $c$  axis by  $\pm \delta_c$  to minimize Coulomb repulsion (if the two displacements were equivalent, the displacement was chosen at random). Scattering from these simulated crystals was then calculated using the program SCATTY,<sup>22</sup> with tetragonal  $4/mmm$  point group symmetry applied in the calculation.

For all simulations,  $J_1$  and  $J_2$  were set to 10 kT. A range of  $J_3$  values from -10 to 10 in steps of 1 were tested, with  $J_3 = -2\text{kT}$  producing ripples most similar to observed data. Further calculations were performed on this simulated crystal varying  $\delta_{ab}$  and  $\delta_c$ , with each displacement pair scored by relative rod intensities compared to those experimentally measured. The pair  $\delta_{ab} = 0.207 \text{ \AA}$  and  $\delta_c = 0.21 \text{ \AA}$  produced the best fit of relative rod intensities and was used for comparison.

### 3.3 Total Scattering Data

In the X-ray total scattering data, sharp rods of scattering were observed below 150 K in  $x = 0.19$  (19 % Mo) at  $l = n/2$  planes, where  $n$  is an integer. Figure 3.1.a-e show the temperature dependence of the  $(hk \frac{1}{2})$  plane in 19% Mo. The scattering is mostly constant below 140 K, with small changes in intensity and linewidth, down to the minimum measured temperature, 30 K. The detailed view from a  $(hk \frac{3}{2})$  slice ( $h$ ), shows that the scattering rods actually have a periodic

bending to them. At 150 K (Figure 3.2.c), the rods have weakened and broadened substantially, and by 160 K only weak diffuse scattering is visible, persisting to room temperature.

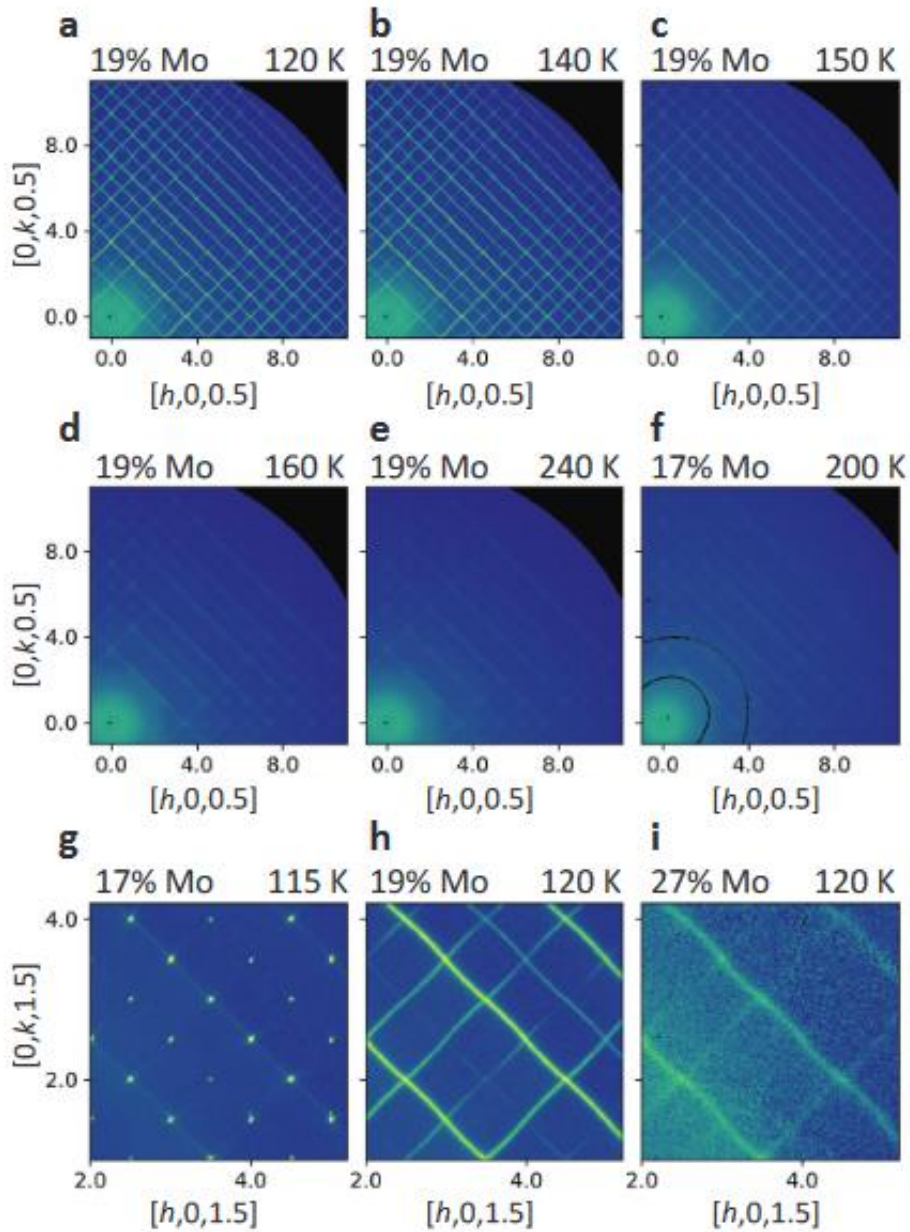


**Figure 3.2** Reciprocal lattice slices from  $V_{1-x}Mo_xO_2$ . (a-e) Temperature dependence of the  $l = 0.5$  slices of  $x = 0.19$ , at  $T = 120, 140, 150, 160,$  and  $240$  K, respectively. (f)  $x = 0.17$  at  $200$  K, with same slice as above. (g-i) Composition dependence of the  $l = 1.5$  low temperature structures at  $x = 0.17, 0.19,$  and  $0.27$ . Coordinates are given in the reciprocal lattice vectors of the parent rutile unit cell.

According to a standard single crystal X-ray diffraction structure solution, the 17% Mo crystal exhibits the normal structural phase transition to the M1 phase at 168 K. Figure 3.2.f-g show that the high temperature scattering for this composition is essentially equivalent to 19% Mo, and that Bragg peaks are observed at  $[\frac{h}{2}, 0, \frac{l}{2}]$  below the transition. A crystal with 27% Mo (i) shows the same network of rods as 19% Mo, except with a reduced intensity and correlation length.

The cross-section of the scattering rods in the  $[hh0]^*$  and  $[00l]^*$  axes can be fit to a Pseudo-Voigt function. The correlation length,  $\xi$  was calculated from the Lorentzian line width component using the expression  $\xi = \frac{1}{L}$  where  $L$  is the line width in reciprocal lattice coordinates ( $\text{\AA}^{-1}$ ). Fitting the  $T$  dependence of  $\xi$  to a power law  $\xi = A(1 - \frac{T}{T_s})^\beta$  gives a transition temperature of 151.0(3) K and a critical exponent of  $\beta = 0.109(18)$  according to the  $[hh0]^*$  cross-section. The resulting  $\xi_{xx}$  and  $\xi_z$  are plotted in Figure 3.3.a as red and blue circles, respectively. The maximum intensity of the scattering rods occurs around 120 K. Cuts from the 3D- $\Delta$ PDF are shown in Figure 3.4a-f. The 17% Mo phase again serves as a standard for usual 3D M1 ordering (Figure 3.4a), with long-range correlations along all crystallographic axes. This is in contrast to the unusual two-dimensional scattering observed in 19% Mo (Figure 3.4.b). In the latter, the strongest correlations fall along (110) and (1-10) planes, as expected from the scattering rod orientations. The two crossed planes must be independent scattering from different regions that are twinned on the nanoscale. That is, some regions have strong correlations in the (110) direction and others have strong (1-10) correlations, but not both. Otherwise, the cooperation of both correlation directions should give a 3D correlation, *e.g.* sharp Bragg peaks. Within the planes of high intensity (Figure 3.4.c-f), there are intense positive and negative peaks at integer points,  $[u, u, w]$ , corresponding to correlations commensurate with the

unit cell. There is also a quadrupolar feature of intensity centered at  $[\frac{u}{2}, \frac{u}{2}, \frac{w}{2}]$  positions (*e.g.* vectors connecting cell corners to the body centers, and *vice versa*). Weaker dipolar features are also observed around the points  $[\frac{u}{3}, \frac{u}{3}, w]$ ,  $[-\frac{u}{3}, -\frac{u}{3}, w]$ ,  $[\frac{u}{6}, \frac{u}{6}, \frac{w}{2}]$ , and  $[-\frac{u}{6}, -\frac{u}{6}, \frac{w}{2}]$ .

Beyond the principal  $\{110\}$  planes, there are weaker planes of correlations that alternate with essentially zero intensity along the adjacent diagonals, except the first off-diagonal plane, which does show significant intensity (about one fifth the intensity of principal diagonal sites).

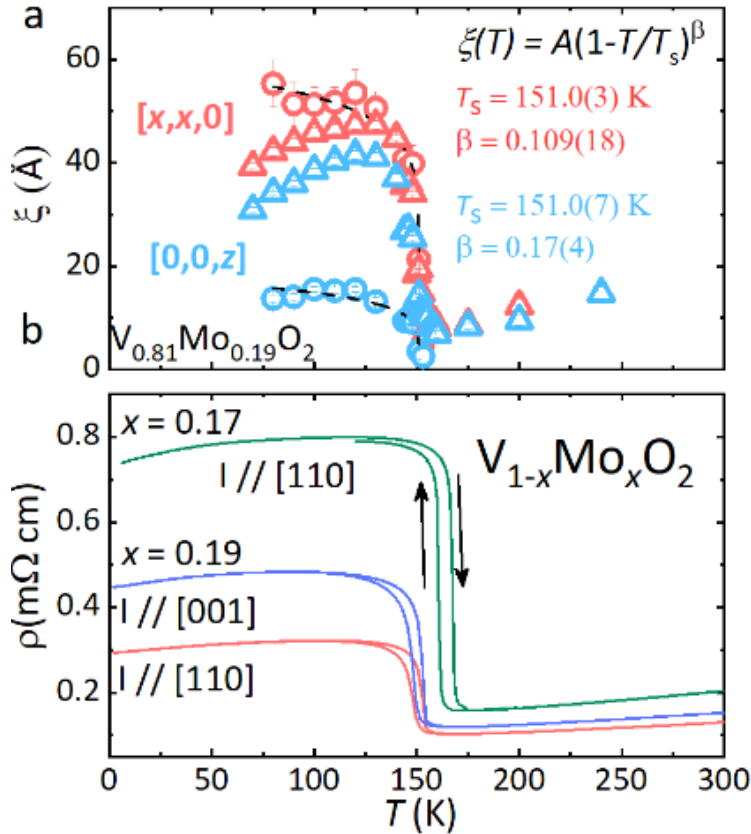


**Figure 3.3** (a) Temperature dependence of the correlation length,  $\xi$ , of 19% Mo as determined from fitting the peak width from the scattering data (circles) and from the 3D- $\Delta$ PDF (triangles). Red and blue symbols are for the  $[x,x,0]$  and  $[0,0,z]$  directions, respectively. (b) Resistivity,  $\rho$ , vs temperature of selected orientations of the 17% and 19% Mo crystals.

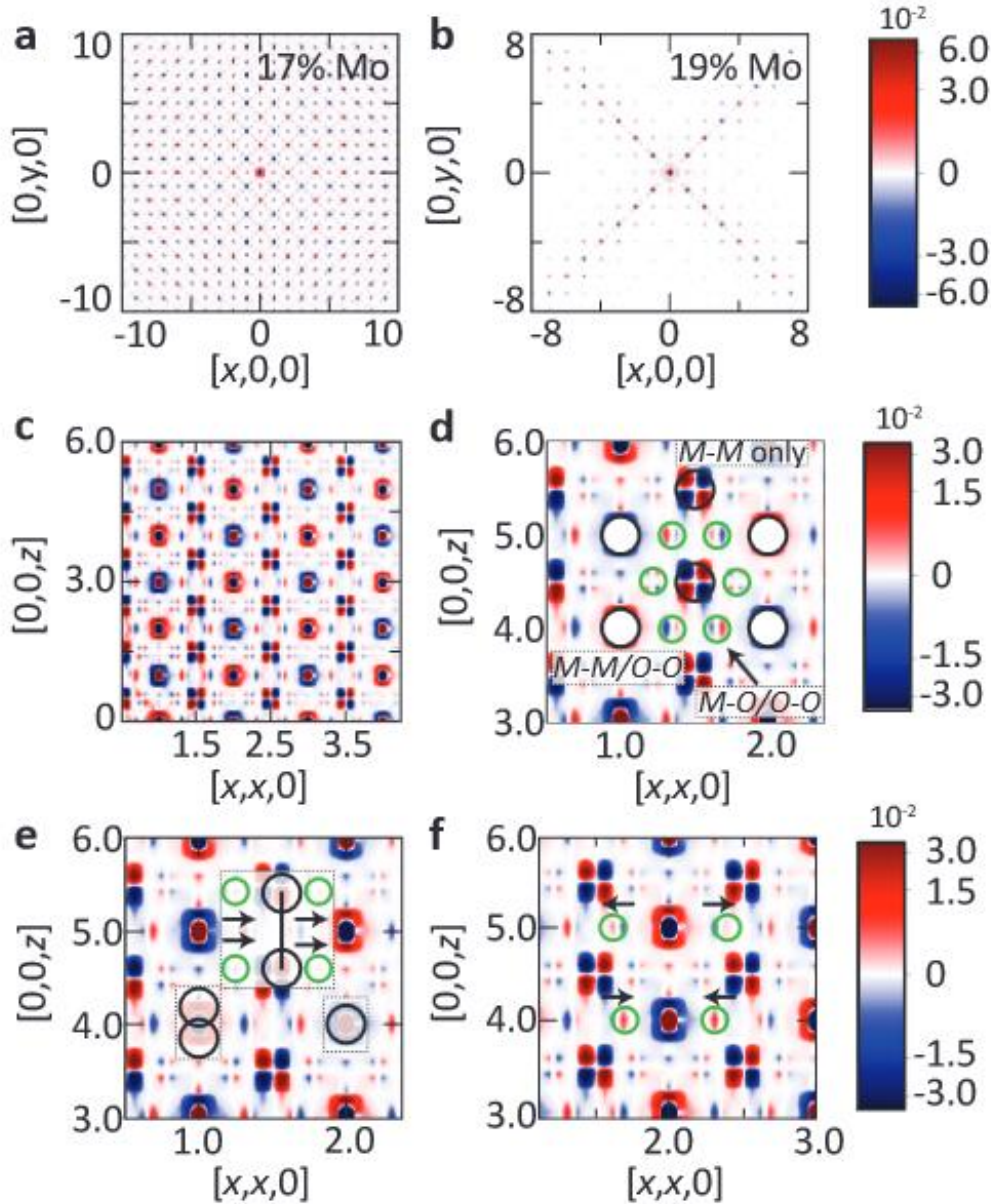


**Figure 3.4** Symmetric log plots of the 3D- $\Delta$ PDF correlation maps from (a) 17% Mo and (b) 19% Mo at 115 and 120 K, respectively, parallel to the (001) plane at  $z = 0$ . (c) Section of the slice from the (110) plane. (d-e) Detailed views of the same slice with drawing showing the various types of lattice vectors that are observed. (d) Placement of the three types of interatomic vectors in the average rutile structure; large filled circles are on integer points and correspond to equivalent atom positions both M-M and O-O vectors. Large empty circles in black are at  $[\frac{u}{2}, \frac{v}{2}, \frac{w}{2}]$  points, and only correspond to interchain M-M vectors. Small green circles correspond to both M-O and O-O vectors, which approximately overlap with each other near  $[0.35, 0.35, z]$  points. (e) and (f) use the same scheme, except the shapes are drawn over maxima in the 3D- $\Delta$ PDF correlation map. (e) shows how the interchain peaks are consistent with local dimer formation, and (f) shows a scheme consistent with the intrachain O atom displacements. The colormap inside the boxes in (e) is muted for clarity. The signal intensity is normalized to unity.

### 3.4 Interpretation and modelling of the 3D- $\Delta$ PDF

The oscillation of positive/negative intensity at each integer point in the 3D- $\Delta$ PDF shows the periodicity of local correlations. By definition, each integer site connects sites that are translationally equivalent in the crystalline (*i.e.* rutile) model. Negative (blue) correlation implies broken translation symmetry at that vector, while a positive (red) correlation means the symmetry is maintained. It is clear that the local planar cell is doubled on each axis, but also centered, giving a new cell with double the area.

Vectors at half-integer points in the plot must correspond to interchain metal-metal ( $M$ - $M$ ) correlations. The  $z$  component of the displacement around the body-center sites and the two strong lobes above and below each integer vector are clear evidence that there are strong dimerizing correlations between some metal sites. The  $[x, x, 0]$  component of the quadrupole feature shows that at least one site has a  $d_{xy}$  displacement. The fact that there is no orthogonal shift in the cross-section of the same feature shown in Figure 3.4.b, shows that the dimerization is dissimilar to the M1 structure. In the M1 phase,  $d_{xy}$  causes buckling between atoms in the neighboring dimer along the diagonal (Figure 3.1.c), so they do not lie along the same  $z$  axis as they do in this 3D- $\Delta$ PDF map. Instead, they should be displaced off of the diagonal, which is obviously not the case in Figure 3.4. This relationship looks much closer to the M2 structure, where the dimerized  $d_z$  atoms contain no  $d_{xy}$ , and the undimerized set do. This would explain why every pair in the 3D- $\Delta$ PDF map is offset laterally as a whole. This is consistent with the dipolar features at  $[\frac{u}{3}, \frac{u}{3}, w]$  and  $[\frac{u}{6}, \frac{u}{6}, \frac{w}{2}]$  sites, which correspond to M-O and O-O interatomic vectors. They show a commensurate shift that is in agreement with the M2 interpretation. In this sense, the (110) cut of the 3D- $\Delta$ PDF map can be interpreted as a 2D cut of the M2 phase on the  $(110)_R$ . This interpretation is illustrated in Figure 3.5 by showing the correlations between the

3D- $\Delta$ PDF map and the corresponding real space vectors. This structural model will be referred to as the ‘2D-M2’ model. The correlations are very strong, and remain measurable in the 3D- $\Delta$ PDF at least to 25 unit cell diagonals (about 20 nm), but die off within just a few unit cells ( $\sim$  nm) in the orthogonal axis.

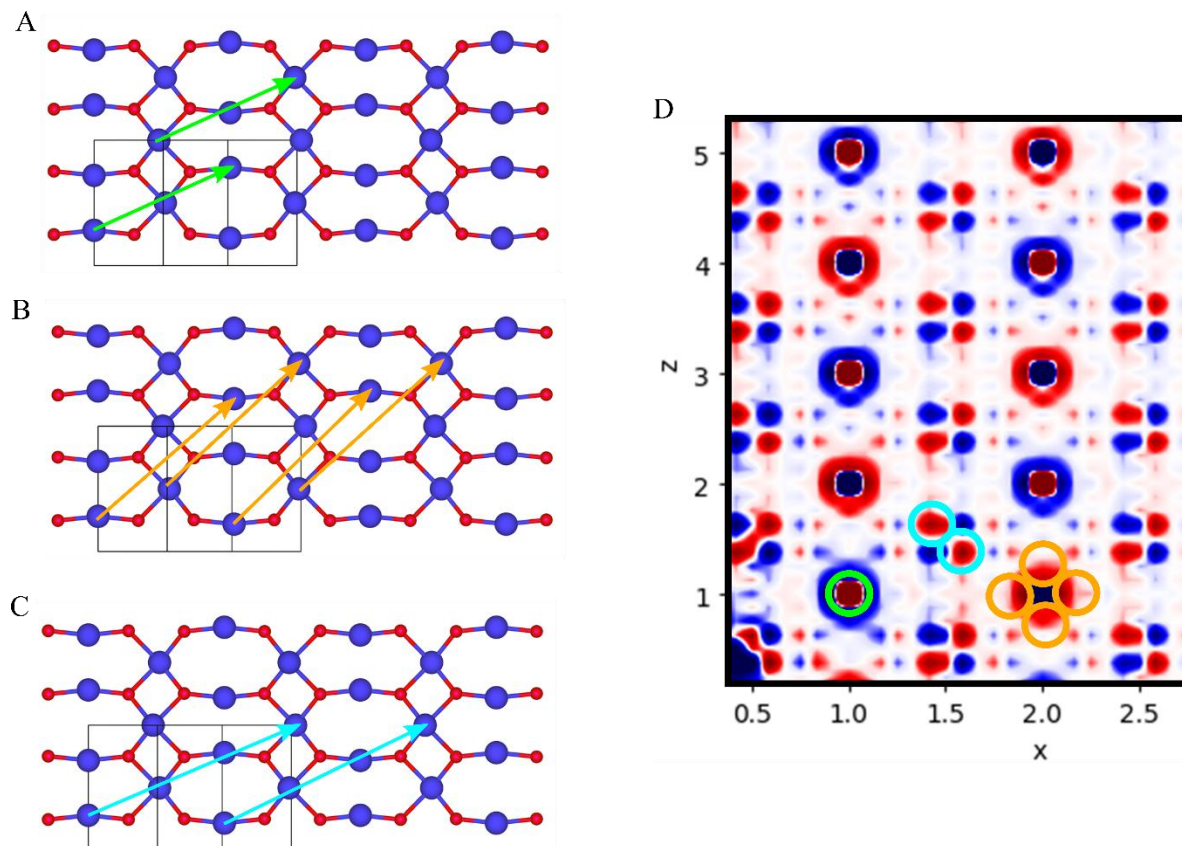


**Figure 3.5** The correlation between the real atom displacements and the 3D- $\Delta$ PDF map showing the probability of finding an atom. Increased positivity is in red and decreased probability is in blue. There are four possible deviations for each metal atom in the M2 phase, two possibilities for each chain of metal atoms. These are  $(x+\delta, y+\delta, z)$ ;  $(x-\delta, y-\delta, z)$ ;  $(x, y, z+\delta)$ ; and  $(x, y, z-\delta)$ . Atoms that are separated by the  $(1, 1, 1)$  lattice vector (A) are always displaced in the opposite direction giving a positive probability of finding the atom centered around the  $(1, 1, 1)$  point in panel D. Unlike the  $(1, 1, 1)$  lattice vector, atoms separated by the  $(2, 2, 1)$  lattice vector (B) have displacements in the same directions leading to four lobes of positive probability in panel D with the dimer formation leading to the positive probability at  $(2, 2, 1+2\delta)$  and  $(2, 2, 1-2\delta)$  and the non-dimerizing distortion leading to positive probability at  $(2+2\delta, 2+2\delta, 1)$  and  $(2-2\delta, 2-2\delta, 1)$ . Displacements in the xy direction and the z direction (C) are coupled in atoms separated by the  $(1.5, 1.5, 1.5)$  lattice vector with displacements resulting in the vector always being smaller in one direction and larger in the other. These displacements are seen in the two-lobe positive probability in panel D at  $(1.5+\delta, 1.5+\delta, 1.5-\delta)$  and  $(1.5-\delta, 1.5-\delta, 1.5+\delta)$ .

In order to test this interpretation, metal-only 2D-M2 models were constructed by Matt Krogstad, a collaborator at Argonne National Laboratory, using the programs Yell and DISCUS, for both the X-ray scattering and 3D- $\Delta$ PDF.<sup>21, 23-24</sup> Figure 3.6 shows the results of these simulations (right) compared to observations (left). The match between experiment and model appears successful, given that there was no actual parameter fitting involved; the observed data was simply used for scaling. It is clear that the constructed 2D-M2 model naturally conforms to the observation, even down to the relative intensities of the scattering rods. Note that one extra parameter, ferroelectric correlations along the [100] and [010] axes, was required in the diffuse scattering simulations to reproduce the wave-like bending of the scattering rods. The weak ferroelectric correlations are frustrated by the main in-plane correlation. This will be discussed further below. The calculated 3D- $\Delta$ PDF map reproduces the integer lattice vectors features and the body centred quadrupolar features. The weaker dipolar features attributed to oxygen atoms are missing, as expected.

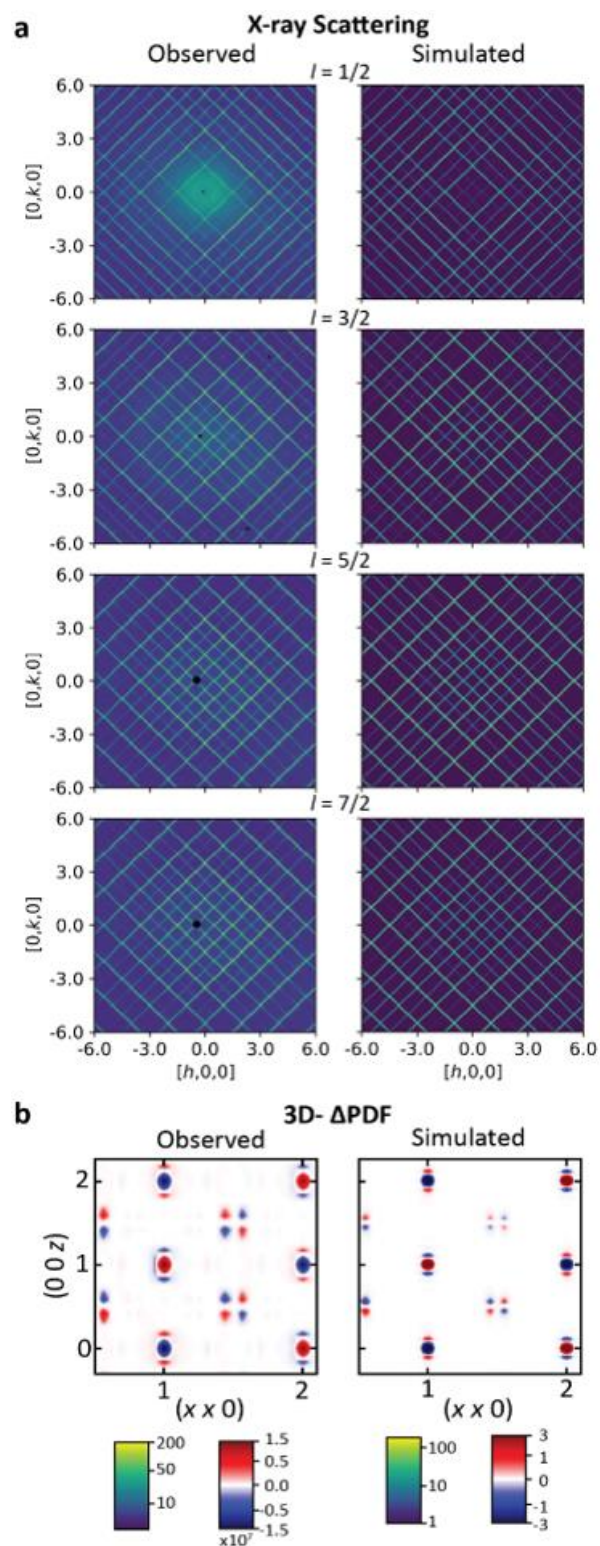


**Figure 3.6** (a) Comparison of observed diffuse scattering from various slices, on left, to the simulated scattering model, on right. (b) Comparison of observed 3D- $\Delta$ PDF, on left, to the calculated disorder model, on right.

### 3.5 Discussion

The constructed models validate the 2D-M2 interpretation of the data. Combining this with the other structural and electronic properties we have measured, we can state that the 2D-M2 is a different thermodynamic phase from both the long-range M1 and R phases. The transition from 2D-M2 to R is a first-order, metal-to-metal phase transition. Compositionally, the structural instability in  $V_{1-x}Mo_xO_2$  changes from M1 to 2D-M2 ordering quite discontinuously between  $0.17 < x \leq 0.188$ . The transition is very similar to the observed  $V_{1-x}Cr_xO_2$  phase behavior, except that here the M2-like phase only has medium-range order in two dimensions and very short-range order in the third dimension. Another difference is that Cr-substitution immediately ( $x \leq 0.015$ ) suppresses M1 in favor of M2. For Mo-substitution, the M1 structure is robust up to  $x = 0.18$ , before suddenly disappearing.

This fragility implies that long-range order of displacements is somehow independent between the orthogonal sets of  $\{110\}$  planes, and that  $x = 0.19$  corresponds to the point where two order parameters diverge. This is reminiscent to the ‘embedded 2D crystal model’ proposed by Lovorn and Sarker.<sup>14</sup> In accordance with the Lovorn-Sarker Ashkin-Teller displacements model, the critical composition near  $x = 0.19$  is when order parameters become  $m_A \neq 0 \neq m_B$ . They predicted that in this case, interactions between the  $\langle 110 \rangle$  and  $\langle 100 \rangle$  directions are geometrically frustrated and prevent ordering along both directions simultaneously. Instead, regions with strongly coupled displacements in either  $[110]$  or  $[1-10]$  planes form. This is exactly what we required to explain the wavy feature in our diffraction data. Another feature of the geometric frustration is that only the odd numbered pairs of parallel are frustrated, while the even-numbered neighbors still have some correlations. It is also consistent with the observed 3D- $\Delta$ PDF map. It is important that the disordered dimension in the 2D-M2 phase would be

symmetrically equivalent to one of the ordered ones in the ht-R phase. To our knowledge an ordered state like this has never been observed experimentally in rutile or any other extended solid.

### 3.6 Conclusions

We have uncovered a new type of ground state in  $V_{1-x}Mo_xO_2$ , 2D-M2, governed by largely 2D ordering of atomic displacements. This type of long-range two-dimensional ordering phase is unprecedented, not only in  $VO_2$  or the rutile system, but in any kind of oxide. The observation of the structure indicates there may be many structural aspects in the rutile system that we could be missing that need to be studied in detail. We have shown that the structure is driven by geometric frustration, and that the properties of this phase support a Mott-Peierls mechanism as its origin. The real structure would have been impossible to describe using conventional crystallographic techniques, showing the power of the new 3D- $\Delta$ PDF method. A full electronic structure treatment of the 2D-M2 remains to be determined. The extremely sharp diffraction features indicate that most of the correlations derive from static order, but there may be a dynamic component, which could be revealed using inelastic X-ray/neutron scattering. The 2D-M2 phase weakens with increasing Mo content, but does exist at least up to  $x = 0.3$ . A systematic study of the structural parameters in detail over a wide compositional range may reveal how the fundamental order parameters evolve, which may help explain what conditions are required for the 2D-M2 state to manifest. This could result in a more complete physical model for  $VO_2$  and the underlying physics universal to all open shell rutile phases.

## References

1. Haverkort, M. W.; Hu, Z.; Tanaka, A.; Reichelt, W.; Streltsov, S. V.; Korotin, M. A.; Anisimov, V. I.; Hsieh, H. H.; Lin, H. J.; Chen, C. T.; Khomskii, D. I.; Tjeng, L. H., Orbital-Assisted Metal-Insulator Transition in VO<sub>2</sub>. *Phys Rev Lett* **2005**, *95* (19), 196404.
2. Weber, C.; O'Regan, D. D.; Hine, N. D. M.; Payne, M. C.; Kotliar, G.; Littlewood, P. B., Vanadium Dioxide: A Peierls-Mott Insulator Stable against Disorder. *Phys Rev Lett* **2012**, *108* (25), 256402.
3. Holman, K. L.; McQueen, T. M.; Williams, A. J.; Klimczuk, T.; Stephens, P. W.; Zandbergen, H. W.; Xu, Q.; Ronning, F.; Cava, R. J., Insulator to Correlated Metal Transition in V<sub>1-x</sub>Mo<sub>x</sub>O<sub>2</sub>. *Phys. Rev. B.* **2009**, *79*, 245114.
4. Wentzcovitch, R. M.; Schulz, W. W.; Allen, P. B., VO<sub>2</sub>: Peierls or Mott-Hubbard? A view from band theory. *Phys. Rev. Lett.* **1994**, *72* (21), 3389.
5. Brito, W. H.; Aquiar, M. C. O.; Haule, K.; Kotliar, G., Metal-Insulator Transition in VO<sub>2</sub>: A DFT + DMFT Perspective. *Phys Rev Lett* **2016**, *117* (5), 056402.
6. Huffman, T. J.; Hendriks, C.; Walter, E. J.; Yoon, J.; Ju, H.; Smith, R.; Carr, G. L.; Krakauer, H.; Qazilbash, M. M., Insulating phases of vanadium dioxide are Mott-Hubbard insulators. *Phys Rev B* **2017**, *97* (7), 075125.
7. Budai, J. D.; Hong, J.; Manley, M. E.; Specht, E. D.; Li, C. W.; Tischler, J. Z.; Abernathy, D. L.; Said, A. H.; Leu, B. M.; Boatner, L. A.; McQueeney, R. J.; Delaire, O., Metallization of Vanadium Dioxide Driven by large Phonon Entropy. *Nature* **2014**, *515*, 535-539.
8. Wall, S.; Yang, S.; Vidas, L.; Chollet, M.; Glownia, J. M.; Kozina, M.; Katayama, T.; Henighan, T.; Jiang, M.; Miller, T. A.; Reis, D. A.; Boatner, L. A.; Delaire, O.; Trigo, M., Ultrafast disordering of vanadium dimers in photoexcited VO<sub>2</sub>. *Science* **2018**, *362*, 572-576.
9. Hiroi, Z., Structural instability of the rutile compounds and its relevance to the metal-insulator transition of VO<sub>2</sub>. *Progr. Solid State Chem.* **2015**, *43*, 47-69.

10. Xu, S.; Shen, X.; Hallman, K. A.; Haglund, R. F.; Pantelides, S. T., Unified band-theoretic description of structural, electronic, and magnetic properties of vanadium dioxide phases. *Phys Rev B* **2017**, *95* (12), 125105.
11. Morin, F. J., Oxides Which Show a Metal-to-Insulator Transition at the Neel Temperature. *Phys. Rev. Lett.* **1959**, *3* (1), 34-36.
12. D'Haenens, J. P.; Kaplan, D.; Merenda, P., Electron spin resonance in  $V_{1-x}Cr_xO_2$ . *J. Phys. C.* **1975**, *8* (14), 2267-2273.
13. Villeneuve, G.; Drillon, M.; Hagenmulier, P., Contribution a l'etude structurale des phases  $V_{1-x}Cr_xO_2$ . *Mat Res Bull* **1973**, *8*, 1111-1122.
14. Lovorn, T.; Sarker, S. K., Complex Quasi-Two-Dimensional Crystalline Order Embedded in  $VO_2$  and Other Crystals. *Phys Rev Lett* **2017**, *119*, 045501.
15. Osborn, R. NeXpy: A Python GUI to analyze NeXus data. <http://nexpy.github.io/nexpy/>.
16. Jennings, G.; Osborn, R.; Wozniak, J. Crystal Coordinate Transformation Workflow. <https://www1.aps.anl.gov/science/scientific-software/cctw>.
17. Weber, T.; Simonov, A., The three-dimensional pair distribution function analysis of disordered single crystals: basic concepts. *Zeitschrift für Kristallographie Crystalline Materials* **2012**, *227* (5), 238-247.
18. Welberry, T. R.; Weber, T., One hundred years of diffuse scattering. *Crystallography Reviews* **2016**, *22* (1), 2-78.
19. Price-Whelan, A. M.; Sipócz, B. M.; Gunther, H. M.; Lim, P. L.; Crawford, S. M.; Conseil, S.; Shupe, D. L.; Craig, M. W.; Dencheva, N.; Ginsburg, A., et al., The Astropy Project: Building an inclusive, open-science project and status of the v2.0 core package. *arXiv* **2018**, 1801.02634.
20. Robitaille, T. P.; Tollerud, E. J.; Greenfield, P.; Droettboom, M.; Bray, E.; Aldcroft, T.; Davis, M.; Ginsburg, A.; Price-Whelan, A. M.; Kerzendorf, W. E., et al., Astropy: A community Python package for astronomy. *A&A* **2013**, *558*, A33.

21. Proffen, T.; Neder, R. B., DISCUS: a program for diffuse scattering and defect-structure simulation. *J. Appl. Cryst.* **1997**, *30*, 171-175.
22. Paddison, J., Ultrafast calculation of diffuse scattering from atomistic models. *Acta Crystallographica Section A* **2019**, *75* (1), 14-24.
23. Paddison, J. A. M., Ultrafast calculation of diffuse scattering from atomistic models. *Acta Crystallogr. A.* **2019**, *75*, 14-24.
24. Simonov, A.; Weber, T.; Steurer, W., Yell: a computer program for diffuse scattering analysis via three-dimensional delta pair distribution function refinement. *J. Appl. Cryst.* **2014**, *47*, 1146-1152.

## CHAPTER 4: A CRYSTALLOGRAPHIC APPROACH TO THE SHORT-RANGE ORDERING PROBLEM IN $V_{1-x}Mo_xO_2$ ( $0.50 \leq x \leq 0.60$ )

Chapter is being prepared for publication.

### 4.1 Introduction

The tetragonal rutile crystal structure contains infinite chains of edge-sharing metal-oxide octahedra. When the metal atoms have an open-shell, they can form metal-metal bonds along the chains. The resulting dimers necessarily break symmetry, though a few different kinds of ground states have been observed.<sup>1</sup> The two most common examples which we have talked about previously are both monoclinic and are colloquially known as the M1 phase and the M2 phase.

Taken alone, the structural instability may seem rather straightforward, but attempts to suppress or enhance it reveal hidden complexity. Substitution of atoms such as niobium, molybdenum, and tungsten lead to a systematic suppression in the transition temperature while substitution of other atoms such as chromium, aluminum, and gallium lead to an increase in it.<sup>2-7</sup> In the studies of these various metal substituents, new structural phases have been discovered, such as the M2 phase which was discovered in chromium substituted samples and has also been seen in aluminum substituted samples, titanium substituted samples, and in strained  $VO_2$  thin films, to name a few.<sup>4, 8-10</sup> However, some of these phases are not well defined, and the phase diagrams are frequently redrawn, with regions of uncertain provenance. In particular, the phase diagram for  $V_{1-x}Cr_xO_2$ —perhaps the most studied  $VO_2$  metal substituted system—has been published multiple times including orthorhombic phases, other monoclinic phases, and a triclinic phase. However, these phases and their phase boundaries are not consistent across published phase diagrams, nor are their structures well-accepted.<sup>8, 11-15</sup> Additionally, it was only recently

that the (Ti,V)O<sub>2</sub> phase diagram was shown to actually undergo spinodal decomposition.<sup>16</sup> These challenges all stem from the difficulty in determining the correct structure for these substituted VO<sub>2</sub> compounds, with the phase diagrams of other, lesser studied substituents remaining even less certain, such as niobium, molybdenum, and tungsten.

Previous TEM measurements found evidence of supercell reflections in electron diffraction patterns of V<sub>1-x</sub>Mo<sub>x</sub>O<sub>2</sub> around  $x = 0.50$ .<sup>3</sup> These reflections are consistent with either the M1 or M2 superstructures, but with a domain on the order of 10 nm, and the peaks were not present in the synchrotron PXRD patterns. Earlier work by Marinder in 1975, by contrast, presented evidence of two variants of the M1 phase called M1', and M1'' existing from  $0.70 \leq x \leq 0.85$  and then the existence of the M2 phase below  $x = 0.70$ .<sup>3, 17</sup> The researchers found that between  $0.50 < x < 0.70$ , the ordering is difficult to reproduce and characterize.

This study aims to clear up these inconsistencies with detailed observations about the local and long-range structure for this  $0.45 \leq x \leq 0.60$  compositional regime of V<sub>1-x</sub>Mo<sub>x</sub>O<sub>2</sub>, using a combination of laboratory SXR, synchrotron SXR total-scattering/3D- $\Delta$ PDF, and synchrotron PXRD. Single crystals are needed for this structural investigation because short-range structural correlations lead to very broad line-shapes and diffuse scattering features which may not be directly observable in powder diffraction. While some information can be recovered using the pair distribution function (PDF) on total scattering data, a lot of information is lost, as is shown in more detail below.

## 4.2 Experimental

Crystal structures were characterized using two in-house single-crystal diffractometers. The first was a Siemens diffractometer equipped with a Bruker APEX-II CCD and a monochromated Mo-K $\alpha$  producing sealed source that was decommissioned during the study. The

second was a Rigaku XtaLAB Synergy R, DW system, equipped with HyPix detector. Structural models of the single crystal diffraction data were created and refined using SHELX and WINGX.<sup>18-19</sup>

The total scattering data was collected at the Advanced Photon Source (APS) at Argonne National Lab (ANL) on sector 6-ID-D. The experiment used an incident beam energy of 87 keV. The detector was a Dectris Pilatus CdTe 2M detector, held at a distance of 650 mm, with a threshold detection limit set to 43 keV. Samples were mounted on Kapton capillaries using either GE varnish or Duco cement. Goniometer geometry allowed free rotation of  $\phi$ , limited  $\omega$ , and fixed  $\chi$  at  $90^\circ$ . Every temperature scan had three  $360^\circ$   $\phi$  scans, at  $\omega = 0, -15, +15$ . The second and third sub-scans also included a shift of the detector of 5 mm x 5 mm and 10 x 10 mm. The detector and  $\omega$  shifts were to correct for gaps in the detector and blooming artefacts. The data were processed using NeXpy, and transformed using the crystal coordinate transformation work-flow (CCTW).<sup>20-21</sup> Sample temperature was controlled using an Oxford Cryosystems nHelix.

Room temperature synchrotron PXRD data was collected at the APS using 11-BM on crystals with composition  $x = 0.27, 0.34, 0.50, 0.56, 0.59$ . The PXRD scans were analyzed using GSAS and EXPGUI to fit the data.<sup>22-23</sup>

### 4.3 Results and Discussion

Three diffraction methods were required to characterize the structure adequately. 1) Mo-source single crystal diffraction provided initial screening of the crystals, which is how the broad peaks indicative of short-range ordering were first identified. Subsequently, the same method was used to build the crystallographic models that are the primary result of this study. 2) Synchrotron total X-ray scattering measurements (ANL beamline 6-ID-D) on single crystals

were used to more fully map the reciprocal space around each reflection. This data was also used to construct 3D-PDF and 3D- $\Delta$ PDF maps, which provide high levels of detail about the local structure. 3) Standard synchrotron powder X-ray diffraction (ANL beamline 11-BM) was used to analyze the line-shape of the Bragg reflections assigned to the standard rutile structure, which gives information about the unit cell that was obscured in the single crystals.

### 4.3.1 Total Scattering Measurements

While hints of broken rutile symmetry have been reported before in the  $0.45 \leq x \leq 0.60$  regime of  $V_{1-x}Mo_xO_2$ , the first direct observation of the requisite diffuse scattering is shown in Figure 4.1 a-b. Cuts of the  $(hk\frac{1}{2})$  planes (Figure 4.1 a) show planes of diffraction indicating the existence of a supercell structure in this compositional region. However, the peaks are extremely broad, with cross-shaped shoulders that extend far into reciprocal space, confirming that the ordering is not long-range.

Using the high-intensity and resolution of 6-ID-D, the complex Q-dependence of the supercell reflections is apparent. (Figure 4.1 c-e). 53.3(13) % Mo undergoes a phase transition between 200K and 293 K. At high temperature it shows very weak diffuse scattering, while at low temperature the cross-shaped reflections are clearly visible. Below 200 K this pattern remains constant. At even higher composition, 57(1)% Mo, the cross features spread further out along that axis and into each other, though the majority of the intensity remains at the rational HKL point. The resulting scattering rods are quite similar pattern to the 2D-M2 phase observed at  $x = 0.19$  (Figure 4.1 f), as is the diffuse scattering pattern in high temperature  $x = 0.533$ . These scattering rods are not nearly as sharp or intense as in 2D-M2, and they do not appear to have the periodic curvature caused by ferroelectric correlations along the  $\langle 100 \rangle$  rutile directions.

The diffuse peaks have Lorentzian line shapes, which were used to estimate the correlation length,  $\xi$ , of the atomic displacement correlations. For  $x = 0.53$ , the peaks are relatively isotropic and the  $\xi = 25$  and  $17 \text{ \AA}$  along the narrowest and widest cross-sections, respectively. By  $x = 0.57$ ,  $\xi = 11$  and  $5 \text{ \AA}$  for the same axes. Compared to the 2D-M2, which has a  $\xi > 50 \text{ \AA}$  all along the 2D planes, and  $\xi < 1 \text{ nm}$  along the other. Thus, the anisotropy is much lower here, indicating that in this higher composition region the correlations are becoming more three-dimensional, but also weaker. The observed diffuse peaks correspond to a local structure deviation from the average rutile structure, rather than a new long range ordered phase. The close similarity to the scattering in the 2D-M2 phase suggests that the same local correlations are at play, even if the net result differs. In this case, though the relatively large intensity and localization around integer points affords a rare opportunity to apply standard crystallographic tools to this system as a disordered supercell. Appropriate care must be taken in doing so, due to multiple complicating factors. The bulk crystal necessarily contains many coherent domains which must be treated the same as intrinsic twinning due to the nature of the broken symmetry. Unlike true crystal twins, the number of independent diffracting domain orientations depends on how the chosen lattice symmetry maps onto rutile's tetragonal symmetry. Another complication is that regardless of the local symmetry, the long-range symmetry will always appear metrically tetragonal. This also adds in additional problems with the absorption correction.

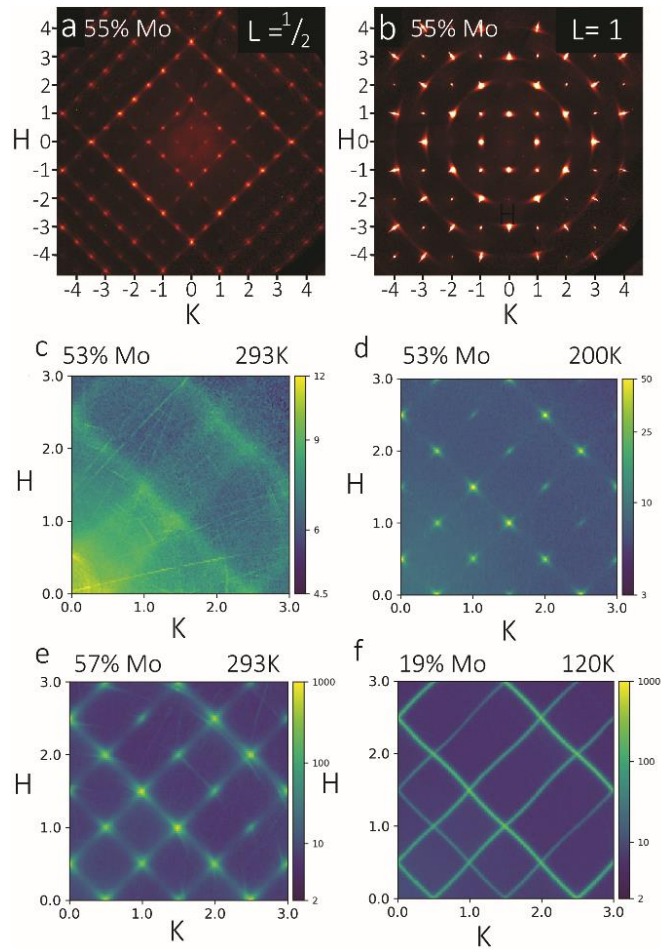


**Figure 4.1** Cuts of the (a)  $hk\frac{1}{2}$  and the (b)  $hk1$  planes in  $V_{1-x}\text{Mo}_x\text{O}_2$  using the rutile lattice vectors. The presence of diffraction peaks in the (a)  $hk\frac{1}{2}$  plane should not exist without a break in the  $P4_2/mnm$  symmetry, but the peaks are considerably broader than usual Bragg peaks. (c-f) Total scattering data from beamline 6-ID-D at the APS. The scattering slices are all taken at  $L = 3/2$ . The 19% Mo data is shown to illustrate the 2D-M2 phase's scattering. All plots are in log scale.

### 4.3.2 Structural Solutions

Standard laboratory SXRD (Phillips and/or Rigaku) was used to index the diffuse peaks and integrate them using a unit cell and space group deemed appropriate based on the diffuse reflections found at the R point in k-space ( $\frac{1}{2}, 0, \frac{1}{2}$ ) and/or  $(0, \frac{1}{2}, \frac{1}{2})$ . For the parent space group,  $P4_2/mnm$ , this leads to its irreducible representation (irrep) choice  $R_1^-$  as a starting point. The atomic displacements in this irrep are caused by the activation of the B1u, B2u, and B3u displacement modes for the metal atom sites as well as the activation of the A1, B1, and B2

displacement modes for the oxygen atom sites. These oxygen displacements are directly correlated to the metal atom displacements. The distortions caused by each displacement mode can be described using a set of four values which each represent a different translational periodicity of the distortion, (a,b,c,d) giving up to four directional degrees of freedom. The distortion of the  $P4_2/mnm$  space group can then be attributed to one of nine possible subgroups depending on the number of those directional degrees of freedom needed to describe that distortion. (Table 4.1). Note that two of the nine options,  $C2/m$  (P1) and  $P2_1/c$  (P4), are the M2 and M1 phases, respectively. The two naming conventions will be used interchangeably. The initial structure solutions for the supercell was limited to these nine choices, with the goal of determining which option gives the model that gave the best fit while remaining consistent with the total X-ray scattering data (6-ID-D). As mentioned above, the apparent crystal system cannot be used to determine the space group in this case, due to the difference between local and long-range metric symmetry.

It is helpful to explain the connection between the nine space group choices. First, note that the designation codes of each subgroup choice have no special meaning, they are just used as unique identifiers that organize the set into subsets. The four  $P_n$  ( $n = 1,3,4,5$ ) are all mutually independent, while the four  $C_n$  ( $n = 1,2,3,8$ ) are each a combination of the modes inherent to two P choices. Thus, the C subset are all subgroups of two of the P ones with both degrees of freedom.  $4D1$  contains all four degrees of freedom from the P subgroups, and thus is the lowest symmetry and a subgroup of the other 8 choices. All 9 choices represent extremely similar local displacements of atoms, with the differences only being represented by how the displacements translate between unit cells in the parent. Since the displacements become disordered on the nanoscale, it is expected that some subgroup choices may give very similar results.

**Table 4.1** Refinement results for the R phase and all nine possible subgroups

<i>Space Group</i> (subgroup symbols)	<i>P42/mnm</i>	<i>C2/m</i> (P1)	<i>Fmmm</i> (P3)	<i>P21/c</i> (P4)	<i>I41/a</i> (P5)
<b>transformation matrix</b>	$\begin{bmatrix} 100 \\ 010 \\ 001 \end{bmatrix} \begin{bmatrix} 0 \\ 0 \\ 0 \end{bmatrix}$	$\begin{bmatrix} 200 \\ 002 \\ 0\bar{1}0 \end{bmatrix} \begin{bmatrix} 0 \\ 0 \\ 0.5 \end{bmatrix}$	$\begin{bmatrix} 220 \\ \bar{2}20 \\ 002 \end{bmatrix} \begin{bmatrix} 0 \\ 0 \\ 0.5 \end{bmatrix}$	$\begin{bmatrix} 10\bar{1} \\ 0\bar{1}0 \\ \bar{1}0\bar{1} \end{bmatrix} \begin{bmatrix} 0.5 \\ 0 \\ 0 \end{bmatrix}$	$\begin{bmatrix} 200 \\ 020 \\ 002 \end{bmatrix} \begin{bmatrix} 0 \\ 1 \\ 0.5 \end{bmatrix}$
<b>displacement directions</b>	(0,0,0,0)	(0,0,a,-a)	(a,-a,-a,a)	(0,0,a,0)	(a,a,a,-a)
<b>Volume per lattice point (Å<sup>3</sup>)</b>	62.680	125.74	252.47	126.50	252.46
<b>R<sub>int</sub></b>	0.0491	0.0791	0.0926	0.0531	0.0967
<b>R<sub>σ</sub></b>	0.0087	0.0202	0.0175	0.0149	0.0181
<b>R<sub>1</sub> (all reflections)</b>	0.0371	0.083	0.0668	0.0614	0.0921
<b>R<sub>1</sub> [F<sub>o</sub> &gt; 4σ(F<sub>o</sub>)]</b>	0.037	0.0821	0.0631	0.061	0.0908
<b>wR0<sub>2</sub></b>	0.1028	0.1891	0.2038	0.1947	0.2848
<b>GooF</b>	1.187	1.202	1.302	1.142	1.3
<b># of refined parameters</b>	11	40	45	31	31
<i>Space Group</i> (subgroup symbols)	<i>C2/m</i> (C1)	<i>P-1</i> (C2)	<i>C2/c</i> (C3)	<i>C2/m</i> (C8)	<i>P-1</i> (4D1)
<b>transformation matrix</b>	$\begin{bmatrix} \bar{2}20 \\ 002 \\ 200 \end{bmatrix} \begin{bmatrix} 0 \\ 0 \\ 0.5 \end{bmatrix}$	$\begin{bmatrix} 010 \\ 101 \\ 10\bar{1} \end{bmatrix} \begin{bmatrix} 0 \\ 0 \\ 0.5 \end{bmatrix}$	$\begin{bmatrix} \bar{2}20 \\ 002 \\ 200 \end{bmatrix} \begin{bmatrix} 0.5 \\ 0.5 \\ 0 \end{bmatrix}$	$\begin{bmatrix} 00\bar{2} \\ \bar{2}20 \\ \bar{1}11 \end{bmatrix} \begin{bmatrix} 0 \\ 0 \\ 0.5 \end{bmatrix}$	$\begin{bmatrix} 002 \\ \bar{1}11 \\ \bar{1}\bar{1}1 \end{bmatrix} \begin{bmatrix} 0 \\ 0 \\ 0.5 \end{bmatrix}$
<b>displacement directions</b>	(a,-a,b,-b)	(0,0,a,b)	(a,a,b,-b)	(a,b,b,a)	(a,b,c,d)
<b>Volume per lattice point (Å<sup>3</sup>)</b>	254.8	125.92	252.8	252.45	252.45
<b>R<sub>int</sub></b>	0.0879	0.0357	0.0927	0.1062	0.0568
<b>R<sub>σ</sub></b>	0.0235	0.0138	0.0237	0.0269	0.0216
<b>R<sub>1</sub> (all reflections)</b>	0.0881	0.06	0.1073	0.1082	0.0941
<b>R<sub>1</sub> [F<sub>o</sub> &gt; 4σ(F<sub>o</sub>)]</b>	0.0841	0.0588	0.1028	0.1019	0.0884
<b>wR0<sub>2</sub></b>	0.2264	0.2061	0.2798	0.239	0.3191
<b>GooF</b>	1.254	1.123	1.279	1.18	1.299
<b># of refined parameters</b>	71	59	59	69	115

Structural solutions of all the options were attempted on the same data set taken from a 55% Mo sample using a brute force approach. The fit statistics from each model are shown in Table 4.1. The rutile model is used as the crystallographically averaged one; it ignores the

diffuse peaks at the R points, and so acceptable statistics are achieved despite the effect that disorder plays. For the subgroup models, the  $R_{\text{int}}$  and  $R_{\sigma}$  generally correlate with the metric symmetry of the model. This is to be expected but does not necessarily reflect a real improvement in the model. Additionally, it should be noted that while  $R_1$  and  $wR_2$  are the standard for validation of the success of a structural fit, the software creating the model is making assumptions based on long-range ordering of the structure when obtaining these statistics. These assumptions fail when considering the short-range ordering of the supercell making the success of models with similar values for  $R_1$  and  $wR_2$  impossible to compare without utilizing other methods of comparison. This issue with basing a comparison solely on the  $R_1$  and  $wR_2$  is highlighted by the values for these statistics in the *P-1* (4D1) structure solution which, as the subgroup of all the possible solutions, should have the best values. However, because of the nature of the short-range ordering in the crystal, solution with fewer refined parameters allows for the short-range distortions to be averaged out in the long-range structure. Because of this, basic comparison of the statistics from the structural solutions cannot be used alone to determine the structure of this short-range ordered phase and other comparison methods must also be utilized. Starting with the highest symmetry ( $Pn$ ) models, *I4<sub>1</sub>/a* (P5) can be dismissed as significantly worse based on the  $R_1$  and  $wR_2$  values. This structural model is tied with *P2<sub>1</sub>/c* (P4) for the fewest refined parameters and still has significantly higher statistics. Of *C2/m* (P1), *Fmmm* (P3), *P2<sub>1</sub>/c* (P4), all are quite similar, with P3 and P4 being slightly better. However, the monoclinic P1 and P4 (the M2 and M1 phases) both benefit from a lower  $R_{\text{int}}$  value, thanks to the model using a lower point group in data reduction and absorption correction. In this context, *Fmmm* may represent a slightly better fit to the data, as it is able to produce a final R value comparable to the others without assuming lower symmetry in the absorption correction.‡

Schematics of the metal atom displacements are shown for these e models in Figure 4.2 b-d. The three models all show different atomic displacement patterns, but none of the show any evidence of significant occupancy ordering.

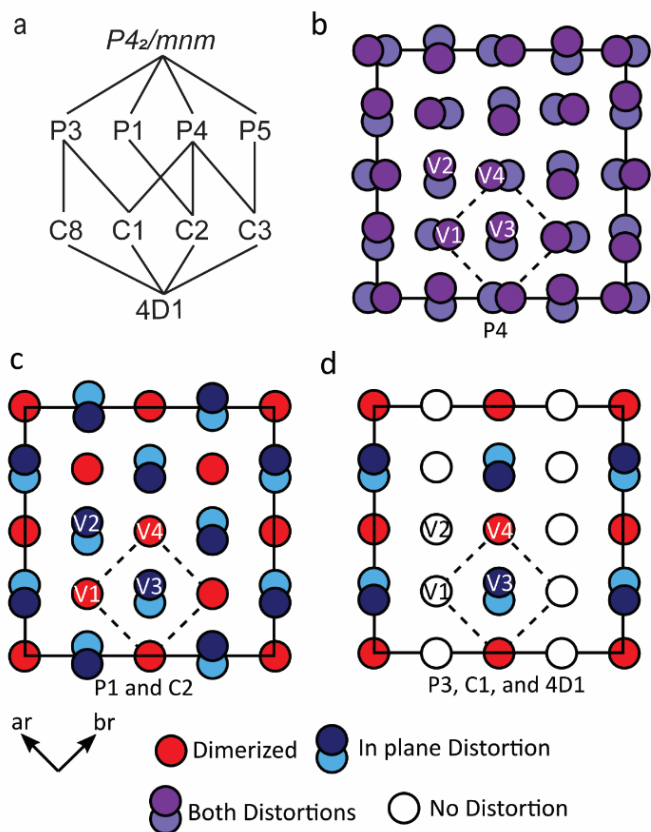


**Figure 4.2** (a) Group-subgroup relations of selected models. (b-d) Schematics highlighting the results of the selected structure solutions. (b)  $P4$  is the M1 phase, (c)  $P1$ , which is the M2 phase, and  $C2$  have nearly identical models, suggesting M1 is incorrect. (d)  $P3$  and  $C1$  are nearly identical, and  $4D1$  agrees qualitatively with them as well. In  $4D1$ , one of the “no distortion” sites has a small  $B2u$  distortion.

Moving on to the  $C_n$  set, they must be compared against their supergroups.  $P-1$  ( $C2$ ) contains a degree of freedom for each of the known M1 and M2 cells ( $P4$  and  $P1$ ), and shows overall the best statistics on the table at first glance. Comparing these three structures, the  $C2$  model is found to agree most closely to the M2 structure compared to the M1 structure (Figure 4.2 c) meaning that when given more degrees of freedom, the M2 model provides the better solution of these two. Dismissing M1 leaves the M2 and  $Fmmm$  models. A similar comparison of

these models can be achieved using another structure possibility,  $C2/m$  (C1), of which both the  $C2/m$  (P1) and  $Fmmm$  (P3) models are substructures. This comparison (Figure 4.2 d) shows that the C1 model barely differs from  $Fmmm$  model.  $Fmmm$  provides the best structural solution of the structural models with only one degree of freedom out of the four irrep modes. A further comparison can be done with the  $P-1$  (4D1) model option of which all eight other options are substructures since the 4D1 model option allows the magnitude for each distortion direction to be different. While this structure does show slight additional distortions compared to that allowed by the  $Fmmm$  structure (Table 4.2), these differences are very small. This provides further evidence that the  $Fmmm$  model is the best description for this short range ordered phase.

Switching from a cartesian coordinate system to an irrep one clarifies what kind of degrees of freedom are necessary.<sup>24</sup> Table 4.2 compares the magnitude of each mode for the M1, M2,  $Fmmm$ , C1, C2, and 4D1 structural models (Table 4.3). This comparison sees a trend in which the magnitude of the B1u and the B2u modes increase going from M1 to M2 to  $Fmmm$ . The larger magnitudes of these modes result in shorter dimers and more drastic in-plane, non-dimerizing distortions in the  $Fmmm$  solution compared to both the M1 and M2 models (Table 4.2). The maximized distortions in the  $Fmmm$  model are relevant because each distortion can only occur at  $1/4$  of the metal atom sites while  $1/2$  of the metal atom sites stay undistorted. On the other hand, in the M2 phase, every metal atom position undergoes a distortion with  $1/2$  forming dimer pairs and  $1/2$  forming in-plane, non-dimerizing distortions, and in the M1 phase every metal atom undergoes both dimerization and in-plane, non-dimerizing distortions. With this in mind, it seems that the weaker distortions contained in the M1 and M2 models are likely a result of an artificial averaging between a strongly distorted chain and a weakly or undistorted chain of metal atoms. Again, this suggests that the  $Fmmm$  model best matches the local structure.

Further evidence of this comes from comparing the *Fmmm* structure solution to lower symmetry ones. The intermediate *C1* phase is exactly equal to the *Fmmm* when the mode magnitudes are  $a = -b$ . This is very close to what was found (Table 4.3). In the lowest symmetry, *4D1* structure solution, every atom is allowed to undergo distortions by the 4 individual degrees of freedom. The structural refinement results in a structure nearly identical to the *Fmmm* phase

**Table 4.2** The difference between the long and short distances between the 4 metal atom sites as well as the angle of metal atom chains.

	<i>R</i>	<i>M1</i>	<i>M2</i>	<i>C2</i>	<i>Fmmm</i>	<i>C1</i>	<i>4D1</i>
$\Delta V1$	0	0.189(1)	0.263(1)	0.2511(11)	0	0.008(2)	0.023(4)
$\Delta V2$	0	0.189(1)	0	0.0372(11)	0	0	0.105(6)
$\Delta V3$	0	0.189(1)	0	0.0372(11)	0	0	0.183(6)
$\Delta V4$	0	0.189(1)	0.263(1)	0.2511(11)	0.477(3)	0.457(2)	0.432(4)
$\angle V1$	180	177.92(5)	180	179.52(5)	180	180	177.94(9)
$\angle V2$	180	177.92(5)	176.87(7)	177.14(5)	178.75(8)	178.60(6)	178.53(4)
$\angle V3$	180	177.92(5)	176.87(7)	177.14(5)	174.24(7)	173.75(9)	174.37(6)
$\angle V4$	180	177.92(5)	180	179.52(5)	180	180	178.66(9)

with  $\frac{1}{4}$  of the metal atom chains undergoing strong dimerization,  $\frac{1}{4}$  of the chains undergoing strong in-plane, non-dimerizing distortions, and only weak dimerization and in-plane, non-dimerizing distortions in the chains where those distortions are not allowed by the *Fmmm* structure. The crystal structure results for the *Fmmm* structure are given in detail in Table 4.4.

Finally, we note that the alternating planes of distorted and non-distorted atoms matches the local structure of the 2D-M2. In that case, there were no short-range correlations between planes and odd number of unit cells apart. This unusual observation was predicted by the geometric frustration model of Lovorn and Sarker.<sup>25</sup> This does not necessarily mean that every other plane is undistorted, only that there are no strong correlations between neighboring planes, and so they average out over multiple unit cells. Thus, it is not clear which way the *Fmmm* model should be interpreted.

**Table 4.3** Values for the displacement modes for the P4, P1, C2, P3, C1, and 4D1 models. In the setting used here, B1u is the dimerizing metal displacement, B2u is the in-plane distortion coupled to the dimerization, and B3u is the in-plane distortion orthogonal to B2u.

<b>Metal Displacement Mode</b>	<b><math>P2_1/c</math> (P4)</b>	<b><math>C2/m</math> (P1)</b>	<b><math>P\bar{1}</math> (C2)</b>	<b><math>Fmmm</math> (P3)</b>	<b><math>C2/m</math> (C1)</b>	<b><math>P\bar{1}</math> (4D1)</b>
<b>B<sub>1u</sub> (a)</b>	-0.09922	-0.09685	0.07472	0.16657	-0.11704	-0.06919
<b>B<sub>1u</sub> (b)</b>	-	-	0.05508	-	0.1126	0.09632
<b>B<sub>1u</sub> (c)</b>	-	-	-	-	-	-0.01377
<b>B<sub>1u</sub> (d)</b>	-	-	-	-	-	0.12945
<b>B<sub>2u</sub> (a)</b>	0.05455	0.05622	0.04237	-0.11244	0.0809	0.04711
<b>B<sub>2u</sub> (b)</b>	-	-	-0.03043	-	-0.07864	-0.06138
<b>B<sub>2u</sub> (c)</b>	-	-	-	-	-	0.01445
<b>B<sub>2u</sub> (d)</b>	-	-	-	-	-	-0.07846
<b>B<sub>3u</sub> (a)</b>	-0.0138	-0.00929	-0.00853	0.0199	-0.01905	-0.01145
<b>B<sub>3u</sub> (b)</b>	-	-	0.00826	-	0.01852	0.01577
<b>B<sub>3u</sub> (c)</b>	-	-	-	-	-	-0.00328
<b>B<sub>3u</sub> (d)</b>	-	-	-	-	-	0.02149

### 4.3.3 Powder Diffraction

The single crystal model only refines atomic positions against a list of measured  $F^2$ , meaning that it doesn't contain any information about the unit cell that was not determined from the integration step. However, if the local structure is orthorhombic  $Fmmm$ , then the metric symmetry must be lowered from tetragonal on the same scale, in this case by making  $\gamma \neq 90^\circ$  in the parent cell. Unfortunately, the long-range symmetry is tetragonal, so that is the apparent symmetry of the model, regardless of the actual local structure. The  $Fmmm$  model's apparent a and b lattice parameters are essentially equal. As an alternate probe, powder diffraction can be extremely sensitive to small changes in lattice parameters, and it is insensitive to crystallite orientation. Additionally, utilizing anisotropic broadening of peaks within the Rietveld method allows an accurate correlation between peak shape and local strain, or in other words, deviation from tetragonality.

**Table 4.4** Structural refinement parameters for the structural solution of  $V_{0.45}Mo_{0.55}O_2$  in the space group  $Fmmm$ .

<b>a</b> (Å)	13.3365(9)
<b>b</b> (Å)	13.3352(10)
<b>c</b> (Å)	5.6785(3)
<b>α</b> (°)	90
<b>β</b> (°)	90
<b>γ</b> (°)	90
<b>V</b> (Å <sup>3</sup> )	1009.89(12)
<b>Z</b>	32
<b>temperature</b> (K)	293(2)
<b>crystal description</b>	plate
<b>crystal color</b>	metallic-bluish-black
<b>crystal size max</b> (mm)	0.16
<b>crystal size mid</b> (mm)	0.12
<b>crystal size min</b> (mm)	0.05
<b>scan mode</b>	ω
<b>absorption coefficient</b> <b>μ</b> (mm <sup>-1</sup> )	8.577
<b>absorption correction</b>	numerical
<b>A<sub>min</sub></b>	0.7247
<b>A<sub>max</sub></b>	1.327
<b>radiation wavelength</b> (Å)	0.71073
<b>radiation type</b>	MoKα
<b>F000</b>	1584
<b>Reflections</b>	1186
<b>R<sub>int</sub></b>	0.0926
<b>R<sub>σ</sub></b>	0.0175
<b>R<sub>1</sub> (all reflections)</b>	0.0668
<b>R<sub>1</sub> [F<sub>o</sub> &gt; 4σ(F<sub>o</sub>)]</b>	0.0631
<b>wR0<sub>2</sub></b>	0.2038
<b>GooF</b>	1.302
<b># of refined parameters</b>	45

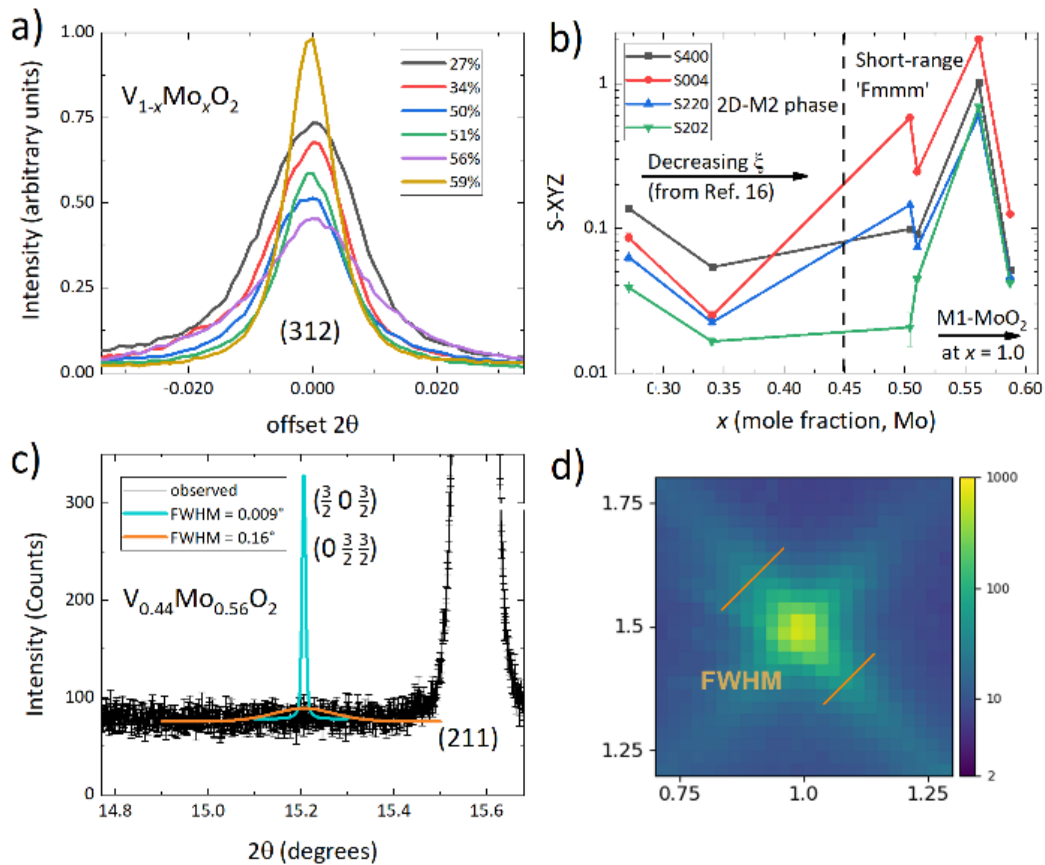


**Figure 4.3** PXRD data on  $V_{1-x}Mo_xO_2$  from 11-BM. (a) Comparison of peak shape between compositions. Peaks are both normalized and offset in  $2\theta$  for comparison. (b) Anisotropic peak broadening and strain analysis as a function of composition from Rietveld refinement using a rutile model (c) Comparison between expected supercell reflection  $(\frac{3}{2} 0 \frac{3}{2})$  and observation in  $V_{0.44}Mo_{0.56}O_2$  for two different linewidths. The intensity is equivalent in both and is taken from the single crystal diffraction integrated intensities. The blue line has the same FWHM as the observed parent phase reflections in this composition (e.g. panel a). The orange line is uses the actual FWHM determined from total scattering (6-ID-D), shown in panel (d).

Synchrotron powder diffraction data (11-BM) were collected in the composition range  $x = 0.20$  to  $0.60$  and  $x = 1.0$  at room temperature. The peak shape of the (312) reflection are shown in Figure 4.3 a. Above  $x = 0.40$ , the peak broadens substantially, with the full width at half maximum (FWHM) maximized at  $x = 0.55$ . Note that this is around where the transition must go above room temperature. The broadening of the rutile peaks is likely directly correlated to the short-range correlations. In order to get a qualitative sense of whether strain is lowering the local

symmetry, the Stephens anisotropic strain broadening terms were refined using the rutile cell as the model, shown in Figure 4.3 b.<sup>26</sup>

Finally, there are no observed peaks in the PXRD pattern that are consistent with the supercell (Figure 4.3 c), as expected. Based on the total scattering data (Figure 4.3 d), the diffuse reflections are about  $0.26^\circ$  FWHM, which is unobservable (Figure 4.3 c, orange line).

Interestingly, even without the super-cell peaks present in the fit, the intensities of the subcell reflections can still be used to fit the same models, with similar results to the SXRD, albeit much less accurate.

#### 4.4 Conclusions

We have shown that  $V_{1-x}Mo_xO_2$  ( $0.50 \leq x \leq 0.60$ ) departs from the symmetry at both higher and lower compositions. The long-range crystal structure is rutile, but that there are strong local correlations that give rise to a phase with a distorted structure that best matches the orthorhombic *Fmmm* space group. The phase cannot be perfectly ordered as evidenced by the cross shaped diffraction peaks observed in total scattering data. The solution of this structural phase helps to increase the understanding of the  $V_{1-x}Mo_xO_2$  phase diagram as well as the  $VO_2$  system in general since the same structural determination used for this phase can be applied to other related substituent phases that have structures which have proven difficult to understand. The model is similar to the planar structure of the 2D-M2 phase at lower compositions and can be seen as the collapse of the 2D-M2 into one that has very short-range ordering equal in all 3 dimensions instead of just one. This seems to be a culmination of the geometric frustration that was the attributed cause of the 2D-M2 ordering.

## References

1. Hiroi, Z., Structural instability of the rutile compounds and its relevance to the metal-insulator transition of VO<sub>2</sub>. *Progr. Solid State Chem.* **2015**, *43*, 47-69.
2. Villeneuve, G.; Bordet, A.; Casalot, A.; Pouget, J. P.; Launois, H.; Lederer, P., Contribution to the Study of the Metal-Insulator Transition in the V<sub>1-x</sub>Nb<sub>x</sub>O<sub>2</sub> System: I-Crystallographic and Transport Properties. *J. Phys. Chem. Solids* **1972**, *33*, 1953-1959.
3. Holman, K. L.; McQueen, T. M.; Williams, A. J.; Klimczuk, T.; Stephens, P. W.; Zandbergen, H. W.; Xu, Q.; Ronning, F.; Cava, R. J., Insulator to Correlated Metal Transition in V<sub>1-x</sub>Mo<sub>x</sub>O<sub>2</sub>. *Phys. Rev. B.* **2009**, *79*, 245114.
4. Pouget, J. P.; Launois, H.; Rice, T. M.; Dernier, P.; Gossard, A.; Villeneu, G.; Hagenmul, P., Dimerization of a linear heisenberg chain in insulating phases of V<sub>1-x</sub>Cr<sub>x</sub>O<sub>2</sub>. *Phys. Rev. B.* **1974**, *10* (5), 1801.
5. Jin, P.; Tanemura, S., Relationship between Transition Temperature and x in V<sub>1-x</sub>W<sub>x</sub>O<sub>2</sub> Films Deposited by Dual-Target Magnetron Sputtering. *Jpn J Appl Phys* **1995**, *34*, 2459-2460.
6. Wu, Y.; Fan, L.; Chen, S.; Chen, S.; Chen, F.; Zou, C.; Wu, Z., A novel route to realize controllable phases in an aluminum (Al<sup>3+</sup>)-doped VO<sub>2</sub> system and the metal-insulator transition modulation. *Mater Lett* **2014**, *127*, 44-47.
7. Kang, L.; Gao, Y.; Zhang, Z.; Du, J.; Cao, C.; Chen, Z.; Luo, H., Effects of annealing parameters on optical properties of thermochromic VO<sub>2</sub> films prepared in aqueous solution. *J Phys Chem C* **2010**, *114*, 1901-1911.
8. Marezio, M.; McWhan, B.; Remeika, J. P.; Dernier, P. D., Structural aspects of metal-insulator transitions in Cr-doped VO<sub>2</sub>. *Phys Rev B* **1972**, *5*, 2541-2551.
9. Ghedira, M.; Vincent, H.; Marezio, M.; Launay, J. C., Structural aspects of metal-insulator transitions in V<sub>0.985</sub>Al<sub>0.015</sub>O<sub>2</sub>. *Solid State Chem* **1977**, *22*, 423-438.
10. Kong, T.; Masters, M. W.; Bud'ko, S. L.; Canfield, P. C., Physical properties of V<sub>1-x</sub>Ti<sub>x</sub>O<sub>2</sub> (0 < x < 0.187) single crystals. *APL Mat.* **2015**, *3* (041502), 041502.

11. Villeneuve, G.; Drillon, M.; Hagenmuller, P., Contribution a l'etude structurale des phases  $V_{1-x}Cr_xO_2$ . *Mat Res Bull* **1973**, *8*, 1111-1122.
12. Hagenmuller, P., Structures and chemical bond problems in vanadium oxides. *NBS Special Publication* **1972**, *364*, 205-218.
13. Villeneuve, G.; Bordet, A.; Casalot, A.; Hagenmuller, P., Proprietes physiques et structurales de la phase  $Cr_xV_{1-x}O_2$ . *Mat Res Bull* **1971**, *6* (2), 119-130.
14. Goodenough, J. B.; Hong, H. Y. P., Structures and a two-band model for the system  $V_{1-x}Cr_xO_2$ . *Phys Rev B* **1973**, *8* (4), 1323-1331.
15. Shao, Z.; Cao, X.; Luo, H.; Jin, P., Recent progress in the phase-transition mechanism and modulation of vanadium dioxide materials. *NPG Asia Materials* **2018**, *10*, 581-605.
16. Hiroi, Z.; Hayamizu, H.; Yoshida, T.; Muraoka, Y.; Okamoto, Y.; Yamaura, J.; Ueda, Y., Spinodal Decomposition in the  $TiO_2$ - $VO_2$  System. *Chem. Mater.* **2013**, *25* (11), 2202-2210.
17. Marinder, B. O., On the Phase Relations in the  $V_xMo_{1-x}O_2$  System ( $0 \leq x \leq 0.55$ ). *Mat. Res. Bull.* **1975**, *10*, 909-914.
18. Sheldrick, G. M., A Short History of SHELX. *Acta. Crystallogr. A.* **2008**, *64* (1), 112-122.
19. Farrugia, L. J., WinGX Suite for Small-Molecule Single-Crystal Crystallography. *J. Appl. Crystallogr.* **1999**, *32* (4), 837-838.
20. Osborn, R. NeXpy: A Python GUI to analyze NeXus data. <http://nexpy.github.io/nexpy/>.
21. Jennings, G.; Osborn, R.; Wozniak, J. Crystal Coordinate Transformation Workflow. <https://www1.aps.anl.gov/science/scientific-software/cctw>.
22. Toby, B. H., ExpGui, a graphical user interface of gsas. *J. Appl. Crystallogr.* **2001**, *34*, 210-213.
23. Larson, A. C.; Dreele, R. B. V., General structure analysis system (gsas). *Los Alamos National Laboratory Report* **2000**, 86-748.

24. Kerman, S.; Campbell, B. J.; Satyavarapu, K. K.; Stokes, H. T.; Perselli, F.; Evans, J. S. O., The superstructure determination of displacive distortions via symmetry-mode analysis. *Acta Cryst.* **2012**, A68, 222-234.
  
25. Lovorn, T.; Sarker, S. K., Complex Quasi-Two-Dimensional Crystalline Order Embedded in VO<sub>2</sub> and Other Crystals. *Phys Rev Lett* **2017**, 119, 045501.
  
26. Stephens, P., Phenomenological Model of Anisotropic Peak Broadening in Powder Diffraction. *J. Appl. Cryst.* **1999**, 32, 281-289.

## CHAPTER 5: FURTHER WORK ON $V_{1-x}M_xO_2$ , $M = Mo, Cr, W$ AND $V_7Nb_6O_{29}$

### 5.1 Introduction

This discovery of the 2D-M2 phase and the solution of the *Fmmm* ordering phase completely redraws the (V,Mo)O<sub>2</sub> phase diagram, and provides new insights into the structural instability in VO<sub>2</sub>. However, there is still much work left to be done on this structural problem, since the data on the compositions between the two phases needs to be visited in greater detail. Additionally, more work is required to fully understand the phase diagram in the Mo rich region of the phase diagram in which Marinder et al. suggested the existed of two new M1 metastable phases, M1' and M1".<sup>1</sup>

Total scattering experiments on VO<sub>2</sub> with other transition metal substituents such as chromium and tungsten, since they are in the same group as molybdenum and niobium since it is in the same group as vanadium would additionally help to tease out more information and set up trends about the inherent structural instability. Chromium substitution leads to the emergence of the M2 phase at low substituent concentrations.<sup>2</sup> There have also been reports of other monoclinic phases, an orthorhombic phase, and a triclinic phase all present in the phase diagram of  $V_{1-x}Cr_xO_2$ , with no consensus on the exact phase lines or even the existence of the phases.<sup>2-5</sup> Tungsten substitution of VO<sub>2</sub> has previously been predicted to result in a systematic change in the local structure.<sup>6</sup> Inclusion of tungsten substitution additionally results in a more drastic suppression of the MIT with the transition temperature dropping by 20K per atomic percent so, determining how the difference in the effect of the substitution on the structural instability should provide better information about the inherent instability. Niobium substitution is an interesting

choice because  $\text{NbO}_2$  has an entirely different parent structure in the  $I4_1/a$  space group. While there is a subgroup of the  $P4_2/mnm$  space group that corresponds to the  $I4_1/a$  space group, it should be noted that these are different structures.<sup>7</sup>

Sometimes in the process of obtaining a compositionally substituted material, a new material with metal-site ordering, rather than the substituted material, can be obtained. Materials such as  $\text{V}_{1-x}\text{Mo}_x\text{O}_2$  have mixed metal sites where both metals exist on the same site in the unit cell with the probability of finding the metal on that site being equal to the relative composition of the two metals. However, other materials such as  $\text{Cr}_2\text{WO}_6$  have ordered metal sites with each metal having at least one unique site in the unit cell.<sup>8</sup> Materials with metal-site ordering have the possibility to have unique properties apart from what would be expected from a material with the same composition but in antiferromagnetic material in part because it contains magnetic chromium atom sites that are sandwiched in between layers of non-magnetic tungsten atom sites.<sup>9</sup> Other properties such as a ferroelectric material can also be obtained with metal-site ordered materials. A ferroelectric is a material in which there is a physical, ferroelectric distortion of an atom site that leads to the material having a non-centrosymmetric space group and have applications as tunable capacitors.<sup>10</sup>

This chapter will discuss incomplete projects that include  $\text{V}_{1-x}\text{M}_x\text{O}_2$ ,  $M = \text{Mo}, \text{Cr},$  and  $\text{W}$ , as well as the structure solution for a new metal-site ordered compound  $\text{V}_7\text{Nb}_6\text{O}_{29}$  that has potential to be a new ferroelectric material.

## 5.2 Further work on $\text{V}_{1-x}\text{Mo}_x\text{O}_2$

Total X-ray scattering experiments have been completed on 11 different compositions of  $\text{V}_{1-x}\text{Mo}_x\text{O}_2$  with compositions between  $0 \leq x \leq 1$ . However, each sample results in several gigabytes of data being collected. Because of the amount of data, the analysis and interpretation

has primarily focused on the most interesting results from the scattering experiments, the  $x = 0.19$  and the  $0.50 \leq x \leq 0.60$  with some information from the  $x = 0.17, 0.27,$  and  $0.33$  being used to support the results from the other compositions. However, there is a lot of data analysis, interpretation, and modeling that is currently being worked on for the additional compositions. With the remaining analysis, the phase diagram between  $0 \leq x \leq 0.60$  can be filled out and more details about the structural instability will be obtain. In this composition range, there is evidence of the 2D-M2 ordering phase existing up to around  $x = 0.40$  shown in Figure 5.1; however, with significantly shorter correlation lengths than in  $x = 0.19$ .

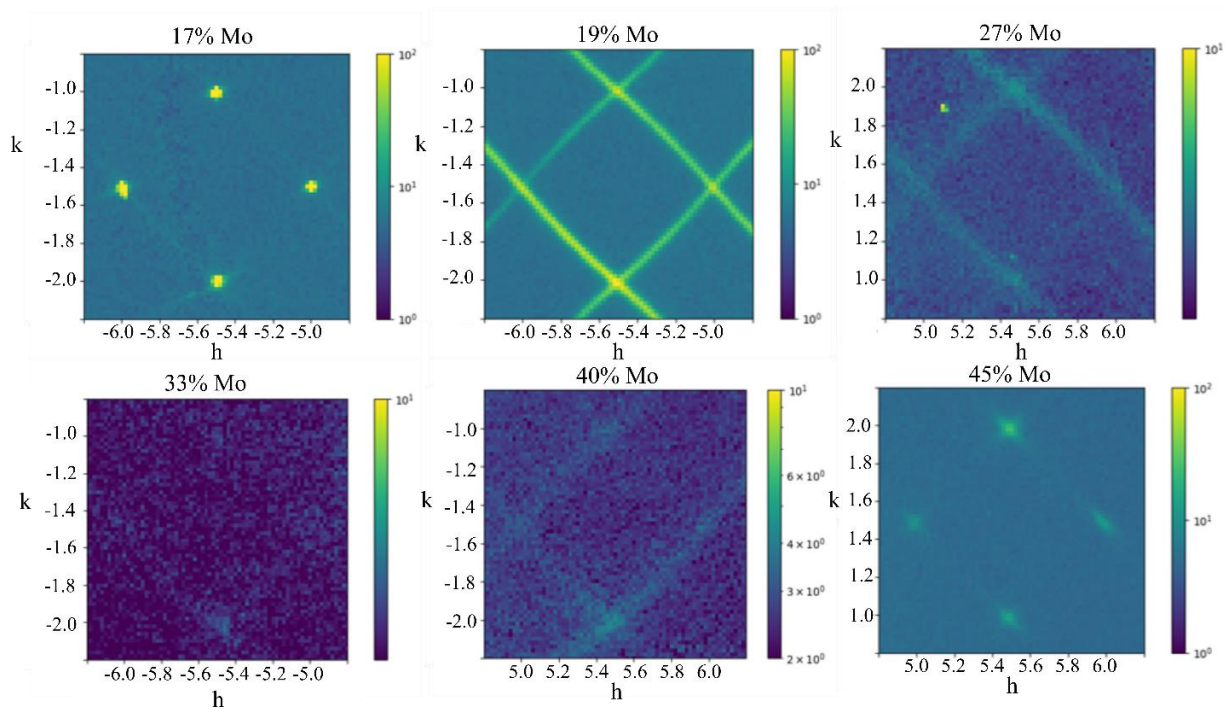


**Figure 5.1** The compositional dependence of the diffuse scattering features in  $V_{1-x}Mo_xO_2$ .

In  $x = 0.19$ , further modeling work on different aspects attributing to the diffuse scattering can give a better idea of how things such as size effects effect the structural instability. With the compositions between  $0.50 \leq x \leq 0.60$ , the diffuse scattering data was mostly used as supporting information for the structural determination done using standard crystallographic

techniques. Further study of the local structure in this compositional range will provide better understanding about the *Fmmm* structural phase and its relationship to the 2D-M2 phase.

Finally, further work can be done to extend the synthetic method to obtain compositions above  $x = 0.60$ . Several attempts at this synthesis have been taken; however, the synthesis has resulted in the formation of  $\text{MoO}_2$ ,  $\text{Mo}_4\text{O}_{11}$ , and other molybdenum and vanadium oxides. It is possible that by using more reducing conditions, then the synthesis can be extended beyond the current  $x = 0.60$  limit. With the synthesis extended to the entire composition range, then the phase line between the *Fmmm* and the  $\text{MoO}_2$  M1 phase can be explored with the determination of the previously observed M1' and M1'' phases in this compositional range.

### 5.3 Synthesis and Total Scattering of Cr, W Substituted $\text{VO}_2$

In addition to the synthesis of single crystals of  $\text{V}_{1-x}\text{Mo}_x\text{O}_2$ , the synthesis of  $\text{V}_{1-x}\text{Cr}_x\text{O}_2$  and  $\text{V}_{1-x}\text{W}_x\text{O}_2$  have also been accomplished using CVT synthesis. The synthesis of these compounds has proven to be less complicated than the synthesis of  $\text{V}_{1-x}\text{Mo}_x\text{O}_2$ , with a CVT synthesis using  $\text{TeCl}_4$  as the transport agent being sufficient for obtaining large single crystals of the substituted compounds. This synthesis uses the same heating scheme in a multi-zone furnace with a dwell time of 6 days, the hot zone set at  $950\text{ }^\circ\text{C}$  (9 hour ramp on heating, 8 hour ramp on cooling), and the cold zone set at  $850\text{ }^\circ\text{C}$  (10 hour ramp on heating, 9 hour ramp on cooling). The synthesis results in large, metallic-grey single crystals, up to  $3\times 3\times 3$  mm in size.

Total X-ray scattering experiments have also been completed on two compositions of  $\text{V}_{1-x}\text{Cr}_x\text{O}_2$  with  $x = 0.03$  and  $0.05$ . Both of these compositions have the M2 cell; however, there is evidence of scattering rods similar to that of  $\text{V}_{0.81}\text{Mo}_{0.19}\text{O}_2$  shown in Figure 5.2, but without the wavy pattern. This data has not been analyzed using 3D- $\Delta$ PDF; however, this would suggest a similar 2D- ordering phase; however, without the geometric frustrations needed in the

$V_{0.81}Mo_{0.19}O_2$  model, likely as a result of the long-range ordering also not having order parameters where  $m_A \neq 0 \neq m_B$ . This likely indicates further structural instability in the  $V_{1-x}Cr_xO_2$  system beyond that which caused the 3D-M2 phase. This instability may result in further structural phases like the previously reported additional monoclinic, orthorhombic and the triclinic phases or, it could result in another structure such as the  $Fmmm$  phase. More work needs to be done to determine how the structural instability evolves as a function of the chromium substitution and the diffuse scattering and the group theoretical approach that we have used on the molybdenum substituted system should prove useful in this further study.

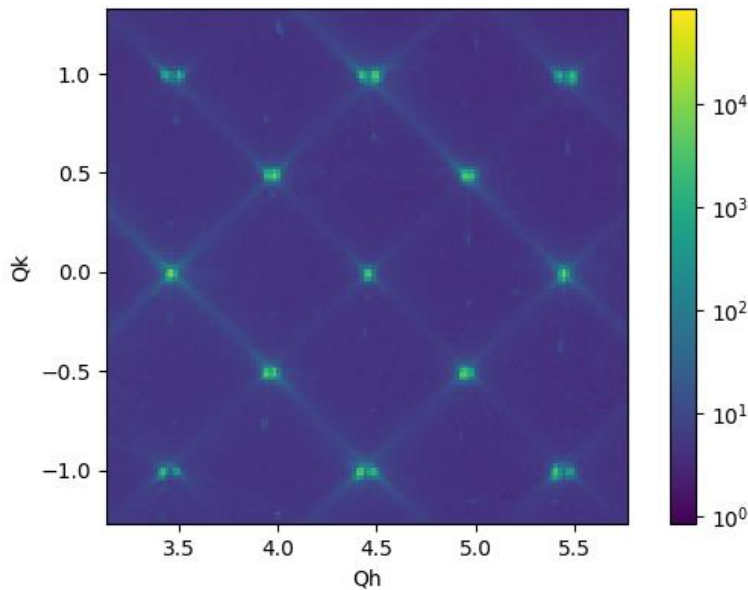


**Figure 5.2** Diffuse scattering feature similar to that caused by the 2D-M2 phase in  $V_{0.81}Mo_{0.19}O_2$ , found in  $V_{0.95}Cr_{0.05}O_2$ .

#### 5.4 New Metal Site Ordering Phase, $V_7Nb_6O_{29}$

When the synthesis of  $V_{1-x}Nb_xO_2$  was first attempted, there was a hardware issue with the multi-zone furnace. So, synthesis of  $V_{0.10}Nb_{0.90}O_2$  was attempted using a single zone tube furnace set to 950°C with a ramp time of 10 hours. The side of the single zone furnace was left open to air to allow a natural heat gradient of 950°C on the hot zone and roughly 850°C on the cold zone. The resulting mixture of products contained a mixture of vanadium and niobium

oxides with an additional unknown material. A crystal of this unknown composition was isolated and used for SXRD experiments. The structure solution, shown in Figure 5.3 with details in Table 5.1 is in the P4 space group which is a non-centrosymmetric space group. The structure has four unique metal sites and a composition of  $V_{6.86}Nb_{6.14}O_{29}$ , with the likely ideal composition being  $V_7Nb_6O_{29}$ . There is metal-site ordering on two sites of these that correspond to vanadium atoms. The other two sites have metal site mixing between vanadium and niobium. They are predominantly niobium with only 11% vanadium on one site and 35% vanadium on the other.

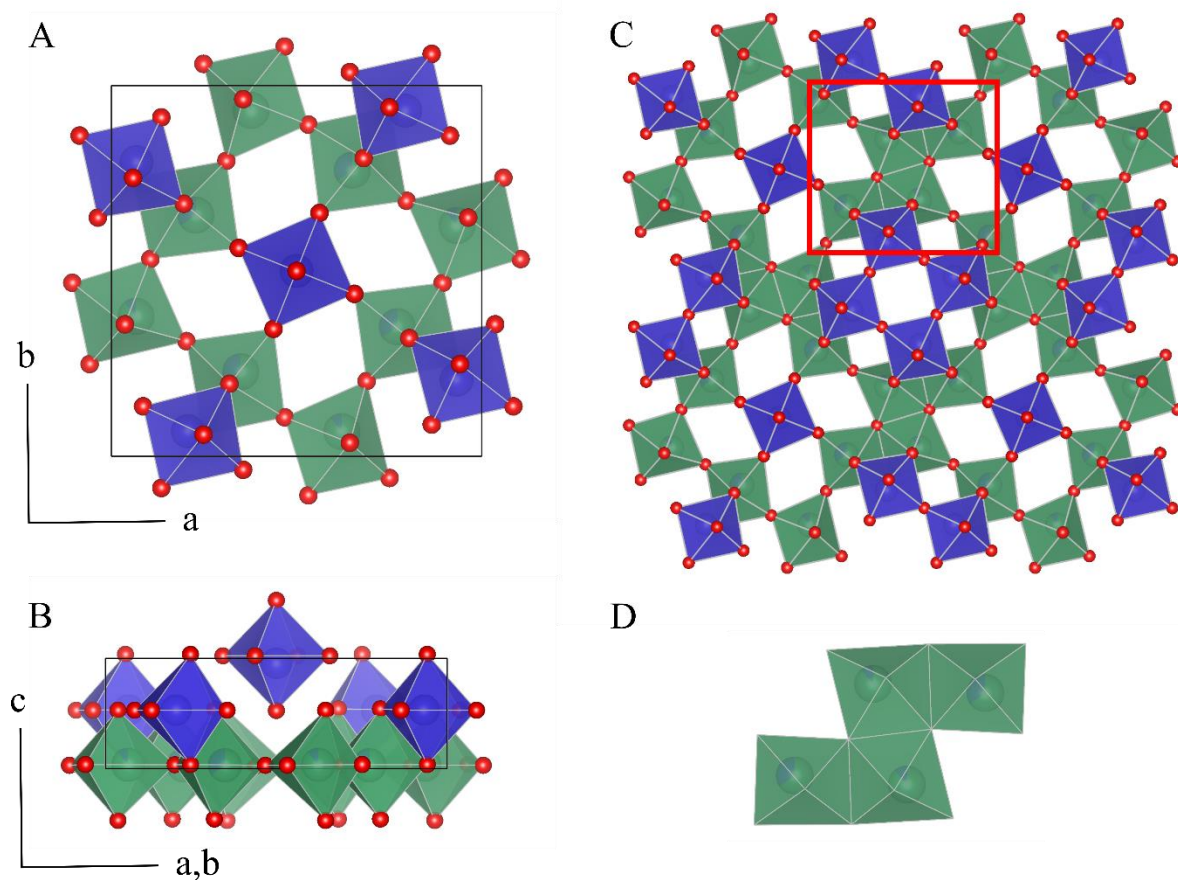


**Figure 5.3** Blue polyhedrons have vanadium at the center and the green polyhedrons have predominantly niobium at the center. A.) View down the c axis. B.) View down the a or b axis, this view shows the ferroelectric distortion in the center of the unit cell. C.) An extended view of the c axis view showing the connectivity between unit cells. The set of four atoms in the red box are isolated in panel D. Based on the partial occupancies of the four atoms forming this set, one will be a vanadium atom and three will be niobium atoms.

This site mixing results in one of the two mixed metal sites having a vanadium roughly 25% of the time with this assumption resulting in the idealized formula of  $V_7Nb_6O_{29}$ . However, if the site was made to be solely niobium, then the idealized formula would become  $V_5Nb_8O_{29}$ . The metal-site ordering in the structure likely comes from a difference in the oxidation of the two metals in the structure. This further supports presumed  $V_7Nb_6O_{29}$  idealized formula as it would mean pure  $V^{4+}$  and  $Nb^{5+}$ , whereas the  $V_5Nb_8O_{29}$  idealized formula would require that some of the metal atoms of the same type have differing oxidation states.

The structure seems to be related to another metal-site ordered oxide of the composition  $VNb_9O_{25}$  which is a lithium storage material shown in Figure 5.4; however, with some of the metal sites being reduced,  $VNb_9O_{25}$  has an average oxidation state of 5+ compared to the average

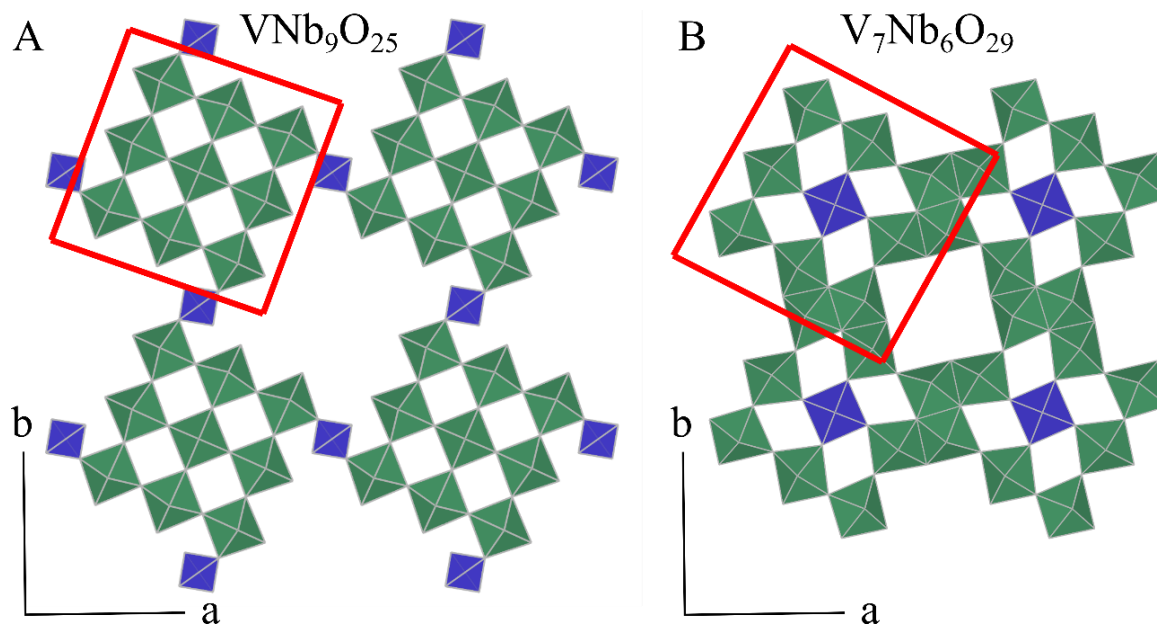


**Figure 5.4** Blue polyhedrons have vanadium at the center and the green polyhedrons have predominantly or entirely niobium at the center. A slice of the  $1\frac{1}{2}1$  plane for  $VNb_9O_{25}$  in panel A and  $V_7Nb_6O_{29}$  in panel B. Due to the smaller overall oxidation state, the corner sharing interactions between the metal clusters, shown in the red boxes, is replaced with edge sharing interactions.

**Table 5.1** Structure solution data for  $V_7Nb_6O_{29}$ 

<b>Space Group</b>	P4
<b>a (Å)</b>	11.8235(3)
<b>b (Å)</b>	11.8235(3)
<b>c (Å)</b>	3.8071(2)
<b><math>\alpha</math> (°)</b>	90
<b><math>\beta</math> (°)</b>	90
<b><math>\gamma</math> (°)</b>	90
<b>V (Å<sup>3</sup>)</b>	532.21(4)
<b>Z</b>	1
<b>Nb1:V1 ratio</b>	0.89(2) : 0.11(2)
<b>Nb2:V2 ratio</b>	0.65(1) : 0.35(1)
<b>temperature (K)</b>	293(2)
<b>crystal description</b>	rod
<b>crystal colour</b>	black
<b>crystal size max (mm)</b>	0.05
<b>crystal size mid (mm)</b>	0.02
<b>crystal size min (mm)</b>	0.02
<b>radiation wavelength (Å)</b>	0.71073
<b>radiation type</b>	MoK $\alpha$
<b>Reflections</b>	2693
<b>R<sub>int</sub></b>	0.0926
<b>R<sub><math>\sigma</math></sub></b>	0.0175
<b>R<sub>1</sub> (all reflections)</b>	0.0512
<b>R<sub>1</sub> [<math>F_o &gt; 4\sigma(F_o)</math>]</b>	0.0436
<b>wR0<sub>2</sub></b>	0.1661
<b>Goof</b>	1.158
<b># of refined parameters</b>	100

oxidation state of 4.46+ in  $V_7Nb_6O_{29}$ , resulting in an increase in edge sharing interactions.<sup>11</sup>

These edge sharing interactions results in ferroelectric distortions in the material compared to  $VNb_9O_{25}$  with most of the ferroelectric distortions occurring in the ab directions and canceling out. However, one of the vanadium atom sites has a ferroelectric distortion in the c direction which is not canceled out and could indicate that the material has promise as a ferroelectric candidate. Additionally, this change from corner sharing to edge sharing interactions is

reminiscent of the structural changes in the vanadium Magnéli phases.<sup>12</sup> It could be possible that these two compounds may fall into a family of similar compounds with slightly varying oxidation state. The current samples from the first synthesis are not large enough to undergo measurements to test for ferroelectricity; however, if the synthesis is optimized and larger samples can be obtained reliably, then the material will need to undergo physical property measurements.

## 5.5 Conclusions

Synthesis of large single crystals of  $V_{1-x}Mo_xO_2$ ,  $V_{1-x}Cr_xO_2$ , and  $V_{1-x}W_xO_2$  have been completed. Using crystals from this synthesis, total X-ray scattering experiments have been carried out on 11 different composition of  $V_{1-x}Mo_xO_2$  and 2 compositions of  $V_{1-x}Cr_xO_2$  with evidence of a 2D ordered phase in both systems. There is still a significant amount of work that needs to be done on the analysis of the data collected on these substituent systems that is currently being carried out by multiple graduate researchers.

A new metal-site ordered phase  $V_7Nb_6O_{29}$  has also been synthesized and the structure has been solved. The structure is non-centrosymmetric and appears to be a potential ferroelectricity candidate due to a ferroelectric distortion in the c direction. Further work needs to be done to obtain larger single crystals that can be used for physical property measurements.

## References

1. Marinder, B. O., On the Phase Relations in the  $V_xMo_{1-x}O_2$  System ( $0 \leq x \leq 0.55$ ). *Mat. Res. Bull.* **1975**, *10*, 909-914.
2. Villeneuve, G.; Drillon, M.; Hagenmuller, P., Contribution a l'etude structurale des phases  $V_{1-x}Cr_xO_2$ . *Mat Res Bull* **1973**, *8*, 1111-1122.
3. Ladd, L. A.; Paul, W., Optical and transport properties of high quality crystals of  $V_2O_4$  near the metallic transition temperature. *Solid State Commun.* **1969**, *7* (4), 425-428.
4. Villeneuve, G.; Bordet, A.; Casalot, A.; Hagenmuller, P., Proprietes physiques et structurales de la phase  $Cr_xV_{1-x}O_2$ . *Mat Res Bull* **1971**, *6* (2), 119-130.
5. Marezio, M.; McWhan, B.; Remeika, J. P.; Dernier, P. D., Structural aspects of metal-insulator transitions in Cr-doped  $VO_2$ . *Phys Rev B* **1972**, *5*, 2541-2551.
6. Tan, X.; Yao, T.; Long, R.; Sun, Z.; Feng, Y.; Cheng, H.; Yuan, X.; Zhang, W.; Liu, Q.; Wu, C.; Xie, Y.; Wei, S., Unraveling Metal-insulator Transition Mechanism of  $VO_2$  Triggered by Tungsten Doping. *Sci. Rep.* **2012**, *2* (466), 1-6.
7. Villeneuve, G.; Bordet, A.; Casalot, A.; Pouget, J. P.; Launois, H.; Lederer, P., Contribution to the Study of the Metal-Insulator Transition in the  $V_{1-x}Nb_xO_2$  System: I-Crystallographic and Transport Properties. *J. Phys. Chem. Solids* **1972**, *33*, 1953-1959.
8. Bayer, G.,  $Cr_2WO_6$ , a New Trirutile Compound. *J. Am. Ceram. Soc.* **1960**, *43* (9), 495-496.
9. Fang, Y.; Wang, L. Y.; Song, Y. Q.; Tang, T.; Wang, D. H.; Du, Y. W., Manipulation of magnetic field on dielectric constant and electric polarization in  $Cr_2WO_6$ . *Appl Phys Lett* **2014**, *104* (13), 132908.
10. Tagantsev, A. K., Size effects in Ferroelectric-Containing Structures. In *Encyclopedia of Materials: Science and Technology*, Buschow, K. H. J.; Cahn, R. W.; Flemings, M. C.; Ilschner, B.; Kramer, E. J.; Mahajan, S.; Vey, P., Eds. Elsevier: 2011; pp 1-6.

11. Jiang, C.; Liu, T.; Long, N.; Cheng, X.; Peng, N.; Zhang, J.; Zheng, R.; Yu, H.; Shu, J., VNb<sub>9</sub>O<sub>25</sub> nanowires with superior electrochemical property towards lithium ion batteries. *Ceram. Int.* **2019**, *45* (14), 18111-18114.
  
12. Allred, J. M.; Cava, R. J., Crystal structures of the high temperature forms of V<sub>8</sub>O<sub>15</sub> and V<sub>9</sub>O<sub>17</sub> and structural trends in the V<sub>n</sub>O<sub>2n-1</sub> Magnéli series. *J. Solid State Chem.* **2013**, *198*, 10-17.

## CHAPTER 6: CONCLUSIONS

The study of the structures of transition metal oxides is an important task to further our understanding of the interplay between structure and properties. Particularly, the structural instability in  $\text{VO}_2$  is an important feature in the material and the substituted analogs of it. Understanding the structural instability can give us insights into the metal-to-insulator transition, but it also gives us insight into structural phase transitions as a whole. We have used various techniques to explore this structural instability and have discovered new, exciting regions in the  $(\text{V},\text{Mo})\text{O}_2$  phase diagram, Figure 6.1, with structural phases that have numerous implications for how the structural instability is expressed. We have provided a novel, two-step CVT synthetic method which can be utilized in further crystal growth systems where balancing reactivity and crystal growth has proven difficult. Additionally, we have given innovative methods of structural solution that others can utilize for a multitude of substituents in the  $\text{VO}_2$  system as well as other systems where complex short-range ordering exists.

A two-step CVT synthesis has been utilized to obtain large single crystals of  $\text{V}_{1-x}\text{Mo}_x\text{O}_2$  that are sufficient for single property measurements and total X-ray scattering collection. The utilization of this two-step synthesis allowed us to avoid unwanted side reactions with the transport agent and by using an atmosphere of  $\text{MoCl}_2$  and  $\text{MoCl}_4$  in the first step of the synthesis of  $\text{V}_{1-x}\text{Mo}_x\text{O}_2$  can be obtained with higher molybdenum concentrations than what was possible through previous synthetic methods. Through further optimization of this synthesis, single crystals for the entire  $\text{VO}_2 - \text{MoO}_2$  compositional range might be possible. This type of two-step

synthesis could prove beneficial in other crystal systems where CVT synthesis has previously failed due to reaction between starting materials and otherwise optimal transport agents.

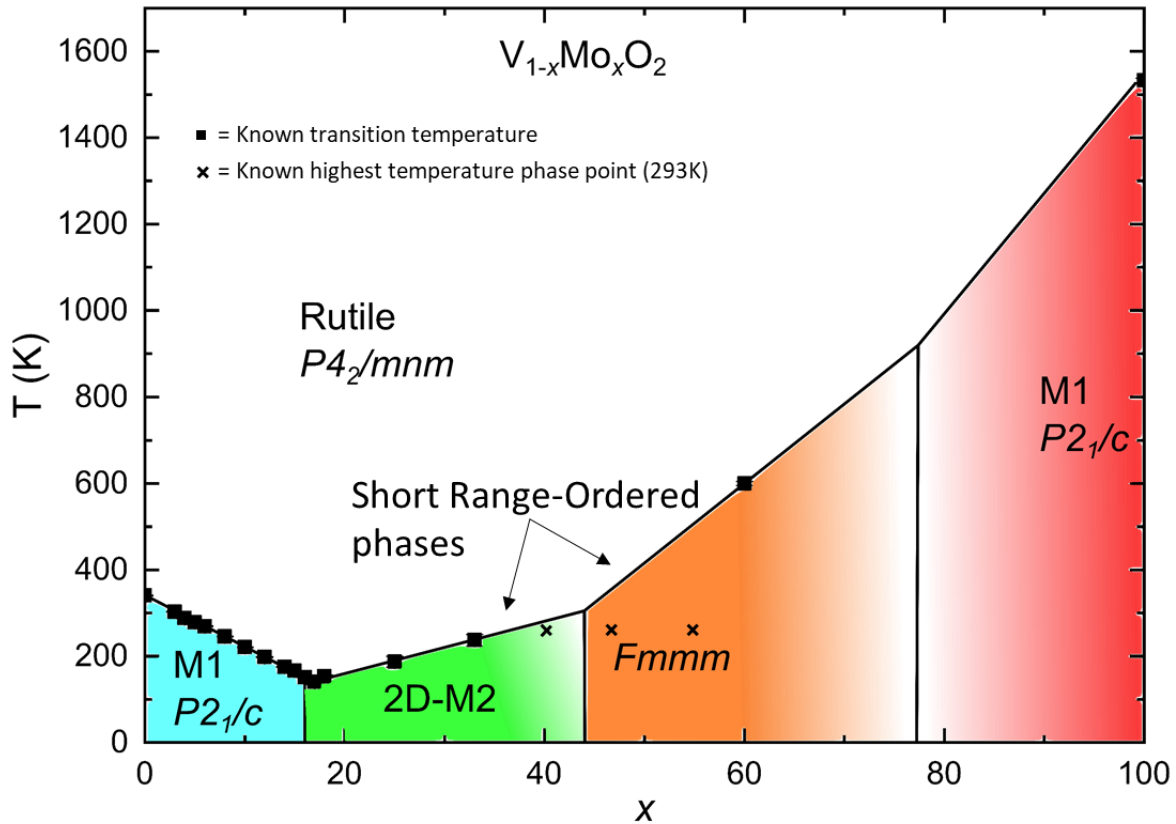


**Figure 6.1** Updated phase diagram including the newly characterized phase regions. The location and details about the phase boundary between the end of the *Fmmm* and the recurrence of the M1 phase at high molybdenum composition is still unknown.

Additionally, using a less complex one-step CVT synthesis, large single crystals of  $V_{1-x}Cr_xO_2$  and  $V_{1-x}W_xO_2$  can also be synthesized. A new metal-site ordered phase  $V_7Nb_6O_{29}$  has also been synthesized with a similar CVT procedure and the structure has been solved. The structure is non-centrosymmetric and appears to be a potential ferroelectricity candidate due to a ferroelectric distortion in the  $c$  direction. Further work needs to be done to obtain larger single crystals that can be used for physical property measurements.

Using crystals from the CVT synthesis, total scattering measurements on 15 compounds in the  $V_{1-x}Mo_xO_2$  and  $V_{1-x}Cr_xO_2$  families have been completed. Resulting in nearly 20 terabytes of useful data. From the total scattering data, we have uncovered a new type of ground state in  $V_{1-x}Mo_xO_2$ , 2D-M2, which occurs due to the 2D ordering of atomic displacements. We have shown that the structure is driven by geometric frustration. The real structure of this 2D ordered phase would have been impossible to describe using conventional crystallographic techniques, showing the power of the new 3D- $\Delta$ PDF method. We have also shown that the 2D-M2 phase weakens with increasing Mo content. A systematic study of the structural parameters in detail over a wide compositional range is still in process to reveal how the fundamental order parameters evolve, to help explain what conditions are required for the 2D-M2 state to manifest. This could result in a more complete physical model for  $VO_2$  and the underlying physics universal to all open shell rutile phases.

We have shown that conventional crystallography techniques can be used to solve the short-range order structure of  $V_{1-x}Mo_xO_2$  ( $0.50 \leq x \leq 0.60$ ) by using isotropic group-subgroup relations to direct the process. While we have shown that the long-range crystal structure is still rutile, there are strong local correlations that give rise to a phase with a distorted structure that best matches the orthorhombic  $Fmmm$  space group. This structural model is quite similar to the 2D-M2 phase at lower compositions and can be seen as the collapse of the 2D-M2 into one that has very short-range ordering equal in all 3 dimensions instead of just one and the culmination of the geometric frustration that is responsible for the 2D ordering. The solution of this structural phase helps to increase the understanding of the  $V_{1-x}Mo_xO_2$  phase diagram as well as the  $VO_2$  system in general since the same structural determination used for this phase can be applied to other related substituent phases that have structures which have proven difficult to understand.

Based on our findings, it is clear that the structural instability in VO<sub>2</sub> remains a rich topic of research even after decades of research on the VO<sub>2</sub> system. We have made major strides toward understanding the structural instability; however, further work on the local structures of V<sub>1-x</sub>Mo<sub>x</sub>O<sub>2</sub>, V<sub>1-x</sub>Cr<sub>x</sub>O<sub>2</sub>, and V<sub>1-x</sub>W<sub>x</sub>O<sub>2</sub> as well as other substituted VO<sub>2</sub> families of compounds needs to be completed in order to obtain a full picture of the structural instability in VO<sub>2</sub> and the effects of additional electrons, changes in oxidation state, and differences in atom size on the instability. As more information is obtained on this structural instability, it will continue to contribute to the discussion of the MIT in VO<sub>2</sub> and can be utilized in discussions on other related materials in the rutile system. Further work in exploring the isotropic group-subgroup relations will likewise prove invaluable to future structural solutions of difficult to determine structures.